The Dissertation Committee for Wei Wang Certifies that this is the approved version of the following dissertation:

Plasmonic Properties of Subwavelength Structures and Their Applications in Optical Devices

Committee:

Shaochen Chen, Supervisor

Li Shi, Co-Supervisor

Xiaojing Zhang

Paulo J. Ferreira

Gennady Shvets

Plasmonic Properties of Subwavelength Structures and Their Applications in Optical Devices

by

Wei Wang, B.E.; M.S.E.

Dissertation

Presented to the Faculty of the Graduate School of

The University of Texas at Austin

in Partial Fulfillment

of the Requirements

for the Degree of

Doctor of Philosophy

The University of Texas at Austin

December, 2010

Dedication

To my parents

Acknowledgements

First of all, I would like to sincerely thank my supervisor, Professor Shaochen Chen, for bringing me into his research group and teaching me with his knowledge and wisdom. Under his patient guidance and help, my graduate studies here in his group had become a wonderful journey and the most rewarding experience in my life.

I would also like to thank my committee members, Prof. Li Shi, Prof. Xiaojing Zhang, Prof. Paulo J. Ferreira, and Prof. Gennady Shvets for serving on my dissertation committee and providing advices on my dissertation.

I am also grateful to all my lab mates, past and present, for their help and friendship. I would like to give special gratitude to Dr. Arvind Battula, Dr. Dongbing Shao, Dr. Yi Lu, Dr. David Fozdar, Dr. Li-Hsin Han, Shaomin Wu, Daniel Eils and Wande Zhang, for their assistance in my work. In particular, I would like to Dr. Arvind Battula for helping me learn using simulation software and physics. In addition, I would like to thank all the faculty and staff in the Materials Science and Engineering program.

Moreover, I would like to thank my family for their consistent love and support. I wouldn't have gone this far if it weren't for my family. I would like to thank my parents Shulin Wang and Yanmin Li for their unending encouragement. At last, I am very thankful to my best friend Si, and Feng, Yibo for their support.

Wei Wang

University of Texas at Austin

Austin, TX

Plasmonic Properties of Subwavelength Structures and Their Applications in Optical Devices

Publication No._____

Wei Wang, Ph.D.

The University of Texas at Austin, 2010

Supervisor: Shaochen Chen, Li Shi

A metallic hole array of a rectangular converging-diverging channel (RCDC) shape exhibits extraordinary transmission for wavelengths larger than the periodicity of the holes. We use a three-dimensional (3D) finite element method to analyze the transmission characteristics of two-dimensional metallic hole arrays (2D-MHA) with RCDC. For a straight channel MHA, when the aperture size is reduced, the transmission peaks have a blue-shift. The same result is observed for a smaller gap throat for the RCDC structure. For the rectangular holes with a high length-width ratio, a similar blue-shift in the transmission peaks as well as a narrower full width at half maximum (FWHM) are observed. The asymmetry from the rectangular shape gives this structure high selectivity for light with different polarizations. Furthermore, the RCDC shape gives extra degrees of geometrical variables to 2D-MHA for tuning the location of the transmission peak and the FWHM.

Tunable extraordinary transmission via changing temperature of a porous metallic layer on top of a thin layer of dielectric strontium titanate (STO) is then studied. The

metallic layer has a through-hole array and each hole has a circular converging-diverging channel (CDC) shape, which induces the excitation of surface plasmon polaritons (SPPs) and then results in a controllable extraordinary optical transmission in the terahertz (THz) frequency range. We use a three-dimensional (3D) finite element method to analyze the transmission characteristics of the structure. Location and magnitude of the transmission peaks can be adjusted by the hole size, converging angle, and thicknesses of metal and STO layers. Remarkably, the suggested structure presents a strong transmission dependency on temperature, which offers a new approach to actively and externally tune the transmission.

Currently, the performances of thin film solar cells are limited by poor light absorption and carrier collection. In this research, large, broadband, and polarization-insensitive light absorption enhancement is realized via integrating with unique metallic nanogratings. Through simulation, three possible mechanisms are identified to be responsible for such an enormous enhancement. A test for totaling the absorption over the solar spectrum shows an up to ~30% broadband absorption enhancement when comparing to bare thin film cells.

Overall performance of a thin film solar cell is determined by the efficiency of conversing photons to electrons that include light absorption, carrier generation and carrier collection processes. Photon management via hybrid designing has been emerging as a powerful means to further boost the conversion efficiency. Here a new nanograting solar cell design, which can be universal and a new solar cell platform technology, is proposed with goals to achieve large enhancement on broadband light absorption and carrier generation, most importantly, under the much reduced usage of active and non-earth-abundant materials. A test for the short circuit current density in $CuIn_xGa_{(1-x)}Se_2$ (CIGS) thin film solar cells shows an up to ~250% enhancement when comparing to the

corresponding bare thin film cells. Besides that, by placing metal strips on top of the nanograting, which act as the top electrode, this design is able to reduce the use of non-earth-abundant materials such as indium that is normally used in both active and transparent conducting materials.

Table of Contents

List of Figures

Chapter 1: Plasmonic Properties of Subwavelength Structures

1.1 Introduction

The electromagnetic properties of metal/dielectric interfaces have attracted a vast amount of research effort ever since the work of Mie [1] and Ritchie [2] for small particles and flat interfaces, respectively. Since then, the ability of such structures to sustain coherent electron oscillations known as surface plasmon has been intensively investigated. There are two main ingredients of plasmonics—localized surface plasmons and surface plasmon polaritons (SPPs). The localized surface plasmons are non-propagating excitations of conduction electrons of metallic nanostructures caused by the oscillating—electromagnetic field, which arise naturally from the scattering of sub-wavelength conductive nanoparticles in an electromagnetic wave. On the other hand, surface plasmon polaritons are propagating electromagnetic excitations at the interface between a dielectric and a conductor, evanescently confined in the perpendicular direction. These electromagnetic surface waves arise via the coupling of the electromagnetic fields to oscillations of the conductor's electron plasma. [3] These interaction processes between electromagnetic radiation and conduction electrons at small metallic nanostructures with metal/dielectric interface lead to an enhanced optical near field of subwavelength dimension. As a result, plasmonics is now a major part of the field of nanophotonics and a powerful tool to study and control the optical/electromagnetic phenomena that have characteristic dimensions smaller than the radiation wavelength or associated with subwavelength scale structures.

The field of plasmonics is a hundred years old, after initial studies of this interaction between electrons and photons, there is a lot of work proposed both in the area of the fundamental physics [4] and for applications such as surface-enhanced

spectroscopy and enhancement of nonlinear light generation. More recently, there has been a resurgence of interest in this field, mainly due to the following three reasons. The first is the development of fabrication techniques such as electron-beam lithography (EBL), ion-beam milling, and self-assembly [6], which made the implementation of nanostructures possible. Second, the rapid advance in computing power and speed has provided us a faster and cheaper way to conduct the plasmonics research using powerful numerical modeling tools. The third, and the most important one, is that the ability to control electromagnetic field in the nanoscale provides wide range of potential applications— solar cells, high-resolution microscopy, drug design and many more.

In most cases, we can derive the plasmonics properties directly using Maxwell's Equations. Indeed, Maxwell's Equations are the most powerful tools for nowadays' plasmon research. In this chapter, from the basic wave equations, which are direct derivations of Maxwell's Equation, we will first discuss the fundamentals of both localized surface plasmons and SPPs on classical model. Then we will introduce the excitation techniques, and applications.

1.2 Localized Surface Plasmons

Long before Gustav Mie [1] published his famous paper "Beiträge zur Optik trüber Medien, speziell kolloidaler Metallösungen" (contributions to the optics of turbid media, particularly solution of colloidal metals)—in which, Mie derived the optical-absorption spectrum by directly solving Maxwell's equations for the scattering of electromagnetic waves by spherical objects—the property of strong interaction between microscopic metal particles and visible light has been employed for many purposes. Historically, one prominent use of metal nanoparticles was the staining of glass windows and ceramic pottery [5]. Small Au nanoparticles embedded in the glass show a strong

optical absorption of light in the green part of the visible spectrum, which results in that the glass shows a red color when seen in transmitted light and shows a green color when seen in reflected light.

The absorption spectrum of Au is shown in Fig. 1.1. [6] Au particles show striking differences compared to their bulk and thin film responses. The absorption spectrum of 30-nm Au nanoparticles in water (red dots) was obtained by directly solving Maxwell's equations for the scattering of electromagnetic waves by spherical objects as carried out by Mie and retaining only the dipolar term [1], which is suitable for nanoparticles with a diameter $d<<\lambda$, where λ is the wavelength of light in the surrounding medium. Compare this curve with the measured absorption spectrum of an aqueous solution of 30-nm Au colloids (black dots), the quasistatic approximation is in good agreement with measurement data, which has been confirmed via a plethora of studies of the optical response of metallic nanoparticles with a diameter well below λ in solid, liquid, and gaseous environments.

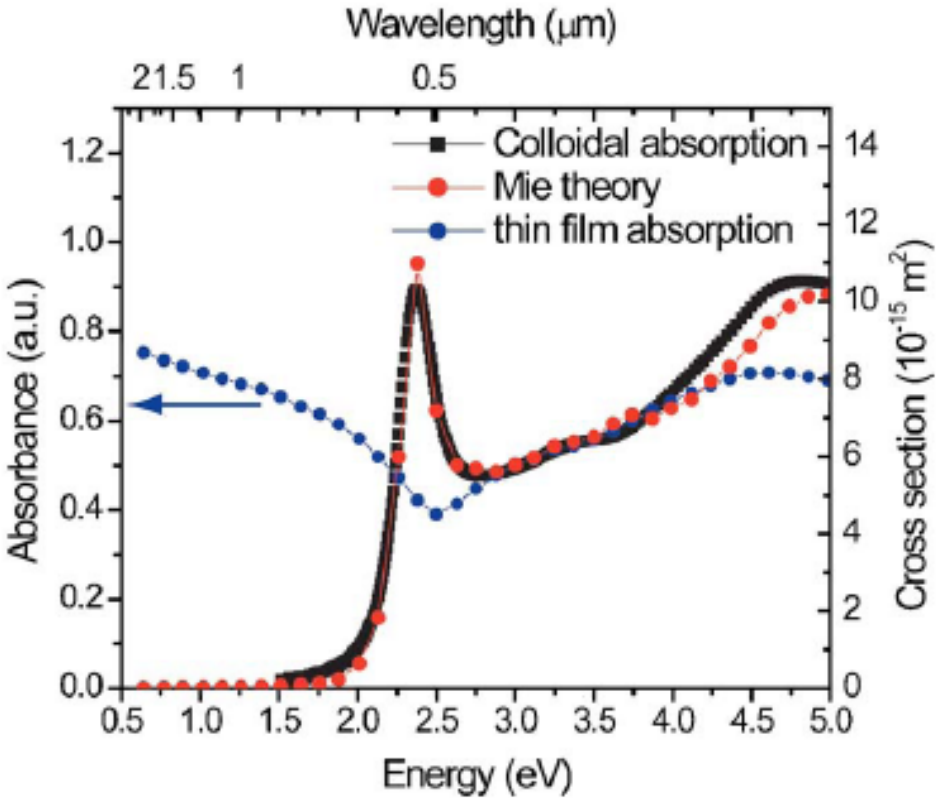

Figure 1.1: Calculated absorption spectrum of a thin gold film (blue dots) and of 30-nm Au nanoparticles in water (red dots) using classical electromagnetic theory. A measured absorption spectrum of an aqueous solution of 30-nm Au colloids (black dots) shows good agreement with the theory. [6]

The unique electromagnetic property of noble-metal nanoparticles is due to the small particle volume. While particles with a diameter $d<<\lambda$ in the environment with radiation of wavelength λ, the conduction electrons inside the particles all move in phase upon plane-wave excitation which leads to the buildup of polarization charges on the particle surface. The charges then act as a restore force which induces a resonance at certain frequency, which is called the particle dipole plasmon frequency. At this specific frequency, the electrons oscillate at a $\pi/2$ phase lag with respect to the driving field, forming a resonant field inside the particle, which in the small particle limit is

homogeneous throughout its volume. This resonant field produces a dipolar field outside the particle which leads to enhanced absorption and scattering cross sections for electromagnetic waves, as well as to a strongly enhanced near field in the immediate vicinity of the particle surface. Indeed, all the special property and applications are based on this dipolar field. [1] In the following part of this section, we will explore the physics of localized surface plasmons by considering the interaction of an electromagnetic wave with a spherical metal nanoparticle placed in a homogeneous medium.

Consider a spherical particle with diameter D and isotropic dielectric constant $\varepsilon(\omega)$ that is placed in an arbitrary medium (with dielectric constant ε_m) in which there exists a uniform static electric field $\vec{E}_0 = E_0 e^{-i\omega t}\hat{z}$ travelling along the z direction with wavelength $\lambda >> D$. Let the electric fields inside and outside the sphere to be $\vec{E}_1$ and $\vec{E}2$, respectively, which are derivable from scalar potential $\Phi(r,\theta)$

$$\vec{E}_1 = -\nabla\Phi, \qquad (r < D/2)$$
$$\vec{E}_2 = -\nabla\Phi, \qquad (r > D/2)$$

Where

$$\nabla^2\Phi = 0. \tag{1.1}$$

Due to the symmetry of the problem, Φ is independent of the azimuthal angle φ, so the general solution is of the form [7]

$$\Phi(r,\theta) = \sum_{l=0}^{\infty}[A_l r^l + B_l r^{-(l+1)}]P_l(\cos\theta) \tag{1.2}$$

where $P_l(\cos\theta)$ is the l order Legendre Polynomials, θ is the angle of the position vector r and the z-axis, A and B are the constants to be determined by the boundary conditions.

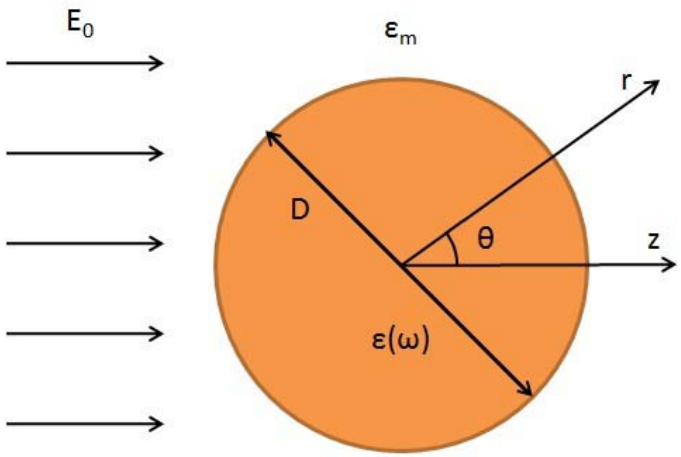

Figure 1.2: Sketch of an isotropic spherical particle in an electromagnetic field.

Let the potential inside and outside the particle be Φ_1 and Φ_2, respectively. Since the potential Φ cannot be infinite at r = 0,

$$\Phi_1(r,\theta) = \sum_{l=0}^{\infty} A_l r^l P_l(\cos\theta) \tag{1.3a}$$

$$\Phi_2(r,\theta) = \sum_{l=0}^{\infty} [B_l r^l + C_l r^{-(l+1)}] P_l(\cos\theta) \tag{1.3b}$$

as $r \to \infty$, $\Phi \to -E_0 z = -E_0 r\cos\theta$. This requires $B_l = -E_0$ for $l = 1$ and $B_l = 0$ for $l \neq 1$. At the boundary of the particle $r = D/2$, the tangential electric field and normal displacement filed are continuous.

$$-\frac{2}{D}\frac{\partial \Phi_1}{\partial \theta}\Big|_{r=D/2} = -\frac{2}{D}\frac{\partial \Phi_2}{\partial \theta}\Big|_{r=D/2} \tag{1.4}$$

$$-\varepsilon_0 \varepsilon \frac{\partial \Phi_1}{\partial r}\Big|_{r=D/2} = -\varepsilon_0 \varepsilon_m \frac{\partial \Phi_2}{\partial r}\Big|_{r=D/2} \tag{1.5}$$

Plug 1.4 and 1.5 into equation 1.3, the coefficients A, B and C can be determined and the final form of the potential function are:

$$\Phi_1(r,\theta) = -\frac{3\varepsilon_m}{\varepsilon + 2\varepsilon_m} E_0 r\cos\theta \tag{1.6}$$

$$\Phi_2(r,\theta) = -E_0 r\cos\theta + \frac{\varepsilon - \varepsilon_m}{\varepsilon + 2\varepsilon_m} E_0 D^3 \frac{\cos\theta}{8r^2} \tag{1.7}$$

Now consider a dipole centered at *r=0* and with moment $\vec{p}$ parallel to the z direction, where *p=qd.* If we let *d* approach zero in such a way that the product *qd* remains constant, we obtain the potential of an ideal dipole

$$\Phi = \frac{\vec{p}\cdot\vec{r}}{4\pi\varepsilon_m r^3} = \frac{p\cos\theta}{4\pi\varepsilon_m r^2} \tag{1.8}$$

Compared with equation 1.7, the field outside the sphere is the superposition of the applied field and the field of an ideal dipole at the origin with dipole moment

$$\vec{p} = \frac{1}{2}\pi\varepsilon_0 D^3 \frac{\varepsilon - \varepsilon_m}{\varepsilon + 2\varepsilon_m}\vec{E_0} \tag{1.9}$$

$$\Phi_2(r,\theta) = -E_0 r\cos\theta + \frac{\vec{p}\cdot\vec{r}}{4\pi\varepsilon_0 r^3} \tag{1.10}$$

The metallic sphere in the applied electromagnetic wave acts as a dipole with moment proportional to the field. The polarized sphere can be specified by the polarizability α defined by

$$\vec{p} = \varepsilon_0 \alpha \vec{E_0}$$

$$\alpha = \frac{1}{2}\pi D^3 \frac{\varepsilon - \varepsilon_m}{\varepsilon + 2\varepsilon_m} \tag{1.11}$$

The distribution of the electric field $\vec{E} = -\nabla\Phi$ can be calculated from equation 1.6 and 1.7

$$\vec{E}_1 = \frac{3\varepsilon_m}{\varepsilon + 2\varepsilon_m}\vec{E}_0 \tag{1.12a}$$

$$\vec{E}_2 = \vec{E}_0 + \frac{3\vec{n}(\vec{n}\cdot\vec{p}) - \vec{p}}{4\pi\varepsilon_0\varepsilon_m}\frac{1}{r^3} \tag{1.12b}$$

By calculating the Poynting vector $\vec{S} = \vec{E} \times \vec{H}$, the scattering and absorption cross sections of a spherical subwavelength particle can be obtained [8].

$$C_{abs} = \frac{2\pi}{\lambda}\mathrm{Im}[\alpha] \tag{1.13a}$$

$$C_{sca} = \frac{1}{6\pi}\left(\frac{2\pi}{\lambda}\right)^4 |\alpha|^2 \tag{1.13b}$$

A compare with equation 1.11, 1.12 and 1.13 shows that when the dielectric constant of the metallic nanoparticle meets

$$Re|\ \varepsilon(\omega)\ | = -2\varepsilon_m \tag{1.14}$$

the value of polarizability $|\alpha|$ reaches a resonant maximum. At the same time, the internal and dipolar fields, and the scattering cross sections are also maximized. Equation 1.14 is called the Fröhlich condition and the associated mode the *dipole surface plasmon* of the metal nanoparticle.

1.3 SURFACE PLASMON POLARITONS

To study this interface and the interesting electromagnetic phenomenon we need first to clarify some relatively simple but important concepts of electromagnetism.

The first concept comes to the *s* and *p-polarized* light. According to the Maxwell's Equations, for a field without free charges, electromagnetic radiation in isotropic media consists of orthogonal oscillating electric and magnetic fields transverse

to the propagation direction. Then when the radiation passes through a linear polarizer, it will be plane polarized. That means there is a well specified plane in which E or B oscillates, this plane containing the appropriate electromagnetic held vector and the direction of propagation. Now if we consider such radiation falling at an incident angle θ upon a smooth planar interface then we have to consider two important situations.

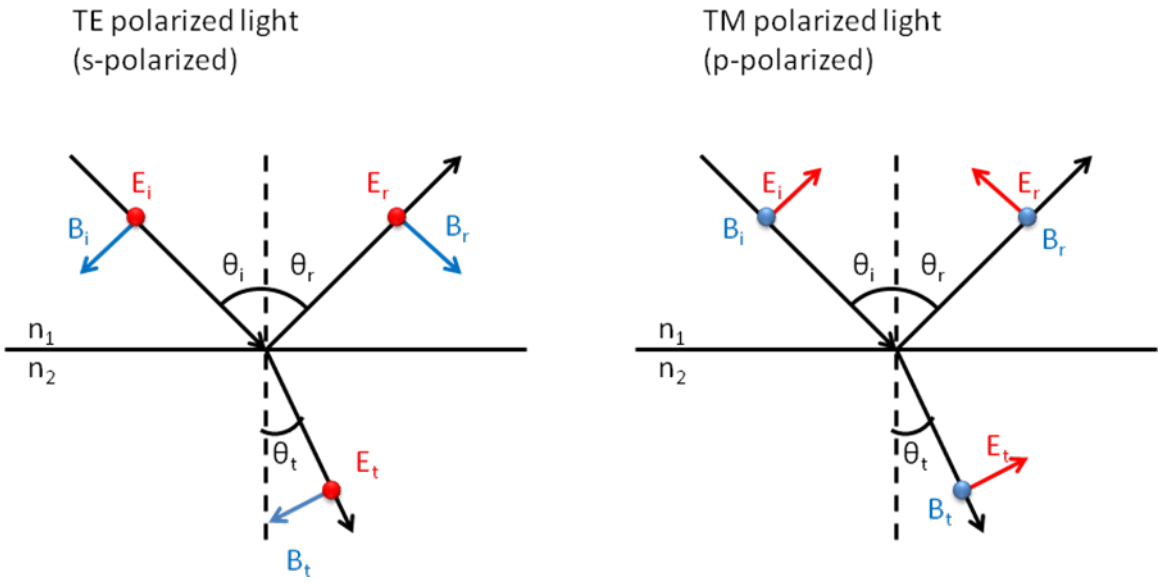

Figure 1.3: *s* and *p-polarized* light

As shown in Figure 1.3, in the first case E vector only has component tangential to the interface, and B vector has both normal and tangential components. In the second case, B vector only has tangential component to the interface, and E vector has both components. Any linearly polarized radiation may be readily represented by a sum of the above two cases.

Now consider a light with free space wavevector k. When in a medium of refractive index n_1, the wavevector changes to $k_1=kn_1$. If the light incidents at a planar interface with an angle θ_i and refract in the new medium at an angle θ_r, the tangential

component of the wavevector will conserve, yet the normal component will be different in media with different refractive index. Considering the reflected light in the same medium, the magnitude and tangential component of the wavevector $|k_1|$ and k_{x1} is conserved, then it follows that k_{z1} of the reflected light is $-k_{z1}$, the usual law of reflection al a planar interface.

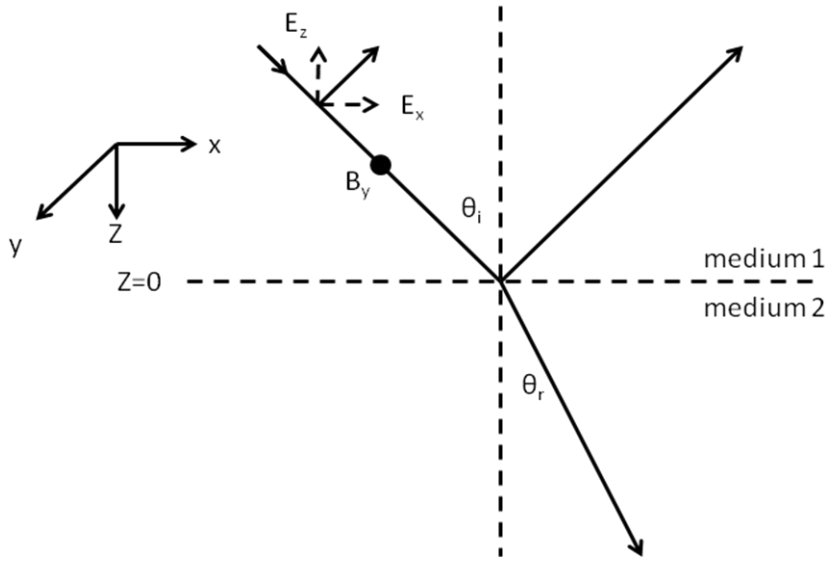

Figure 1.4: *P-polarized* radiation incidents a surface [9]

On the other hand, in the second medium with refractive index n_2, the new wavevector is $k_2=kn_2$ with tangential component $k_{x2}=k_2 sin\theta_r$. Since the tangential component is the same in medium 1, then $k_2 sin\theta_r = k_1 sin\theta_i$, which will give the Snell's Law, $n_1 sin\theta_i = n_2 sin\theta_r$. Supposing the light travels from a high index medium to a low medium ($n_2<n_1$), since the maximum of $sin\theta_r$ is 1, there is a limiting angle of incidence, θ_c, given by

$$sin\ \theta_c = n_2/n_1 \tag{1.15}$$

This angle is called *critical angel*, beyond which the incident radiation has more momentum along the surface plane than can be supported by medium 2. At this time, all

light will be reflected and there is no refractive light. However, for such radiation the oscillating E field will cause the charges in medium 1 and at the interface to oscillate. And this oscillation will induce a radiation penetrating into medium 2. These fields cannot propagate, but are spatially decaying fields (evanescent) which oscillate in time, at the same frequency as the incident radiation, decaying in amplitude in medium 2 in a direction normal to the interface. At the critical angle the decay length is infinite but this falls rapidly to the order of the wavelength of light as the angle of incidence is further increased. This evanescent field for radiation incident beyond the critical angle is useful for coupling radiation to surface plasmons as we shall see later.

Next we consider the boundary conditions of E and B fields. Since there is no boundary orthogonal to E_x, this component is conserved across the boundary. And since there is no free charge at the interface, D_z is continuous. Together with equation $D_z=\varepsilon E_z$, we can get the boundary condition of E_z,

$$\varepsilon_1\varepsilon_0 E_{z1}= \varepsilon_2\varepsilon_0 E_{z2} \tag{1.16}$$

This discontinuity in E_z results in polarization changes at the interface. Since it does not contain normal component, *s-polarized* incident radiation will not normally cause the creation of charge at a planar interface, while p-polarized radiation will automatically create time dependent polarization charge at the interface.

Based on the discussion above, only *p-polarized* electromagnetic contributes to the creating of charges at the interface. As a result, we only need to consider this model. If we take the x-y plane to be the interlace plane and the positive z half space as medium 2 as shown in Figure 1.4, the E, B field can be written in the form of wave equation [9]

$$E_1 = (E_{x1}, 0, E_{z1}) \exp(ik_x x) \exp(ik_{z1} z) \exp(-i\omega t) \quad (1.17a)$$

$$H_1 = (0, H_{y1}, 0) \exp(ik_x x) \exp(ik_{z1} z) \exp(-i\omega t) \quad (1.17b)$$

$$E_2 = (E_{x2}, 0, E_{z2}) \exp(ik_x x) \exp(ik_{z2} z) \exp(-i\omega t) \quad (1.17c)$$

$$H_2 = (0, H_{y2}, 0) \exp(ik_x x) \exp(ik_{z2} z) \exp(-i\omega t) \quad (1.17d)$$

Applying Maxwell's Equations $\nabla \cdot E = 0$ and $\nabla \times E = -\mu \frac{\partial H}{\partial t}$ in the wave equations 1.17, we can get

$$E_{z1} = -E_{x1} = \frac{k_x}{k_{z1}} \quad (1.18a)$$

$$E_{z2} = -E_{x2} = \frac{k_x}{k_{z2}} \quad (1.18b)$$

$$H_{y1} = \omega E_{x1} \varepsilon_1 \varepsilon_0 / k_{z1} \quad (1.18a)$$

$$H_{y2} = \omega E_{x2} \varepsilon_2 \varepsilon_0 / k_{z2} \quad (1.18b)$$

Then we apply the boundary conditions at z=0. According to the electromagnetic theory, the tangential H is continuous and so is the tangential E, which leads to the simple equation between the permittivities and the normal component of wavevector below

$$\frac{\varepsilon_1}{k_{z1}} = \frac{\varepsilon_2}{k_{z2}} \quad (1.19)$$

Also since $\varepsilon_i k^2 = k_x^2 + k_{zi}^2$, $i=1,2$. If the wave is truly a trapped surface wave with exponential decays into both media then we need $ik_{z1} > 0$ and $ik_{z2} < 0$. Thus both k components are imaginary with opposite signs

$$k_{z1} = -i(k_x^2 - \varepsilon_1 k^2)^{1/2}, \text{ requiring } k_x^2 > \varepsilon_1 k^2$$

$$k_{z2} = i(k_x^2 - \varepsilon_2 k^2)^{1/2}, \text{ requiring } k_x^2 > \varepsilon_2 k^2 \quad (1.20)$$

Equation 1.20 tells us that, to have decaying waves in both sides of the interface, two requirements must to be met. First, the relative permittivities in two media must be in opposite signs. This requirement is automatically satisfied for the case of an interface between dielectric and metal materials. Second, the surface mode wavevector k_x must be

greater than the maximum photon wavevector available in the dielectric. Substituting expressions (1.20) into (1.19) will give:

$$k_x = k\left(\frac{\varepsilon_1\varepsilon_2}{\varepsilon_1+\varepsilon_2}\right)^{1/2} \tag{1.21}$$

Where ε_2 (relative permittivity in metal) is a complex number with a real component $\varepsilon_{2r}<0$ and an imaginary part ε_{2i}.

So the wavevector is also a complex number:

$$k_x = k\left[\frac{\varepsilon_1(\varepsilon_{2r}+i\varepsilon_{2i})}{\varepsilon_1+\varepsilon_{2r}+i\varepsilon_{2i}}\right]^{1/2} \tag{1.22}$$

with a real component $k_{xr} \cong k\varepsilon_1^{1/2}\left(1-\frac{\varepsilon_1}{2\varepsilon_{2r}}\right)$ and an imaginary component $k_{xi} = \frac{1}{2}k\frac{\varepsilon_{2i}\varepsilon_1^{3/2}}{\varepsilon_{2r}^{2}}$ [9]. The imaginary component of the wavevector is related with the propagation length of the surface plasmon.

Form equation (1.22), we can see that for k_x to be real, the requirement is $|\varepsilon_{2r}| > \varepsilon_1$. This equation also tells us that the interaction between the surface charge density and the electromagnetic field results in the momentum of the SPPs mode, k_x, being greater than the free-space wavevector k. So it is a big issue to provide this extra momentum to take advantage of SPPs. The techniques providing the missing momentum will be discussed below.

1.3.3 Excitation of surface plasmon polaritons at planar interfaces

As discussed in section 1.2, localized surface plasmons arise naturally from the scattering of a small, sub-wavelength conductive nanoparticle in an electromagnetic wave. The curved surface of the particle exerts an effective restoring force on the driven electrons, so that a resonance can be excited by direct light illumination.

For the case of SPPs, however, the surface mode wavevector is greater than the maximum photon wavevector available in the dielectric, which results in the SPPs propagating at the flat interface are essentially two-dimensional electromagnetic waves decaying on both sides of the interface. Therefore, SPPs excitation by three-dimensional light beams is not possible unless special excitation techniques are employed.

There have been already lots of excitation techniques available for different application requirements. In this section, we will concentrate on two techniques used to take advantage of surface plasmon at the dielectric/metal interface. The main idea of the first one is to make use of prism coupling to enhance the momentum of the incident light at the smooth interface. [10] The second one involves utilizing the gratings to excite the surface plasmons. [11]

1.3.3.1 Prism coupling

The use of prism is to produce enhanced momentum of photons in the dielectric medium. To better explain the method, we have to refer to the concept of critical angle introduced before. Beyond the critical angle of incidence there will be an evanescent field in the second half space. This evanescent field does not propagate, but has a momentum in the x direction, which is $n_1\hbar k\sin\theta_i$, since $\theta_i > \theta_c$, $n_1\hbar k\sin\theta_i > n_2\hbar k$. Therefore, the enhancement of momentum in the dielectric medium is $n_1\hbar k\sin\theta_i - n_2\hbar k = n_1\hbar k(\sin\theta_i - \sin\theta_c)$, which could be used to couple radiation to SPPs. As a result it is possible to place the metal/dielectric interface which supports the surface plasmon close enough to the totally internally reflecting interface. An obvious geometry to consider is that shown in Figure 1.5, which is called Otto geometry. [9-10]

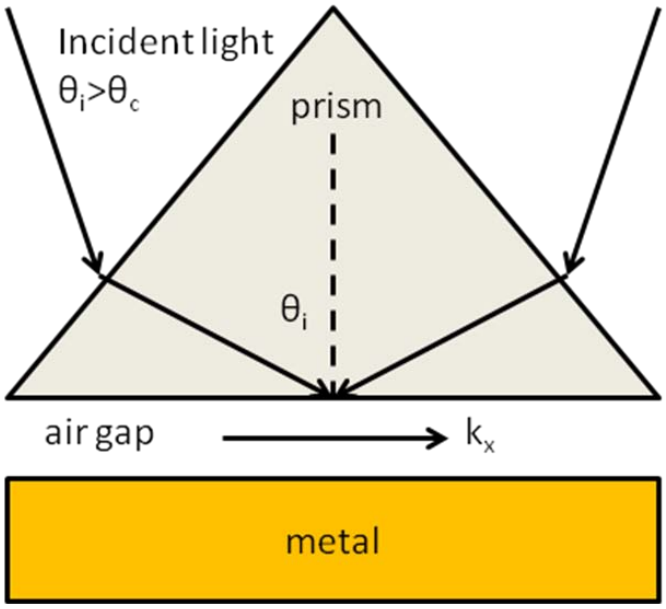

Figure 1.5: Otto geometry

The figure shown that, by varying the incident angle from the prism, we can get an x-component of electric field larger than it can be sustained in the air gap (or a space with low index). Then there will be an evanescent electric field in the gap as we mentioned before. This field will excite the surface plasmon at the air (dielectric) metal interface. The air gap is less than a few radiation wavelengths thick (for visible < 2μm). The reflectivity curve for gold and silver at 632.8 nm is shown in Figure 1.6 [9]. This figure also shown the *s-polarized* radiation is not capable of creating the surface plasmon.

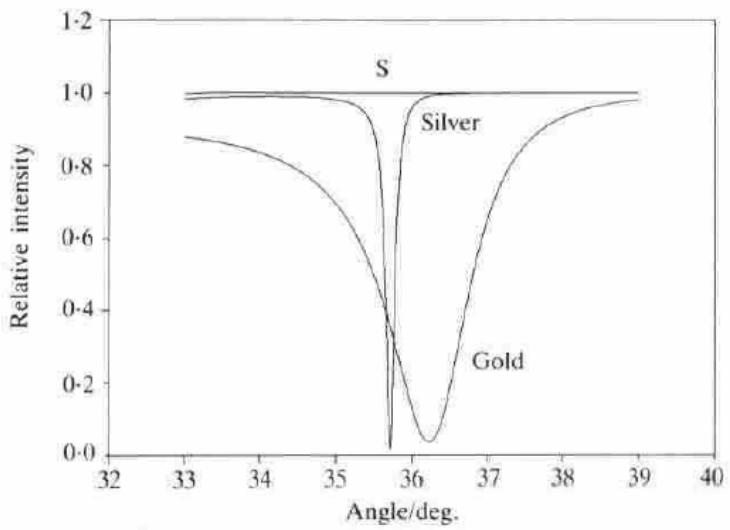

Figure 1.6: Form of the reflectivity curve for *p-polarized* and *s-polarized* radiation (λ=632.8μm) from thick gold and silver films with a sapphire prism (n = 1.766). Here the coupling gap is 0.5μm for gold and 1.0μm for silver. [9]

A very obvious disadvantage of Otto geometry is that it is difficult to fabricate the air gap. This problem may be addressed in quite a different manner by using, instead of an air gap, an evaporated dielectric spacing layer (or perhaps a spun polymer). There also have been many substitutions to the Otto geometry, which are shown in figure 1.7 [9]

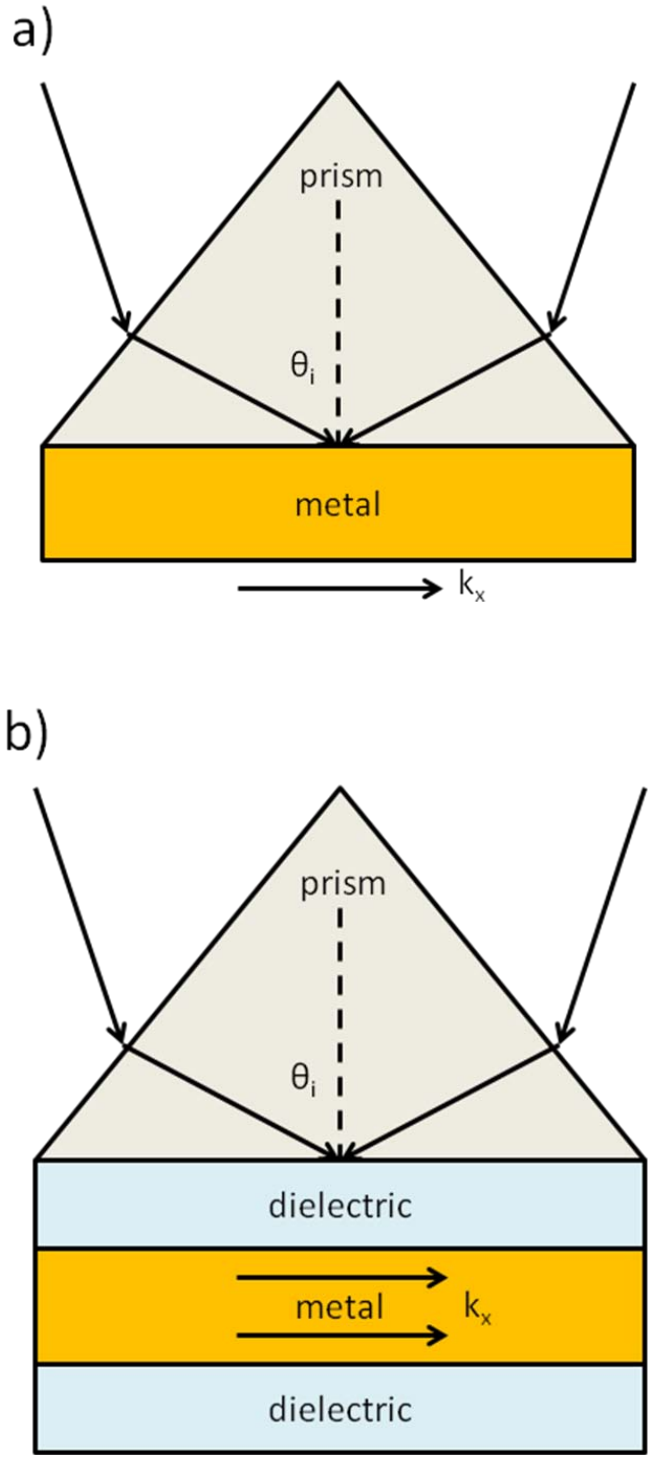

Figure 1.7: Substitutions to Otto geometry. a) Kretschmann-Raether, b) mixed hybrid arrangement

1.3.3.2 Grating coupling

The mismatch in wave vector between the surface wave and impinging photons can also be achieved by patterning the metal surface with a shallow grating of grooves or holes with lattice constant (periodicity) *p*. As shown in Fig. 1.8, for the simple one-dimensional grating of grooves, phase matching takes place:

$$k_{sp} = k_{\parallel} \pm 2n\pi / a \tag{1.23}$$

where k_{sp} is the wavevector of the surface plasmon $k_{sp} = k_0 = \frac{1}{\sqrt{1+(1/\varepsilon_m)}}$, k_x is the in-plane wavevector $k_x = k\sin\theta$, a is the lattice constant (periodicity), and *n = (1, 2, 3…).* As with prism coupling, excitation of SPPs is detected when the reflected light is at minimum. Surface plasmon excited by grating dielectric/metal interface attracted intensive interest recently since Ebbesen et al. first reported in a now famous paper that a thin metal film perforated with an array of subwavelength sized holes can transmit much more light than expected [12]. This unique phenomenon is call extraordinary optical transmission, which will be described in the next section.

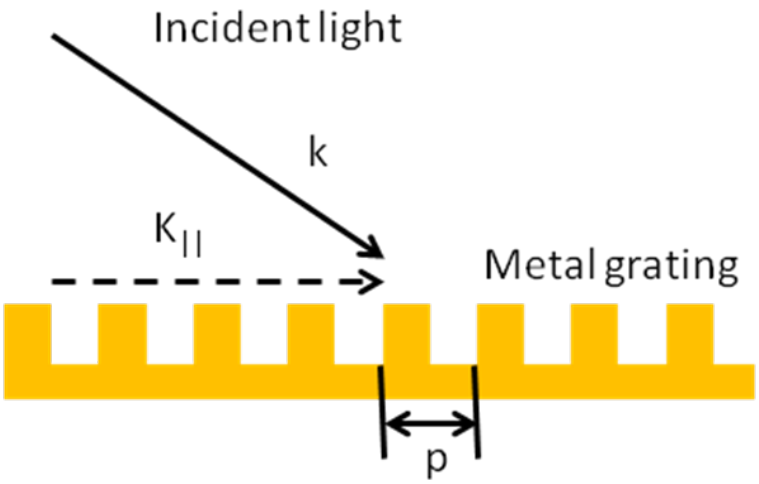

Figure 1.8: Phase-matching of light to SPPs using a grating.[11]

1.4 APPLICATIONS OF PLASMONICS

Surface plasmons, as we mentioned above, is a phenomenon we can use to manipulate the flow of light at nanoscale. With different elaborately designed structure, one can use surface plasmons to manipulate light for different purposes. Research in this area could lead to an entirely new class of optical devices. Ultimately it may be possible to employ plasmonic components in a wide variety of instruments, with their help we will be able to improve the resolution of microscopes, the efficiency of light-emitting diodes (LEDs) and the sensitivity of chemical and biological detectors. Scientists are also considering medical applications, designing tiny particles that could use plasmon resonance absorption to kill cancerous tissues, for example. And some researchers have even theorized that certain plasmonic materials could alter the direction of light around an object to such an extent that it would become invisible—the technology that may make invisibility cloaks a reality.

Plasmonics, along with the developments of computational power—which have enabled investigators to accurately simulate the complex electromagnetic fields generated by plasmonic effects, and novel methods for fabricating nanoscale structures—which have made it possible to build and test ultrasmall plasmonic devices and circuits improve our understanding of light and extend our ability to utilize light in a broader range. In the following part of this section, we will introduce some important and interesting applications.

A major phenomenon observed for the plasmonic nanostructures is the extraordinary optical transmission through metal subwavelength hole arrays. When light scatters through apertures, it diffracts at the edges. In the subwavelength regime, Bethe gave a theoretical description of the diffraction of light at a given wavelength λ through a circular hole of radius $r<<\lambda$ in the idealized situation of an infinitely thin and perfect

metal sheet. He has shown that the transmission $T(\lambda)$ scales uniformly with the ratio of r to λ to the power of four, as described in equation (1.24)

$$\eta_B = 64(kr)^4/27\pi^2 \qquad (1.24)$$

When the scale of the hole is smaller than the wavelength of the incident light, the amount of transmission light will be very limited. However, recently, several experiments have shown that, if holes are structured forming a 2D periodic array in a metallic film, extraordinary optical transmission can be obtained at wavelengths up to 10 times larger than the diameter of the holes [12]. Figure 1.9 shown the geometry [12] used to achieve the high transmission.

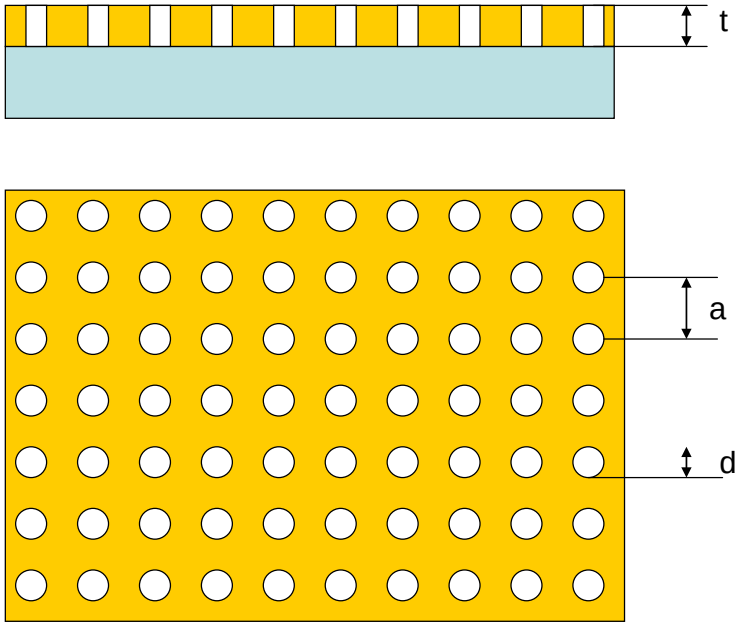

Figure 1.9: Schematic view of the subwavelength hole array

Figure 1.10 shows the zero-order transmission spectrum through the 2D subwavelength hole array [12]. The transmission peaks become gradually stronger at longer wavelengths, even beyond the minimum at the periodicity a_0. This result is very different from Bethe's prediction. There have been arguments about the main cause of

this high transmission through subwavelength holes [13-15]; however, more and more researchers in this area are beginning to believe that enhanced transmission through subwavelength MHA can be divided into three steps: the coupling of light to SPPs on the incident surface, the transmission through the holes and the re-emission from the second surface.

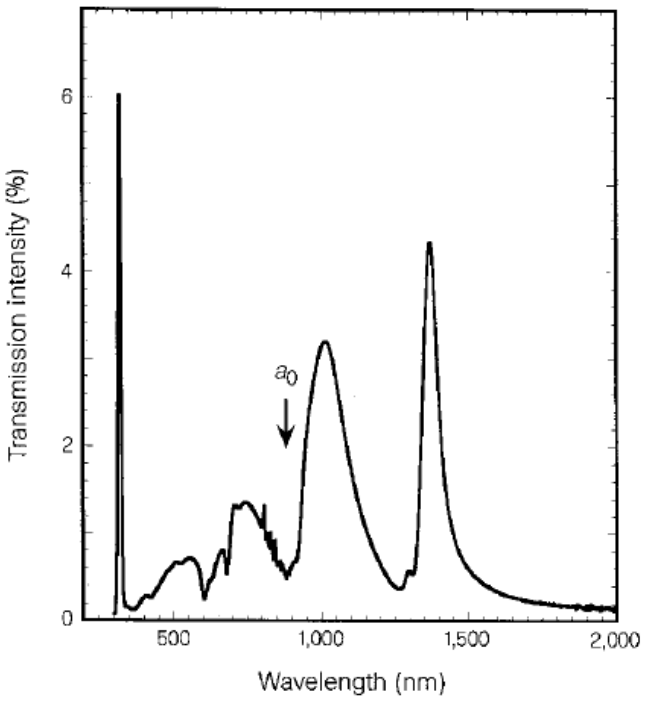

Figure 1.10: Zero-order transmission spectrum of an Ag array (a_0*= 0.9μm, d = 150 nm, t = 200 nm*)

The most straightforward applications are frequency selective optical filters. By varying the shape of the holes or applying external fields, tunable transmission can be achieved [16-24]. Porto et al. demonstrated optical bistability by filling non-linear

materials into sub-wavelength apertures, which can be regarded as optical switch [25]. Wenger et al. was able to detect single molecule fluorescence in nanoapertures [26].

Another important application of plasmonic is in thin film solar cell. Active materials used in thin film solar cells are usually polycrystalline or amorphous silicon (p-Si or *a*-Si) because of their low cost, non-toxicity, abundance and mature processing technology. Yet, such great benefits are balanced by a short carrier diffusion length in silicon, resulting in a much lower conversion than that in crystalline solar cells. In order to achieve a nearly complete absorption the absorbing layer's thickness should be at least a few micrometers. Unfortunately, this is unrealistic due to high and defect-related carrier recombination [27]. As a result, improving the absorption in thin film Si solar cells has become crucial. Enhanced scattering by the subwavelength metallic structures both at surface plasmon resonance and near the resonance wavelength was found extremely useful in improving light absorption in thin film solar cells [28-29].

As shown in figure 1.11, at least three ways were proposed using plasmonic structures to reduce the physical thickness of the photovoltaic absorber layers while keeping their optical thickness constant [28]. First, metallic nanoparticles were put on the transparent top electrode (shown in figure 1.11a). Acting as subwavelength scattering elements, the particles bend the incident light, which result in an increase in the effective optical path length in the active layer. Second, metallic nanoparticles were put at the top electrode/active material interface (shown in figure 1.11a). The plasmonic near-field is coupled to the semiconductor, increasing its effective absorption cross-section. Third, a metallic grating is placed on the back side of active layer (shown in figure 1.11a). The

grating couples sunlight into SPP modes travelling parallel to the metal/semiconductor interface as well as guided modes in the active layer.

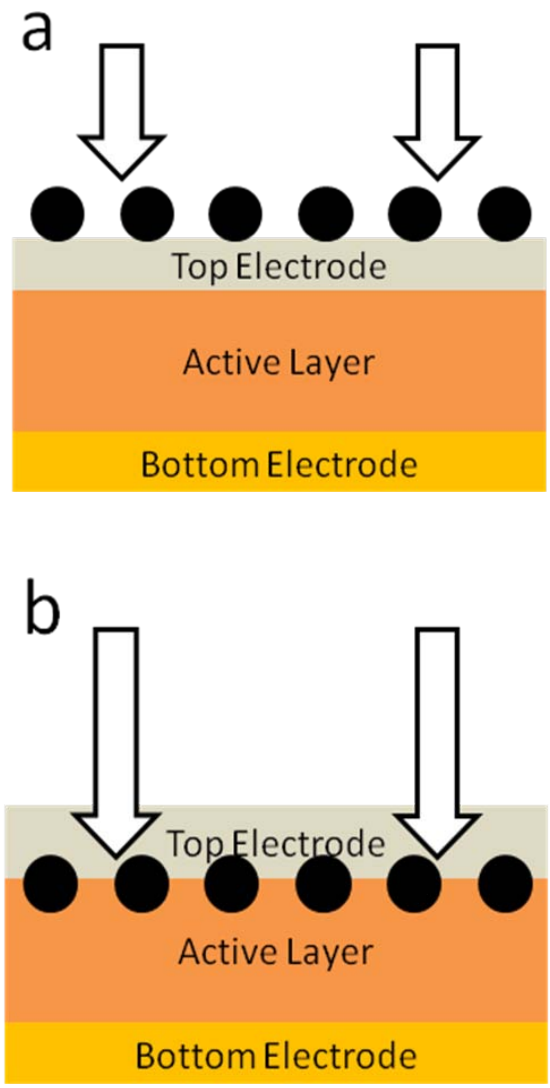

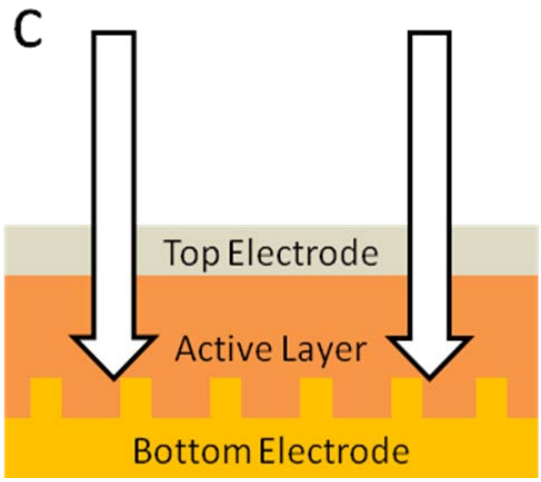

Figure 1.11: Plasmonic light-trapping structures for thin film solar cells. a) Light trapping by scattering by metal nanoparticles on the top of the transparent top electrode. Light is scattered and trapped into the absorbing layer by multiple scattering, causing an increase in the effective optical path length without changing the absorbing layer. b) Light trapping by the excitation of localized surface plasmons in metal nanoparticles at the top electrode/active mater interface. The strong electric field at the excited particles' proximity causes the creation of electron–hole pairs in the semiconductor. c) Light trapping by the excitation of surface Plasmon polaritons at the metallic electrode/active material interface. A grating structure on the back side of the active layer couples light to surface plasmon polariton or photonic modes that propagate in the plane of the active layer.

Plasmonic structures have provided a promising way of light-trapping, and have consistently drawn an increasing amount of attention. Au or Ag nanoparticles and nanogratings have been introduced to crystalline and amorphous silicon solar cells [29-39]. By coupling to surface plasmon and other photonic modes, a broadband and polarization-insensitive absorption enhancement as high as 30% was achieved, when comparing to bare thin film cells over the solar spectrum.

1.5 DISSERTATION OVERVIEW

This dissertation will be mainly focused on applying various plasmonic nanostructures in optical devices. In Chapter 2, I will proposes a metallic hole array of a rectangular converging-diverging channel (RCDC) shape with extraordinary transmission. A three-dimensional (3D) finite element method will be used to analyze the transmission characteristics of two-dimensional metallic hole arrays (2D-MHA) with RCDC. The length-width ratio (a/b) of the rectangular hole, the converging angle θ, and the metal film thickness t will be changed to study the effect of these parameters on the relationship between transmission and wavelength. In Chapter 3, Tunable extraordinary transmission via changing temperature of a porous metallic layer on top of a thin layer of dielectric strontium titanate (STO) will be studied. The metallic layer has a through-hole array and each hole has a circular converging-diverging channel (CDC) shape, which induces the excitation of surface plasmon polaritons (SPPs) and then results in a controllable extraordinary optical transmission in the terahertz (THz) frequency range. The converging angle, and the metal and STO thickness, were changed accordingly in the simulation to study the effect of such varying parameters on the relationship among transmission, wavelength, and temperature. In Chapter 4, a new thin film solar cell design, placing a metallic nanograting at the bottom of the optically active layer, will be proposed. This design will not only free up those photons blocked by surface nanostructures in previous designs, but also achieve a broadband and polarization-insensitive absorption enhancement by taking advantage of effective coupling to planar waveguide modes, the Fabry-Perot (FP) resonance and the SPPs resonance. The design will be carefully examined by the two-dimensional (2D) finite element method, and contribution from all above three mechanisms will be carefully analyzed. In chapter 5, a new nanograting solar cell design, which can be universal and a new solar cell platform

technology, was suggested with goals to achieve large enhancement on broadband light absorption and carrier generation, most importantly, under the much reduced usage of active and non-earth-abundant materials. A test for the short circuit current density in $CuIn_xGa_{(1-x)}Se_2$ (CIGS) thin film solar cells shows an up to ~250% enhancement when comparing to the corresponding bare thin film cells. Besides that, by placing metal strips on top of the nanograting, which act as the top electrode, this design is able to reduce the use of non-earth-abundant materials such as indium normally used in both active and transparent conducting materials. At last, chapter 6 will discuss the current work and the future recommendations.

REFERENCE

1. Mie, G., *Articles on the optical characteristics of turbid tubes, especially colloidal metal solutions.* ANNALEN DER PHYSIK 1908(25).
2. Ritchie, R.H., *Plasma losses by fast electrons in thin films.* PHYSICAL REVIEW 1957(106).
3. Maier, S.A., *Plasmonics: Fundamentals and Applications*. 1st. ed. 2007: Springer.
4. Raether, H., *Surface Plasmons on Smooth and Rough Surfaces and on Gratings*. 1988: Springer-Verlag. 136 pages.
5. Mulvaney, P., *Not all that's gold does glitter.* Mrs Bulletin, 2001. **26**(12): p. 1009-1014.

6. Maier, S.A. and H.A. Atwater, *Plasmonics: Localization and guiding of electromagnetic energy in metal/dielectric structures.* Journal of Applied Physics, 2005. **98**(1).

7. Jackson, J.D., *Classical Electrodynamics*. 3rd ed. 1998: Wiley.

8. BOHREN, C.F. and D.R. HUFFMAN, *Absorption and Scattering of Light by Small Particles*. First ed. 1983, New York, NY: John Wiley & Sons. Inc.

9. Sambles, J.R., G.W. Bradbery, and F.Z. Yang, *Optical-Excitation of Surface-Plasmons - an Introduction.* Contemporary Physics, 1991. **32**(3): p. 173-183.

10. OTTO, A., *EXCITATION OF NONRADIATIVE SURFACE PLASMA WAVES IN SILVER BY METHOD OF FRUSTRATED TOTAL REFLECTION.* ZEITSCHRIFT FUR PHYSIK, 1968(216): p. 398.

11. Maier, S.A., *Plasmonics: Fundamentals and Applications*. 1 edition ed. 2007: Springer. 223.

12. Ebbesen, T.W., et al., *Extraordinary optical transmission through sub-wavelength hole arrays.* Nature, 1998. **391**(6668): p. 667-669.

13. Cao, Q. and P. Lalanne, *Negative role of surface plasmons in the transmission of metallic gratings with very narrow slits.* Phys Rev Lett, 2002. **88**(5): p. 057403.

14. Lalanne, P., J.P. Hugonin, and J.C. Rodier, *Theory of surface plasmon generation at nanoslit apertures.* Phys Rev Lett, 2005. **95**(26): p. 263902.

15. Lezec, H.J. and T. Thio, *Diffracted evanescent wave model for enhanced and suppressed optical transmission through subwavelength hole arrays.* Optics Express, 2004. **12**(16): p. 3629-3651.

16. Qu, D.X., D. Grischkowsky, and W.L. Zhang, *Terahertz transmission properties of thin, subwavelength metallic hole arrays.* Optics Letters, 2004. **29**(8): p. 896-898.

17. Cao, H. and A. Nahata, *Influence of aperture shape on the transmission properties of a periodic array of subwavelength apertures.* Optics Express, 2004. **12**(16): p. 3664-3672.

18. Degiron, A., et al., *Effects of hole depth on enhanced light transmission through subwavelength hole arrays.* Applied Physics Letters, 2002. **81**(23): p. 4327-4329.

19. Azad, A.K. and W.L. Zhang, *Resonant terahertz transmission in subwavelength metallic hole arrays of sub-skin-depth thickness.* Optics Letters, 2005. **30**(21): p. 2945-2947.

20. Pan, C.L., et al., *Control of enhanced THz transmission through metallic hole arrays using nematic liquid crystal.* Optics Express, 2005. **13**(11): p. 3921-3930.

21. Steele, J.M., et al., *Resonant and non-resonant generation and focusing of surface plasmons with circular gratings.* Optics Express, 2006. **14**(12): p. 5664-5670.

22. Koerkamp, K.J.K., et al., *Strong influence of hole shape on extraordinary transmission through periodic arrays of subwavelength holes.* Physical Review Letters, 2004. **92**(18).

23. Battula, A., et al., *Tunable transmission at 100 THz through a metallic hole array with a varying hole channel shape.* Optics Express, 2007. **15**(22): p. 14629-14635.

24. Wang, W., et al., *Tunable and polarization-selective THz range transmission properties of metallic rectangular array with a varying hole channel shape.* Optics Express, 2009. **17**(9): p. 7361-7367.

25. Porto, J.A., L. Martin-Moreno, and F.J. Garcia-Vidal, *Optical bistability in subwavelength slit apertures containing nonlinear media.* Physical Review B, 2004. **70**(8).

26. Wenger, J., et al., *Single molecule fluorescence in rectangular nano-apertures.* Optics Express, 2005. **13**(18): p. 7035-7044.

27. Shah, A.V., et al., *Thin-film silicon solar cell technology.* Progress in Photovoltaics, 2004. **12**(2-3): p. 113-142.

28. Atwater, H.A. and A. Polman, *Plasmonics for improved photovoltaic devices.* Nature Materials, 2010. **9**(3): p. 205-213.

29. Hallermann, F., et al., *On the use of localized plasmon polaritons in solar cells.* Physica Status Solidi a-Applications and Materials Science, 2008. **205**(12): p. 2844-2861.

30. Rockstuhl, C., S. Fahr, and F. Lederer, *Absorption enhancement in solar cells by localized plasmon polaritons.* Journal of Applied Physics, 2008. **104**(12).

31. Pala, R.A., et al., *Design of Plasmonic Thin-Film Solar Cells with Broadband Absorption Enhancements.* Advanced Materials, 2009. **21**(9999): p. 1-6.

32. Schaadt, D.M., B. Feng, and E.T. Yu, *Enhanced semiconductor optical absorption via surface plasmon excitation in metal nanoparticles.* Applied Physics Letters, 2005. **86**(6).

33. Panoiu, N.C. and R.M. Osgood, *Enhanced optical absorption for photovoltaics via excitation of waveguide and plasmon-polariton modes.* Optics Letters, 2007. **32**(19): p. 2825-2827.

34. Pillai, S., et al., *Surface plasmon enhanced silicon solar cells.* Journal of Applied Physics, 2007. **101**(9).

35. Derkacs, D., et al., *Improved performance of amorphous silicon solar cells via scattering from surface plasmon polaritons in nearby metallic nanoparticles.* Applied Physics Letters, 2006. **89**(9).

36. Stenzel, O., et al., *ENHANCEMENT OF THE PHOTOVOLTAIC CONVERSION EFFICIENCY OF COPPER PHTHALOCYANINE THIN-FILM DEVICES BY INCORPORATION OF METAL-CLUSTERS.* Solar Energy Materials and Solar Cells, 1995. **37**(3-4): p. 337-348.

37. Westphalen, M., et al., *Metal cluster enhanced organic solar cells.* Solar Energy Materials and Solar Cells, 2000. **61**(1): p. 97-105.

38. Ferry, V.E., et al., *Plasmonic Nanostructure Design for Efficient Light Coupling into Solar Cells.* Nano Letters, 2008. **8**(12): p. 4391-4397.

39. Wang, W., et al., *Broadband Light Absorption Enhancement in Thin-Film Silicon Solar Cells.* Nano Letters, 2010. **10**(6): p. 2012-2018.

Chapter 2: Tunable and polarization-selective THz range transmission properties of metallic rectangular array with a varying hole channel shape

This chapter proposes a metallic hole array of a rectangular converging-diverging channel (RCDC) shape with extraordinary transmission. We use a three-dimensional (3D) finite element method to analyze the transmission characteristics of two-dimensional metallic hole arrays (2D-MHA) with RCDC. For a straight channel MHA, when the aperture size is reduced, the transmission peaks have a blue-shift. The same result is observed for a smaller gap throat for the RCDC structure. For the rectangular holes with a high length-width ratio, a similar blue-shift in the transmission peaks as well as a narrower full width at half maximum (FWHM) are observed. The asymmetry from the rectangular shape gives this structure high selectivity for light with different polarizations. Furthermore, the RCDC shape gives extra degrees of geometrical variables to 2D-MHA for tuning the location of the transmission peak and the FWHM. The tunable transmission property of this structure shows promise for applications in nanolithography, imaging, and bio-sensing.

2.1 Introduction

In 1998, extraordinary optical transmission (EOT) phenomenon was reported by T. W. Ebbesen and his coworkers. EOT was achieved through subwavelength metallic hole arrays (MHAs) milled in an opaque metal screen [1]. This work generated considerable interest and led to the development of a new family of optical devices based on subwavelength hole arrays with tunable transmission spectrums via adjustable array properties (periodicity, thickness of the film, etc.). There have been arguments about the

main cause of this high transmission through subwavelength holes [2-4]; however, more and more researchers in this area are beginning to believe that enhanced transmission through subwavelength MHA can be divided into three steps: the coupling of light to SPPs on the incident surface, the transmission through the holes and the re-emission from the second surface. EOT in the terahertz (THz) region has been observed recently in both metallic [5-8] and semiconductor hole arrays [9-11]. Although metal surfaces in this frequency region act as perfect conductors and the SPPs excitation cannot be expected, it has been proven both experimentally [12] and theoretically [13] that the resonantly-excited SPP-like mode plays an important role in high transmission in the THz region.

Photonic structures have several geometric variables, such as film thickness, interface media, periodicity, hole shape, aperture size, etc., that can be used to manipulate the light propagation at the subwavelength scale. As mentioned above, the high transmission is caused by the coupling interaction of the SPPs on both the incident and the transmitted surfaces and is strongly affected by the thickness of the metal film. The transmission decreases exponentially with increasing depth [14], and the SPPs on the two surfaces are uncoupled when the hole depth is large. It is observed in the THz region that the EOT can be achieved at an array thickness of only one third of the skin depth [15]. It has also been shown that the peak transmission has a red-shift as the index of refraction inside the metallic hole arrays undergoes an increase [16]. Similarly, when the surrounding dielectric constant increases, a red-shift along with a reduction in the transmission magnitude is observed [9]. In addition to the parameters that have already been discussed, periodicity is also very important. It has been reported that a planar circular grating with the period of the rings matching the SPP wavelength can have enhanced intensity at the focal point of the plasmonic lens [17]. Different hole shapes have also been studied. A circular hole shape has an order of magnitude higher

normalized transmission than a rectangular shape, along with a large blue-shift spectrum [18]. Also, the different influence of the hole shape in the THz region from that in the optical region has been studied [5-6].

The hole size along with the channel shape will have significant impact on the transmission efficiency because the holes are expected to mediate the SPP coupling between both surfaces of the metal film. Recently we have proposed a subwavelength hole array having a converging diverging channel (CDC) with a circular hole shape [19]. This CDC-shaped hole array offers similar EOT effects, yet has an extra degree of freedom in a geometric variable, the converging angle, to tune the transmission spectrum. The converging angle determines the slope of the sidewall and the area at the throat of the CDC channels (Fig. 2.1). The transmission spectrum was studied for a 2D-MHA with variable throat and aperture size and was compared with a straight channel array. The results show that when the channel shape is changed to CDC the transmittance peaks become narrower and there is a blue-shift. The blue-shift becomes larger as the throat area decreases.

In this chapter, we propose to use a rectangular converging-diverging channel (RCDC) to study the EOT properties for light with different polarizations. The proposed structure has another geometric variable, the length-width ratio of the rectangle that can be used to tune the transmission properties. More importantly, this structure has a strong selectivity for different polarizations.

2.2 COMPUTATIONAL CONSIDERATIONS

Figure 2.1 shows a side view of the structure used for the simulation where the incident light goes through a thin film of silver. The thickness of the film is t, and there is

a rectangular RCDC hole array with a converging angle θ in it. The transmission vs. wavelength curve was calculated for different geometric variables. Figure 2.2 shows the top surface of the silver film. The rectangular hole array is periodic in both the x and y directions, and the periodicity for the two directions are the same (22μm). The inset shows the top view of a single rectangular hole, with a and b defined as the long and short sides. The lengths of the two sides are not identical, resulting in an asymmetric structure along the x and y directions. Transmissions are expected to change with different polarizations of the incident light. In fact, we will show that such a structure has a very high selectivity of transmission with different polarizations and can be used as a polarization-selective filter.

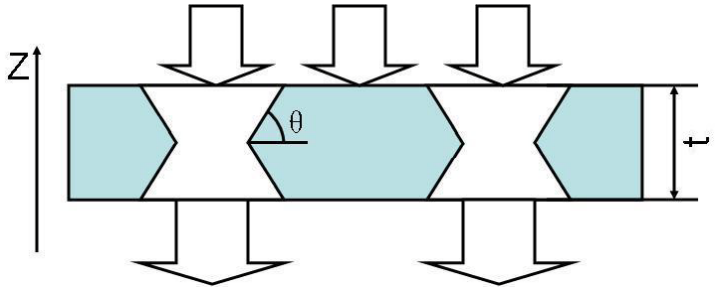

Figure 2.1: Side view of the structure. The thickness of the film is t, and there is a rectangular RCDC hole array with a converging angle θ in it.

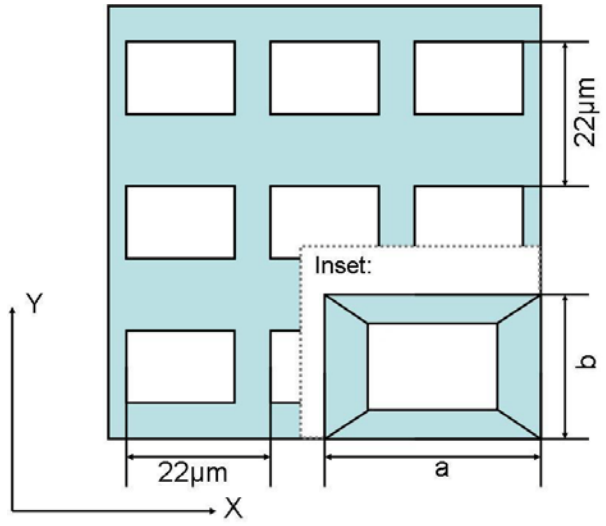

Figure 2.2: Top surface of the structure. The rectangular hole array is periodic in both the x and y directions, and the periodicity for the two directions are the same (22 μm). The inset shows the top view of a single rectangular hole, with a and b defined as the long and short sides. The lengths of the two sides are not identical, resulting in an asymmetric structure along the x and y directions.

In this chapter, we will change the length-width ratio (a/b), the converging angle θ, and the metal film thickness t, while keeping the other parameters unchanged to study the effect of these parameters on the relationship between transmission and wavelength.

For this study we considered the frequency to be around 15 THz or 20μm wavelength. The dielectric constant of silver used in the simulation was described by the Drude model $\varepsilon = \varepsilon_\infty - \omega_p^2 / (\omega^2 + i\gamma\omega)$, where $\varepsilon_\infty = -175.0$, $\omega_p = 1.1 \times 10^{16}\ s^{-1}$, and $\gamma = 10.51 \times 10^{13}\ s^{-1}$ [20]. The electromagnetic fields were assumed to be time harmonic and the resulting governing equations for the steady-state distribution was solved using a commercially available 3-dimensional (3D) finite element software (COMSOL 3.3) [21]. The computational domain considered is a single unit cell surrounded either by periodic boundary conditions or by perfectly matching layers (PML) [22].

2.3 RESULTS AND DISCUSSIONS

2.3.1 Results for different a/b ratios

Figure 2.3 (a-c) shows the transmission spectrums for Ag MHAs having different a/b ratios. For all the cases, the hole area, the converging angle (30^o) and the metal film thickness (2 μm) are kept the same. The solid and dashed lines show the transmissions for different polarizations (solid line: E-field parallel to the short side; dash line: E-field parallel to the long side). Since these 2D structures are asymmetric along their short and long sides, the polarization becomes a very crucial parameter for the transmission peak. In the case of polarization (i.e., E-field) parallel to the long sides of the rectangles, there is negligible transmission. When the incident polarization is rotated 90^o to point along the rectangles' minor sides, the aperture transmits a substantial fraction of the incident light, in agreement with the result reported previously [23].

The transmission spectrum changes as the a/b ratio increases, but the magnitude of the transmission peak remains the same and is much larger than $(A/\lambda)^4$, the Bethe-Bouwkamp power law model. In this model, 'A' is the aperture size and 'λ' is the wavelength of the light. By changing the a/b ratio, we can tune the position of the band and the full width at half maximum (FWHM). For example, decreasing the a/b ratio causes an increase in the FWHM of the transmission peaks accompanied by a red-shift. At the frequencies below the cutoff frequency ω_c (the frequencies at which the transmission reaches half maximum of the peak), the curves are very sharp and the transmissions rapidly drop to 0.1. This means the RCDC structures with different a/b ratios are all very good filters for low frequencies.

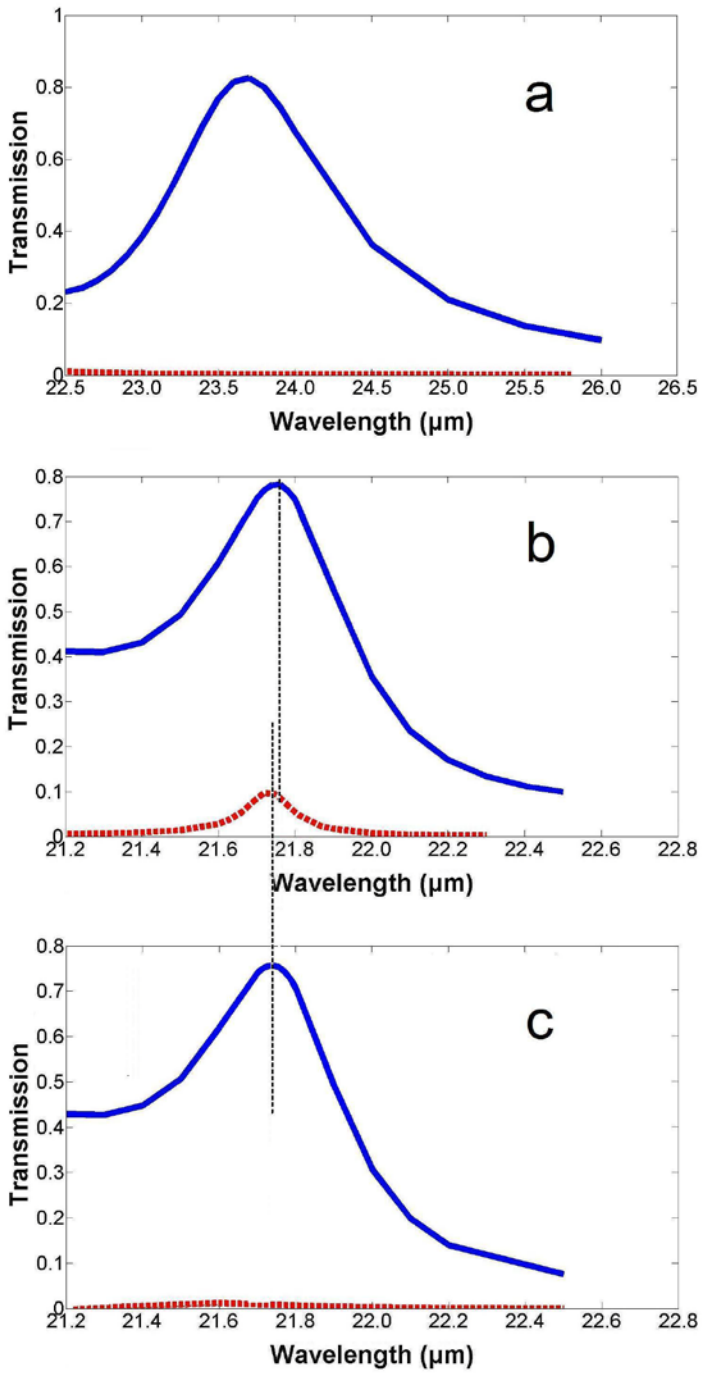

Figure 2.3: Transmittance spectrum with the same hole area and converging angle θ=30o, but different a/b ratios (a) a=16 μm, b=12 μm, (b) a=18 μm, b=10.7 μm, and (c) a=20 μm, b=9.6 μm. The solid and dashed lines represent the transmissions for different polarizations. The vertical dashed lines denote the wavelength of each peak.

2.3.2 Results for different converging angles

Figure 2.4 shows the transmission spectrum for Ag MHAs with different converging angles while keeping the same hole area, a/b ratio (16μm/12μm) and film thickness (2μm). The two sets of simulation data show a high-selectivity for different polarizations. Similar to the results in section 3.1, the transmission spectra for an E-field perpendicular to the long side has a strong peak for each converging angle in this wavelength range, while there is no peak in the range of our interest for the case of an E-field parallel to the long side. The position of the peaks and the FWHM can be tuned by changing the converging angle. Figure 2.4 shows that the location of the peak blue shifts nearly linearly as the converging angle decreases. Moreover, since the throat size varies as the converging angle changes, the magnitudes of the transmission peak and the FWHM increase as the angle increases. Interestingly, the change of magnitude with respect to the angle is nearly linear. For frequencies beyond the cut off frequency ω_c, the transmissions drop rapidly, indicating the potential application as band-pass filters.

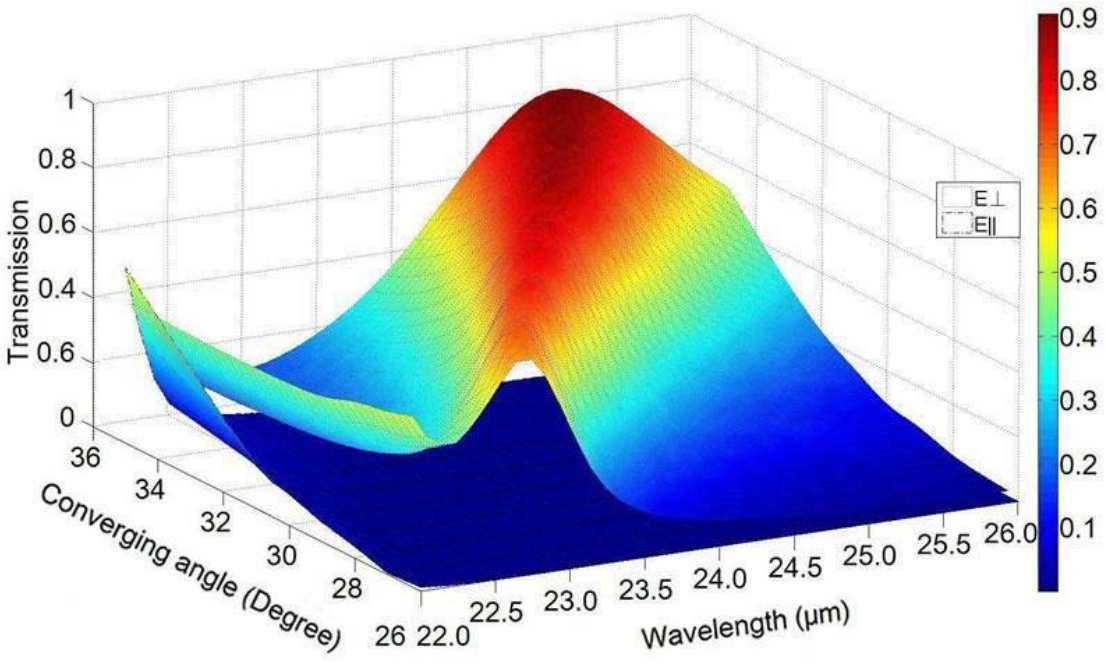

Figure 2.4: Transmissions for different converging angles. The hole area, film thickness and a/b ratio (16μm/12μm) remain the same in all cases.

2.3.3 Results for different metal film thickness

Figure 2.5 shows the transmission spectrum for Ag MHAs with different metal film thicknesses while keeping the same hole area, a/b ratio (16μm/12μm) and converging angle (30^o). The solid and the dashed lines are for different polarizations. Similar to the results in sections 3.1 and 3.2, the transmissions are highly selective—there are strong transmission peaks only for the cases of E-field perpendicular to the long side. But the difference is that, since we extend our study to shorter wavelengths, there are two transmission peaks for some cases. As the thickness increases, one of the peaks stays almost at the same location (~21.8μm), yet the location of the other peak blue shifts. The behavior of these two peaks may be due to the excitation of two types of electromagnetic modes as mentioned previously [24]: coupled SPPs and waveguide resonances. The

nearly fixed peaks are excited by coupled SPPs whose locations are not sensitive to the film thickness, whereas the other peaks are caused by the waveguide resonances.

From t=2.0μm to 2.5μm, the transmission peaks due to the waveguide resonances blue shift and both the magnitude and the FWHM of the peaks decrease resulting from the reduced throat area. However, the magnitudes of the peaks related to SPPs increase as the thickness increases. One possible reason is as the waveguide resonances peak blue shifts, the two peaks come closer and the interaction between them becomes stronger. When t=2.5μm, the interactions are so strong that the location of the SPPs peak red shifts a little. For the case of t=3.0μm, however, only the SPPs peak is left and it is relatively small (<0.5). This shows that without the contribution of the waveguide resonance, the magnitude of the SPPs peak will decrease with an increasing film thickness.

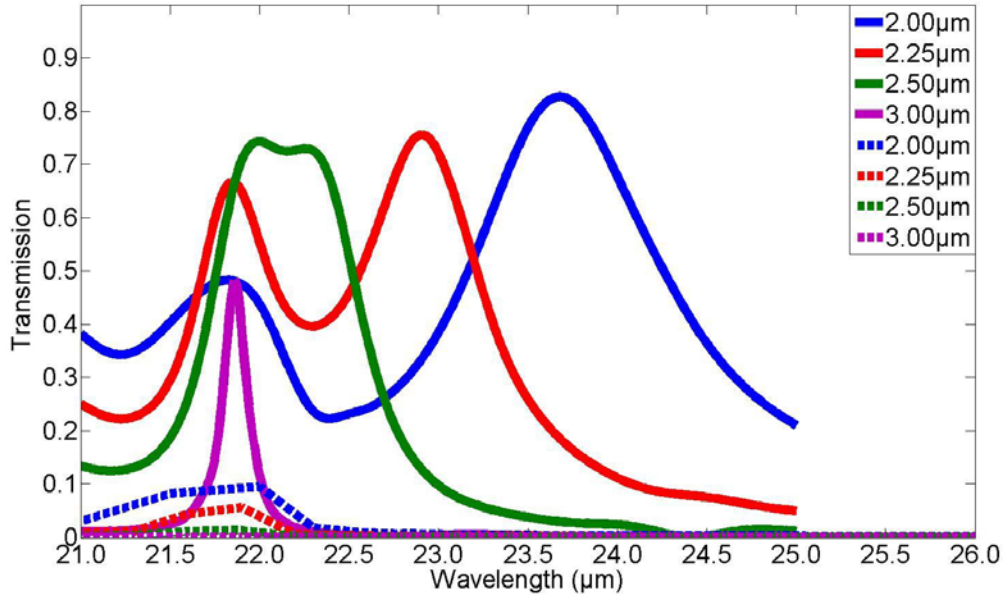

Figure 2.5: Transmissions for different metal film thickness. The hole area, converging angle (30^{o}) and a/b ratio remain the same in all cases. The solid and dashed lines represent the transmissions for different polarizations.

2.4 Conclusion

The transmission spectrums of metallic hole arrays with different converging-diverging channels have been discussed in this chapter. Since the structure is asymmetric along the x and y directions, it is highly selective for different polarizations, providing a potential application as a polarized optical filter. Meanwhile, by changing the a/b ratio, the converging angle and the metal film thickness, the transmission properties can be changed. As a result, this proposed RCDC shape in MHAs could lead to extraordinary transmission at different wavelengths and can be used to develop THz polarized filters. This could lead to a wide range of applications in tunable filters, photonic circuits, nanopatterning, and biosensors.

REFERENCE

1. Ebbesen, T.W., et al., *Extraordinary optical transmission through sub-wavelength hole arrays.* Nature, 1998. **391**(6668): p. 667-669.

2. Cao, Q. and P. Lalanne, *Negative role of surface plasmons in the transmission of metallic gratings with very narrow slits.* Phys Rev Lett, 2002. **88**(5): p. 057403.

3. Lalanne, P., J.P. Hugonin, and J.C. Rodier, *Theory of surface plasmon generation at nanoslit apertures.* Phys Rev Lett, 2005. **95**(26): p. 263902.

4. Lezec, H.J. and T. Thio, *Diffracted evanescent wave model for enhanced and suppressed optical transmission through subwavelength hole arrays.* Optics Express, 2004. **12**(16): p. 3629-3651.

5. Qu, D.X., D. Grischkowsky, and W.L. Zhang, *Terahertz transmission properties of thin, subwavelength metallic hole arrays.* Optics Letters, 2004. **29**(8): p. 896-898.

6. Cao, H. and A. Nahata, *Influence of aperture shape on the transmission properties of a periodic array of subwavelength apertures.* Optics Express, 2004. **12**(16): p. 3664-3672.

7. Miyamaru, F. and M. Hangyo, *Finite size effect of transmission property for metal hole arrays in subterahertz region.* Applied Physics Letters, 2004. **84**(15): p. 2742-2744.

8. O'Hara, J.F., R.D. Averitt, and A.J. Taylor, *Terahertz surface plasmon polariton coupling on metallic gratings.* Optics Express, 2004. **12**(25): p. 6397-6402.

9. Azad, A.K., Y. Zhao, and W. Zhang, *Transmission properties of terahertz pulses through an ultrathin subwavelength silicon hole array.* Applied Physics Letters, 2005. **86**(14).

10. Rivas, J.G., et al., *Enhanced transmission of THz radiation through subwavelength holes.* Physical Review B, 2003. **68**(20).

11. Janke, C., et al., *Optimization of enhanced terahertz transmission through arrays of subwavelength apertures.* Physical Review B, 2004. **69**(20).

12. Tanaka, M., et al., *Effect of a thin dielectric layer on terahertz transmission characteristics for metal hole arrays.* Optics Letters, 2005. **30**(10): p. 1210-1212.

13. Pendry, J.B., L. Martin-Moreno, and F.J. Garcia-Vidal, *Mimicking surface plasmons with structured surfaces.* Science, 2004. **305**(5685): p. 847-848.

14. Degiron, A., et al., *Effects of hole depth on enhanced light transmission through subwavelength hole arrays.* Applied Physics Letters, 2002. **81**(23): p. 4327-4329.

15. Azad, A.K. and W.L. Zhang, *Resonant terahertz transmission in subwavelength metallic hole arrays of sub-skin-depth thickness.* Optics Letters, 2005. **30**(21): p. 2945-2947.

16. Pan, C.L., et al., *Control of enhanced THz transmission through metallic hole arrays using nematic liquid crystal.* Optics Express, 2005. **13**(11): p. 3921-3930.

17. Steele, J.M., et al., *Resonant and non-resonant generation and focusing of surface plasmons with circular gratings.* Optics Express, 2006. **14**(12): p. 5664-5670.

18. Koerkamp, K.J.K., et al., *Strong influence of hole shape on extraordinary transmission through periodic arrays of subwavelength holes.* Physical Review Letters, 2004. **92**(18).

19. Battula, A., et al., *Tunable transmission at 100 THz through a metallic hole array with a varying hole channel shape.* Optics Express, 2007. **15**(22): p. 14629-14635.

20. Palik, E.D., *Handbook of Optical Constants of Solids*. 1985: Academic.

21. *COMSOL 3.3 Reference Manual*. version 3.3 ed. 2005.

22. Lavrinenko, A., et al., *Comprehensive FDTD modelling of photonic crystal waveguide components.* Optics Express, 2004. **12**(2): p. 234-248.

23. Zakharian, A.R., M. Mansuripur, and J.V. Moloney, *Transmission of light through small elliptical apertures.* Optics Express, 2004. **12**(12): p. 2631-2648.

24. Porto, J.A., F.J. Garcia-Vidal, and J.B. Pendry, *Transmission resonances on metallic gratings with very narrow slits.* Physical Review Letters, 1999. **83**(14): p. 2845-2848.

Chapter3: Tuning the extraordinary transmission in a metallic/dielectric CDC hole array by changing the temperature

Tunable extraordinary transmission via changing temperature of a porous metallic layer on top of a thin layer of dielectric strontium titanate (STO) was studied. The metallic layer has a through-hole array and each hole has a circular converging-diverging channel (CDC) shape, which induces the excitation of surface plasmon polaritons (SPPs) and then results in a controllable extraordinary optical transmission in the terahertz (THz) frequency range. We used a three-dimensional (3D) finite element method to analyze the transmission characteristics of the structure. Location and magnitude of the transmission peaks can be adjusted by hole size, converging angle, and thicknesses of metal and STO layers. Remarkably, the suggested structure presents a strong transmission dependency on temperature, which offers a new approach to actively and externally tune the transmission. This new design could lead to a family of temperature-sensitive devices working in the THz frequency range, promising in many applications including photonics, nanolithography, imaging, and sensing.

3.1 INTRODUCTION

The terahertz (THz) frequency band, which lies between domains of microwave electronics and mid infrared optics, has received increasing attentions recently because of its possible applications in fundamental science, new imaging and sensing modalities, and high bandwidth signal processing [1]. Examples of such applications include communication [2], medical imaging [3], pharmaceutical quality control [4], and chemical and biochemical sensing [5]. Utilizing the light in the THz band, however, requires a precise control of the wave propagation as well as the electromagnetic field

distribution. For example, in the applications as THz filters, photonic circuits, and sensors, control of the transmission spectrum, especially a capability of active and precise frequency tuning, is highly desirable.

The extraordinary optical transmission (EOT) phenomenon was first reported by T. W. Ebbesen *et. al.* in 1998 [6]. This work has generated considerable interests in recent years and led to the development of a new family of optical devices based on subwavelength hole arrays with extraordinary transmission spectra. This unique phenomenon is believed to be due to the SPPs excited at the metal/dielectric interface [7-9]. Although metal surfaces in the THz frequency region act as perfect conductors making SPPs excitation unexpected, EOT has been observed recently in both metallic [10-12] and semiconductor [13-15] hole arrays, and it has been proven both experimentally and theoretically that the resonantly-excited SPP-like mode plays an important role in the much enhanced transmissions [16-17]. Excited by Ebbesen's pioneer work, intensive studies were done to analyze the tunability of the transmission. By changing the geometric variables (film thickness, interface media, periodicity, hole shape, aperture size, channel shape, etc.), the transmission properties (magnitude, location of the peaks, the full width at half maximum (FWHM), and selectivity of different polarization) can be tuned correspondingly [10-11, 18-24].

However, tuning by changing the geometry variables indicates either deforming or replacing the device will be required, and is not active. This actually limits their future applications in real-time systems. Previous work has shown that the transmission of light through a thin Ag film with a specifically designed periodic subwavelength hole array can be influenced by the presence of the externally applied magnetic field [25], which indeed indicates an initial move toward the active frequency tuning direction. Considering the fact that SPPs strongly rely on the metal/dielectric interface,

modification of the interface would become an effective route for realizing the active tuning, and recent development of dielectric materials with a strong non-linear response [26] will actually support the idea. Here, the term “non-linear response” means their optical properties can be controlled by external parameters (temperature, electric or magnetic field, light pulse, etc.). Among these non-linear materials, so called incipient ferroelectric materials [27] such as strontium titanate ($SrTiO_3$, STO) or potassium tantalate ($KTaO_3$, KTO) exhibit a potential to realize the large frequency range and active tuning. For example, between 0.3 THz to 0.9 THz, i.e. wavelengths between 300 μm to 1 mm, both real and imaginary parts of permittivity of STO undergo an increase as temperature decreases [26]. This unique property offers a new way to design strong temperature-dependent devices working in the THz band.

In this work, we propose a new structure with a metallic layer on top of a thin layer of the STO. The metallic layer has a through-hole array with a circular, converging-diverging channel (CDC) shape. Use of the CDC shape has been proven with similar EOT effect, in addition, with an extra degree of freedom in a geometric variable to further fine-tune the transmission spectrum [23]. Simulations were performed to study the EOT properties under different temperature conditions. By careful design of the converging angle and STO layer thickness, the proposed structure can function well at certain THz bands with a realistic transmission spectrum profile. More importantly, the strong transmission dependency on temperature provides us the capability to modulate the transmission without using deformation or replacement—a true active frequency tuning.

3.2 SIMULATION CONSIDERATIONS

Figure 3.1 shows a side view of the proposed structure used for the simulation where the incident light transmits through the thin layers of silver and STO. Their thicknesses are t_1 and t_2, respectively. There is a circular CDC hole array with a semi converging angle θ in the silver layer [23]. The radii of the holes at surface are fixed at 20 μm. The transmission was calculated for different wavelengths, temperatures and geometric variables. Figure 3.2 shows the top view of the silver film. The circular hole array is periodic in both the x and y directions, and the periodicity for the two directions are the same (50 μm). The inset shows the details of a single circular hole.

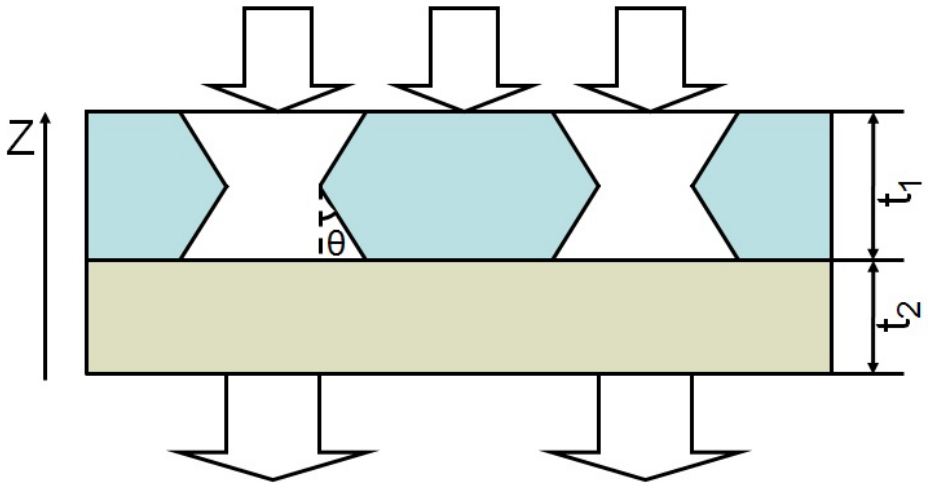

Figure 3.1: The side view of the device structure. The thickness for the metallic layer is t_1, the thickness for the dielectric layer with a temperature dependent dielectric constant is t_2, and a circular CDC hole array with a semi-angle θ will be made inside the metallic layer.

The converging angle, θ, and the metal and STO thickness, t_1 and t_2, were changed accordingly in the simulation, while keeping all other parameters unchanged. The goal is to study the effect of such varying parameters on the relationship among transmission, wavelength, and temperature. For this study we considered the frequency to

be around 0.6THz or 450 μm wavelength and the temperature range to be from 270K to 305K. The dielectric constant of STO was described by a damped harmonic oscillator model: $\varepsilon = \varepsilon_\infty + f^2 / (\omega_0^2 - \omega^2 - i\gamma_t\omega)$, where $\omega_0(T)[cm^{-1}] = \sqrt{31.2(T-42.5)}$, $\gamma(T)[cm^{-1}] = -3.3 + 0.094T$, $f = 2.3\times10^6 cm^{-2}$ [26]. The dielectric constant of silver used in the simulation was described by the Drude model $\varepsilon = \varepsilon_\infty - \omega_p^2 / (\omega^2 + i\gamma_s\omega)$, where $\varepsilon_\infty = 1$, $\omega_p = 1.44 \times 10^{16}\ s^{-1}$, and $\gamma_s = 4 \times 10^{13}\ s^{-1}$ [28]. Within the suggested temperature range in our calculation, the dielectric constant of silver is set to be temperature independent. The electromagnetic fields were assumed to be time harmonic and the resulting governing equations for the steady-state distribution was solved using commercially available three-dimensional (3D) finite element software (COMSOL 3.3). The computational domain considered is a single unit cell surrounded either by periodic boundary conditions or by perfectly matching layers (PML) [29]. The light is incident normal to the film surface and the transmittance is calculated from the obtained electromagnetic field distributions.

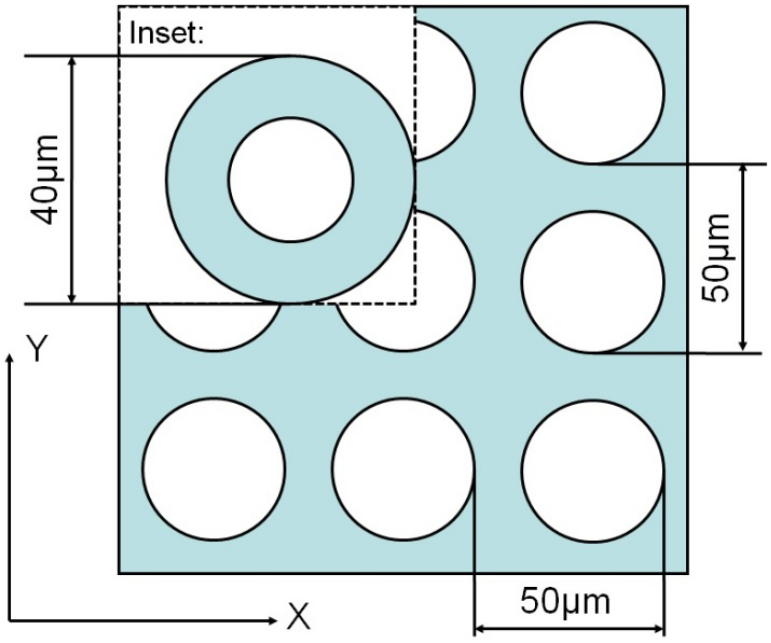

Figure 3.2: The top view of the structure. The circular hole array is periodic in both the x and y directions, and the periodicity for the two directions are the same (50μm). The inset shows the top view of a single circular hole.

3.3 RESULTS AND DISCUSSION

Figure 3 shows the transmission vs. temperature and wavelength for the structure having various geometric variables. To better evaluate the transmission property, all figures in Fig. 3 were plotted at the same scale. All the figures shown are characterized by their strong transmission peaks which are much larger than $(A/\lambda)^4$, the Bethe-Bouwkamp power law model [30]. In this model, 'A' is the aperture size and 'λ' is the wavelength of the light. This indicates the existence of EOT inside the proposed structure. Further examination reveals that the transmission spectrum changes as both temperature and geometry change. Let's first look at the transmission's dependency on temperature. Each figure in Fig. 3 shows the full transmission spectrum under certain geometric conditions. Since a higher temperature results in both smaller imaginary and

real parts of the dielectric constant of the STO material, the magnitude of the transmission peak increases and the peak blue-shifts as the temperature increases.

To better study the role of changing both temperature and converging angle, we compare Fig. 3a-c altogether. Responses from both CDC and the straight-hole array due to a temperature change of 36 K are re-plotted in Fig. 4. When changing the temperature 36 K around the room temperature as shown in Fig. 4a, the transmission peak's location and magnitude among all cases change about 33 μm, which is about 3% central to the transmission wavelength. This indicates a fairly large frequency tunable range, and is actually practical for many long wavelength photonics application. Another remarkable benefit is that these transmission properties are nearly linearly dependent on temperature. Moreover, the full width at half maximum (FWHM) is relatively independent of temperature change, which remains to be around 60 μm.

For the hole-arrayed metal/dielectric structure, an increase in the angle θ actually gives rise to a decrease in transmission, which is slightly different from the case without the dielectric layer [23]. However, it shows a blue-shifted transmission when increasing the angle θ, indicating an additional manipulation over the transmission by changing the angle is possible. Fig. 4b shows the different transmission spectra at different converging angles at 269 K. As the apertures in the metal layer change from straight-channel to the CDC shape with a converging angle of 60º, the peak transmission reduces from 20.1% to 15.8% with a blue shift of ~32 μm, and the FWHM of those peaks is actually becoming narrower too. The results here indicate, for the suggested metal/dielectric structure, introducing CDC to the design is not beneficial to the transmission amplitude, but does add a freedom in fine-adjusting the peak position and in modifying the FWHM of the transmission.

The comparison of Fig. 3b and 3d reveals the transmission dependency on the metal film thickness. With the same converging angle and temperature, the magnitude of the transmission peak is much lower for a thicker metal layer. Also, as the metal layer thickness increases, the location of the transmission peak red-shifts at the same time. It is important to point out that Fig. 3c (using a larger converging angle) and 3d (using a thicker metal layer thickness) show very closed transmission spectrum, which indicates that adding the CDC design to the structure can provide not only an extra degree of freedom to fine-tune the transmission properties, but also as an important substitution to change other geometric variables, for example, here to use less amount of metallic material.

The thickness of STO the layer also plays an important role in the transmission properties. Fig. 3b, 3e and 3f show the transmission spectrum with a same converging angle of 45^{o} for different STO thicknesses. Although all the transmission peaks in the three plots are still much larger than those predicted by the Bethe-Bouwkamp power law model, the magnitude of each peak is much lower for a thicker layer of STO. Along with magnitude reduction, the location of the transmission peak red-shifts at the same time. Since STO is not a lossless material, the reduction of transmission results from the increased energy loss in longer travel distance in the absorbing material. In the case of our simulation, as shown in Figure 3, when the STO layer thickness increases from 1.5 μm to 2.5 μm, a steep magnitude drop of the transmission peaks of around 10% with a red shift of nearly 100 μm is observed. The dramatic transmission change suggests that the STO layer thickness is a crucial parameter on which special attention is needed to meet the desired performance requirement. A further investigation over the case having holes all the way through the metal/dielectric structure will be also interesting, and this is an ongoing effort.

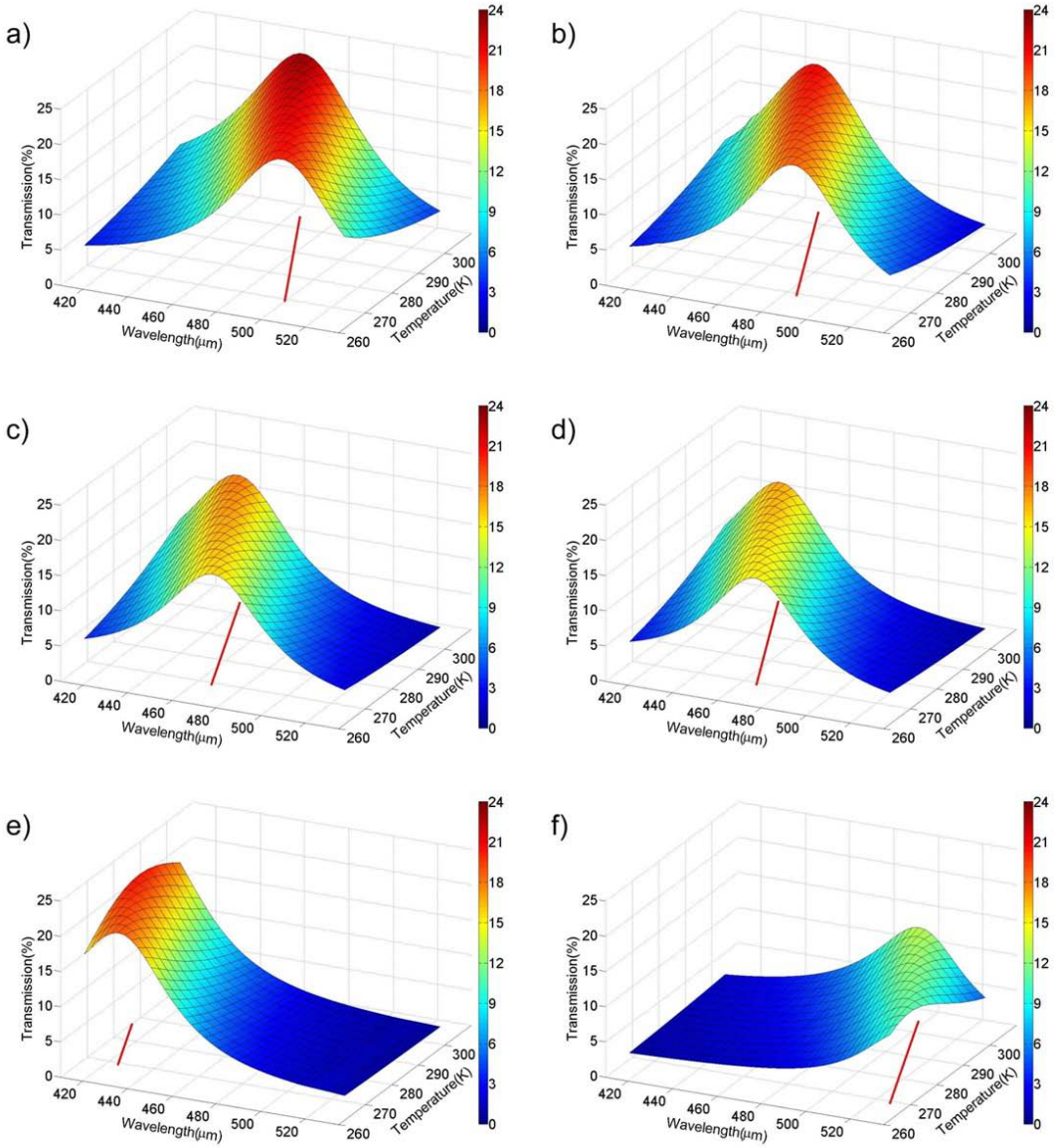
a)
b)
c)
d)
e)
f)
Transmission(%)
Wavelength(μm)
Temperature(K)

Figure 3.3: Transmittance spectrum with different geometric variables and temperatures. (a)-(c) are plots of transmission versus wavelength and temperature with converging angle (a) 0^o, (b) 45^o, and (c) 60^o. Thickness of the metal and STO layer are both fixed at 2 μm. (d) shows the case at which the thickness of the metal and STO are 3 μm and 2 μm, respectively. The converging angle is 45^o. (e) and (f) show the transmittance spectrums with the same metal film thicknesses (2 μm) and converging angle (45^o), but with different STO layer thicknesses: (e) t_2 = 1 μm and (f) t_2 = 2.5 μm. For all cases above, the hole area is unchanged. The transmission peak vs. temperature curve is shown at the bottom in each figure (red curve).

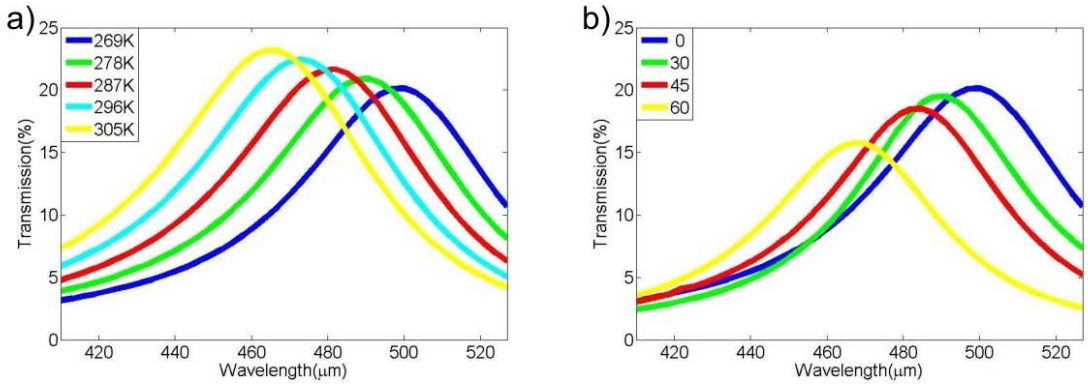

Figure 3.4: Transmittance spectrum curves. (a) shows transmission spectrum with different temperatures. The converging angles are fixed at 0^o (straight hole) for all cases. (b) shows transmission spectrum with different converging angles. The temperatures are fixed at 269 K for all cases.

3.4 CONCLUSION

We have investigated the transmission spectra of metallic hole arrays with different converging-diverging channels combined with a layer of STO. Besides extraordinarily-high subwavelength transmission, the simulation results also show strong tunable transmission characteristics. Both the location and magnitude of the transmission peak can be tuned by temperature, converging angle, and both of the metal and STO film thickness. Moreover, adding a STO layer offers a new approach to actively control the transmission without mechanically changing the optical device. As a result, this proposed

structure could lead to extraordinary transmission at different wavelengths and can be used to develop temperature-tuning THz filters.

REFERENCE

1. Tonouchi, M., *Cutting-edge terahertz technology.* Nature Photonics, 2007. **1**(2): p. 97-105.
2. Piesiewicz, R., et al., *Short-range ultra-broadband terahertz communications: Concepts and perspectives.* Ieee Antennas and Propagation Magazine, 2007. **49**(6): p. 24-39.
3. Woodward, R.M., et al., *Terahertz pulse imaging in reflection geometry of human skin cancer and skin tissue.* Physics in Medicine and Biology, 2002. **47**(21): p. 3853-3863.
4. Strachan, C.J., et al., *Using terahertz pulsed spectroscopy to quantify pharmaceutical polymorphism and crystallinity.* Journal of Pharmaceutical Sciences, 2005. **94**(4): p. 837-846.
5. Nagel, M., et al., *Integrated THz technology for label-free genetic diagnostics.* Applied Physics Letters, 2002. **80**(1): p. 154-156.
6. Ebbesen, T.W., et al., *Extraordinary optical transmission through sub-wavelength hole arrays.* Nature, 1998. **391**(6668): p. 667-669.

7. Cao, Q. and P. Lalanne, *Negative role of surface plasmons in the transmission of metallic gratings with very narrow slits.* Phys Rev Lett, 2002. **88**(5): p. 057403.

8. Lalanne, P., J.P. Hugonin, and J.C. Rodier, *Theory of surface plasmon generation at nanoslit apertures.* Phys Rev Lett, 2005. **95**(26): p. 263902.

9. Lezec, H.J. and T. Thio, *Diffracted evanescent wave model for enhanced and suppressed optical transmission through subwavelength hole arrays.* Optics Express, 2004. **12**(16): p. 3629-3651.

10. Qu, D.X., D. Grischkowsky, and W.L. Zhang, *Terahertz transmission properties of thin, subwavelength metallic hole arrays.* Optics Letters, 2004. **29**(8): p. 896-898.

11. Cao, H. and A. Nahata, *Influence of aperture shape on the transmission properties of a periodic array of subwavelength apertures.* Optics Express, 2004. **12**(16): p. 3664-3672.

12. Miyamaru, F. and M. Hangyo, *Finite size effect of transmission property for metal hole arrays in subterahertz region.* Applied Physics Letters, 2004. **84**(15): p. 2742-2744.

13. Azad, A.K., Y. Zhao, and W. Zhang, *Transmission properties of terahertz pulses through an ultrathin subwavelength silicon hole array.* Applied Physics Letters, 2005. **86**(14).

14. Rivas, J.G., et al., *Enhanced transmission of THz radiation through subwavelength holes.* Physical Review B, 2003. **68**(20).

15. Janke, C., et al., *Optimization of enhanced terahertz transmission through arrays of subwavelength apertures.* Physical Review B, 2004. **69**(20).

16. Tanaka, M., et al., *Effect of a thin dielectric layer on terahertz transmission characteristics for metal hole arrays.* Optics Letters, 2005. **30**(10): p. 1210-1212.

17. Pendry, J.B., L. Martin-Moreno, and F.J. Garcia-Vidal, *Mimicking surface plasmons with structured surfaces.* Science, 2004. **305**(5685): p. 847-848.

18. Degiron, A., et al., *Effects of hole depth on enhanced light transmission through subwavelength hole arrays.* Applied Physics Letters, 2002. **81**(23): p. 4327-4329.

19. Azad, A.K. and W.L. Zhang, *Resonant terahertz transmission in subwavelength metallic hole arrays of sub-skin-depth thickness.* Optics Letters, 2005. **30**(21): p. 2945-2947.

20. Pan, C.L., et al., *Control of enhanced THz transmission through metallic hole arrays using nematic liquid crystal.* Optics Express, 2005. **13**(11): p. 3921-3930.

21. Steele, J.M., et al., *Resonant and non-resonant generation and focusing of surface plasmons with circular gratings.* Optics Express, 2006. **14**(12): p. 5664-5670.

22. Koerkamp, K.J.K., et al., *Strong influence of hole shape on extraordinary transmission through periodic arrays of subwavelength holes.* Physical Review Letters, 2004. **92**(18).

23. Battula, A., et al., *Tunable transmission at 100 THz through a metallic hole array with a varying hole channel shape.* Optics Express, 2007. **15**(22): p. 14629-14635.

24. Wang, W., et al., *Tunable and polarization-selective THz range transmission properties of metallic rectangular array with a varying hole channel shape.* Optics Express, 2009. **17**(9): p. 7361-7367.

25. Battula, A., et al., *Tuning the extraordinary optical transmission through subwavelength hole array by applying a magnetic field.* Optics Letters, 2007. **32**: p. 2692-2694.

26. Kuzel, P. and F. Kadlec, *Tunable structures and modulators for THz light.* Comptes Rendus Physique, 2008. **9**(2): p. 197-214.

27. Tagantsev, A.K., et al., *Ferroelectric materials for microwave tunable applications.* Journal of Electroceramics, 2003. **11**(1-2): p. 5-66.

28. Palik, E.D., *Handbook of Optical Constants of Solids*. 1985: Academic.

29. Lavrinenko, A., et al., *Comprehensive FDTD modelling of photonic crystal waveguide components.* Optics Express, 2004. **12**(2): p. 234-248.

30. Bethe, H.A., *Theory of diffraction by small holes.* Phys. Rev., 1944. **66**: p. 163–182.

Chapter 4: Broadband Light Absorption Enhancement in Thin-Film Silicon Solar Cells

Currently, the performances of thin film solar cells are limited by poor light absorption and carrier collection. In this research, large, broadband, and polarization-insensitive light absorption enhancement was realized via integrating with unique metallic nanogratings. Through simulation, three possible mechanisms were identified to be responsible for such an enormous enhancement. A test for totaling the absorption over the solar spectrum shows an up to ~30% broadband absorption enhancement when comparing to bare thin film cells.

4.1 Introduction

Active materials used in thin film solar cells are usually polycrystalline or amorphous silicon (p-Si or *a*-Si) because of their low cost, nontoxicity, abundance and mature processing technology. Yet, such great benefits are balanced by a short carrier diffusion length in silicon, resulting in a much lower conversion than that in crystalline solar cells. To achieve a nearly complete absorption the absorbing layer's thickness should be at least a few micrometers. Unfortunately, this is unrealistic because of high and defect-related carrier recombination [1]. As a result, improving the absorption in thin film Si solar cells has become crucial. In the past years, many light-trapping techniques have been investigated, among which a typical example is the use of scattering surface textures [2]. However, they are balanced by the induced surface roughness that is almost of the same order as the film thickness and by the resulting large surface area which causes an increased surface recombination. Recently, notable progresses in the field of

surface plasmon polaritons (SPPs) [3] have provided a promising way of light-trapping, and have consistently drawn an increasing amount of attention [4-9].

Upon excitation, SPPs cause strong near-field amplitude of the incident electromagnetic (EM) field, and a resonantly enhanced scattering cross section (SCS) as well. With regard to light absorption enhancement in thin film solar cells, SPPs are thought to be useful because the dissipation energy is proportional to the electric field (E-field) squared, a larger E-field causes a larger absorption, and because a stronger SCS redirects more incident photons into the absorbing layer, substantially increasing the absorbing length. Early work in this area carried out in late 1990s involved incorporation of small copper or silver clusters in organic solar cells, reporting an increase in short circuit current by a factor of 2 [10-11]. More recently, Au or Ag nanoparticles [7, 9] and nanogratings [4] have been introduced to crystalline [7, 9] and amorphous [5, 12] silicon solar cells. Common disadvantages associated with those past efforts are that resonances can only occur at certain wavelengths, and their designs involve the use of metallic nanostructures directly on top of solar cells, which will block a fairly large amount of total incident solar photons [5-6, 8]. Even more unfortunate, excitation of SPPs is normally very polarization-sensitive to incident radiation. Placing a single scattering object on back side of the cell shows the potential to enhance the absorption [13]; however, using such a simple design to maximize the performance over either a broad spectrum or a large scale will be still a challenge.

In this research, a new thin film solar cell design, placing a metallic nanograting at the bottom of the optically active layer, was proposed. This design will not only free up those photons blocked by surface nanostructures in previous designs, but also achieve a broadband and polarization-insensitive absorption enhancement by taking advantage of effective coupling to planar waveguide modes, the Fabry-Perot (FP) resonance and the

SPPs resonance. The design was carefully examined by the two-dimensional (2D) finite element method, and contribution from all above three mechanisms was carefully analyzed. A remarkable ~30% light absorption improvement was anticipated from using the design, when compared to those bare *a*-Si thin film solar cells, and ~10% in certain wavelength ranges, when compared to bulk Si solar cells. Fabrication of such metallic nanogartings is technically feasible too. It can be made by a few advanced nanofabrication methods [14-15] or simply by aligning the surface with metallic nanowires [16].

4.2 Computational Considerations

The basic structure of the proposed design is shown in Figure 4.1. On top is a thin layer of indium tin oxide (ITO) having a thickness of T_1, acting as the top transparent electrode. The bottom electrode is a metallic nanograting with a feature period of P, thickness of T_2 and width of W. The grating slits can be filled with suitable dielectric materials, providing an additional ability to fine-tune the dielectric environment of the nanograting. The light-absorbing Si thin film is then sandwiched between two electrodes, with a thickness of T_3. Solar light will irradiate the cell from the top with TE and TM polarizations. To maximize the absorption, it is important to study the absorption's dependence on the structure's geometric parameters and incident polarizations. To simplify our discussions, we fixed the ITO's thickness, T_1, at 20 *nm* and the slit width, W, at 100 *nm*.

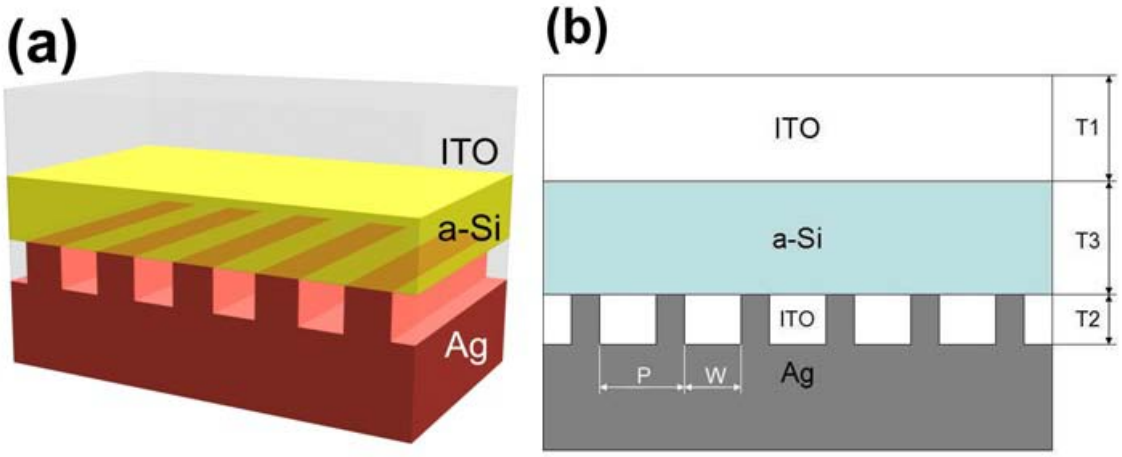

Figure 4.1: The proposed solar cell structure. (a) A 3D conceptual schematic. (b) A cross-sectional view outlining the device's structure to be used in simulations.

To match the solar spectrum to *a*-Si absorption, a wavelength range from 270 to 970 *nm* was selected. The simulated solar cell structure includes the use of ITO as top electrode, *a*-Si as absorbing material and Ag as bottom electrode, respectively. Dispersive dielectric constants of the three materials can be referred from references [17], [18] and [19]. The grating slits will be filled with either ITO or spin-on-glass (SOG). In our simulations, EM field distribution across the structure and light absorption by the active *a*-Si layer were analyzed. EM fields were assumed to be time harmonic and the resulting governing equations for the steady-state distribution were solved using a commercial 2D finite element software (COMSOL 3.3) [20]. The computational domain considered is a single unit cell surrounded either by periodic boundary conditions or by perfectly matching layers [21]. The absorption by the *a*-Si layer for a normal incident monochrome plane wave was calculated using eq

$$Absorption = \oint_{s} \vec{S}(\vec{r},\omega)\cdot d\vec{a} \tag{4.1}$$

where $\vec{S}(\vec{r},\omega)$ is the Poynting vector and s is the surface of the analyzed Si layer.

4.3 Results and Discussions

Figure 4.2a and 4.2b show the simulated E-field distribution across the bare *a*-Si thin film solar cell without the bottom Ag nanograting. Under the illumination of an ultraviolet (UV) wavelength of 270 *nm* (Figure 4.2a), the incoming photon energy was fully absorbed before reaching the bottom electrode. In the case of illuminating by a near infrared wavelength light of 960 *nm*, light reached the bottom electrode and was then reflected back, with only a limited amount of photons being absorbed by the *a*-Si layer. A more informative way to see this is to plot the ratio of light absorption in the basic cell using a bare 100 *nm* thick *a*-Si thin film to that using a semi-infinite Si layer (see figure 4.3). Figure 4.3 shows that for short wavelengths the ratios are close to unity, indicating that the absorption by thin film *a*-Si is comparable to that by the bulk Si. However, for long wavelengths the ratio falls below unity, to a minimum < 20% at certain wavelengths.

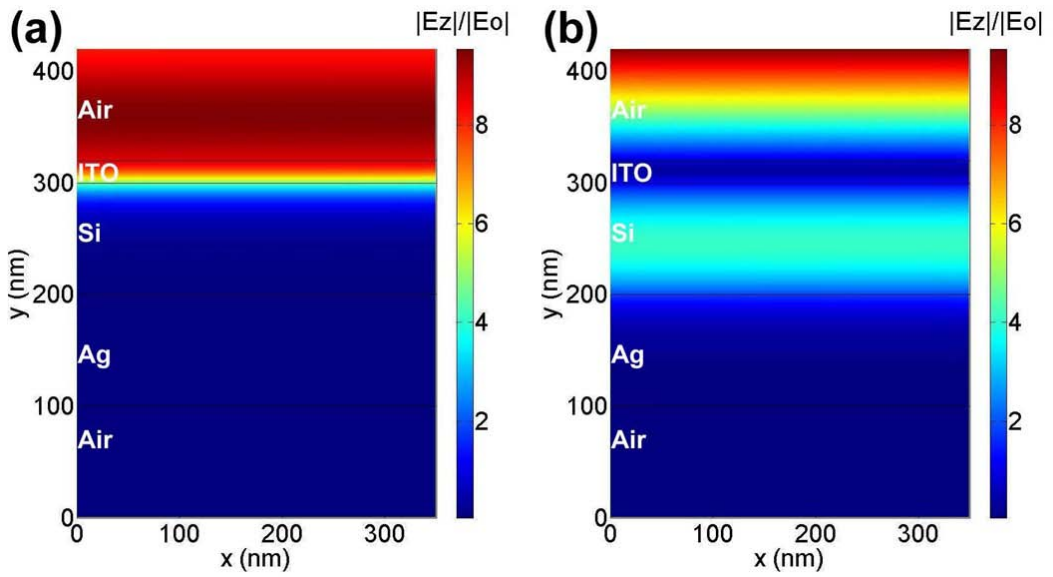

Figure 4.2: Normalized and time-averaged E-field intensity distribution across the basic *a*-Si solar cell structure at the case of normal incidence. The wavelengths are 270 *nm* (UV) (a) and 960 *nm* (near-infrared) (b), respectively. The cell uses a 100 *nm* thick *a*-Si layer.

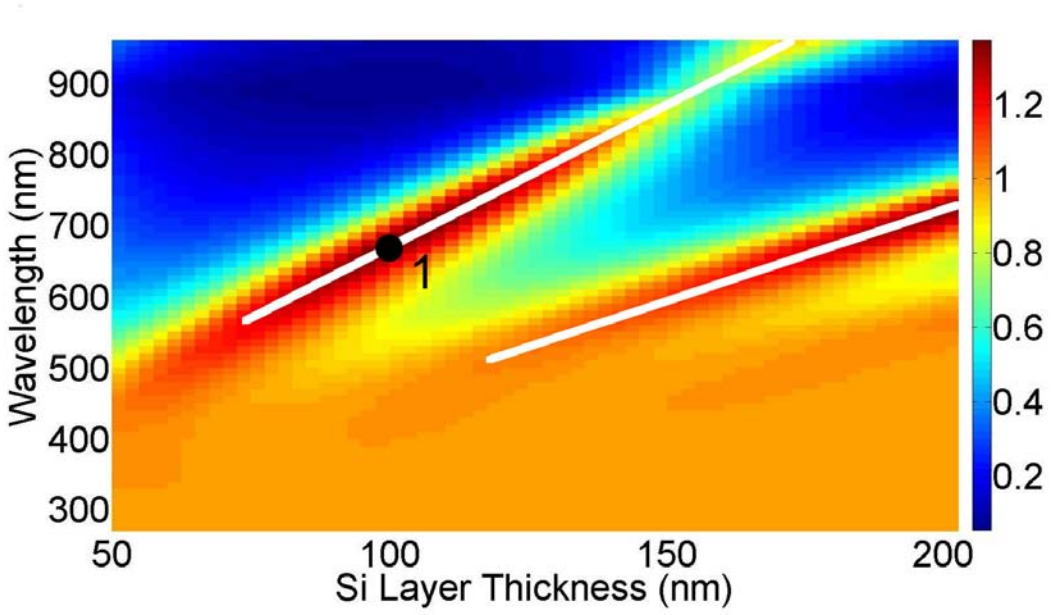

Figure 4.3: Plot of light absorption ratio in a basic cell using a 100 *nm* thick thin film *a*-Si to that using a semi-infinite Si layer. The incidence was assumed to be at normal.

Interestingly, in the long wavelength range figure 4.3 shows a few areas in which large light absorption enhancement occurs (marked with two white solid lines). This is due to the cavity resonance inside the *a*-Si layer, when both layer thicknesses and the incidence wavelength satisfy the resonance condition. Absorption is then enhanced by the much-intensified E-field inside the *a*-Si layer. Apparently, the wavelength band corresponding to such an enhancement is narrow. Adding an Ag nanograting into the basic cell structure may significantly improve the absorption. To make the comparison straightforward, an absorption enhancement function (Λ), defined as the ratio of absorbed energy by the same *a*-Si layer in thin film solar cells with and without adding the Ag nanograting, was used throughout our simulations. Λ is a function of the cell's geometric parameters (nanograting period, *a*-Si layer thickness, slit width, nanograting thickness, etc.), illumination conditions (incidence's wavelength and polarization), and those materials to be used inside the thin film solar cell structure.

Simulation results, obtained through mappings Λ with different structural parameters and incident conditions, are shown in figure 4.4a-4.4f. Inside those maps each calculation point represents a full-field simulation result according to corresponding geometric and illumination parameters. For all short wavelengths, adding the Ag nanograting maintains a good absorption, similar to the case without the grating. Significant differences will be (1) the way of absorption enhancement occurring at certain long wavelengths and (2) the broadband absorption enhancement. In figure 4.4, the long-wavelength absorption enhancement becomes complicated after adding the nanograting. In some areas (for example in figure 4.4c), such an enhancement can reach a level of ~14 times, referring to the intensity bar. A broadband absorption enhancement can also be witnessed in almost every map in figure 4.4, and this can be directly attributed to the Ag nanograting. In reality, the ability to realize a large, broadband, and polarization-

insensitive absorption enhancement will be crucial to practical thin film solar cells. Results shown here are therefore remarkable.

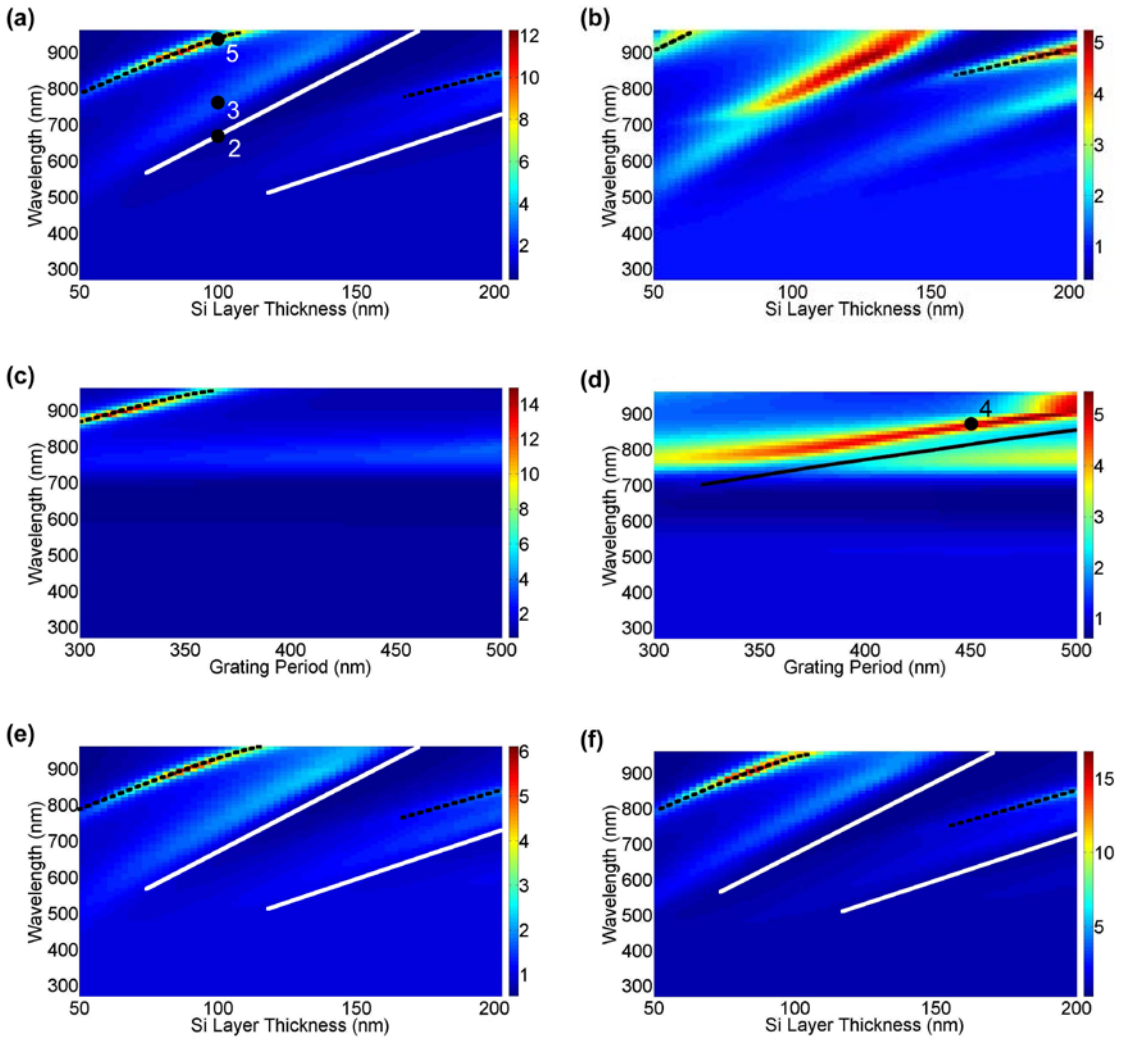

Figure 4.4: Mapping the absorption enhancement with varying geometric parameters and illumination conditions. For all nanograting-added cases, the grating slits were filled with ITO. (a) and (b) show the absorption enhancement with both wavelength and *a*-Si thickness for TE and TM incidences, respectively. The nanograting's periodicity and thickness are 350 *nm* and 50 *nm*, respectively. (c) and (d) show the enhancement versus both wavelength and nanograting's period. The *a*-Si layer thickness was fixed at 100 *nm* and the nanograting's thickness at 50 *nm*. Both TE and TM polarizations were considered in order to account for the randomly polarized nature of sunlight. (e) and (f) show maps of the absorption enhancement versus both wavelength and film thickness for TE mode only, but the nanograting's thicknesses was changed to 25 *nm* (e) and 100 *nm* (f), respectively.

For a better looking over those figures in Figure 4.4, both TE and TM wavelength-dependent absorption spectra were shown in Figure 4.5 (line-cuts when thickness for Si and Ag are fixed at 100 *nm* and 50 *nm*, respectively), selecting the grating period at 350 *nm* (corresponding to points 2, 3, and 5 in Figure 4.4a) and 450 *nm* (the point 4 in Figure 4.4d), respectively.

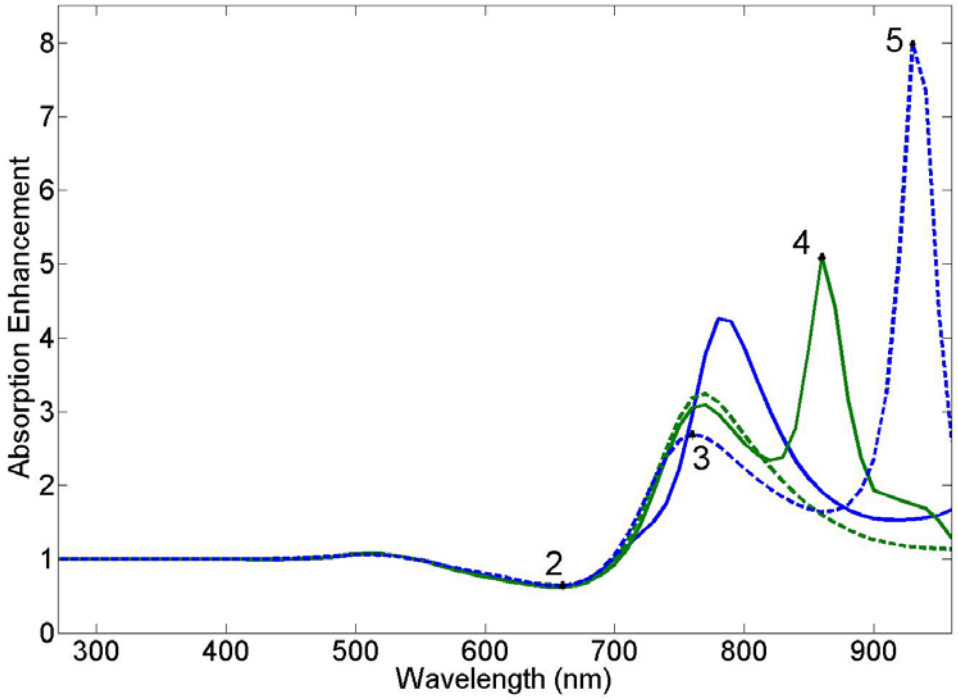

Figure 4.5: Absorption enhancement spectra at the Si thickness of 100*nm*, under TM (solid lines) and TE (dashed lines) illumination with the grating periods of 350 *nm* (blue) and 450 *nm* (green).

In figure 4.4, three absorption enhancement mechanisms in the long wavelength range can be identified and are responsible for the observed large, broadband, and polarization-insensitive absorption enhancement. The first mechanism is related to cavity resonance, and can be seen in those maps with varying *a*-Si layer thickness: figure 4.4a,

4.4b, 4.4e, and 4.4f. It is typically dependent on *a*-Si layer thickness, and shifts to red when increasing this thickness. The second mechanism directly relates to SPPs, which have characteristics of being excited only by TM polarization, less dependence of plasmonic wavelength on *a*-Si thickness, and red-shift as the nanograting's period increases. This can be clearly witnessed through those large enhancements shown in two TM polarization-excited maps: figure 4.4b and 4.4d. The last mechanism will be associated with coupling into the *a*-Si planar waveguide. Excitation of such planar guiding modes can be affected by *a*-Si layer thickness (figure 4.4a, 4.4e and 4.4f), nanograting period (figure 4.4b), and incident polarization (figure 4.4b), but much less affected by the nanograting's thickness (figure 4.4a, 4.4e, and 4.4f). All such guiding modes are clearly marked in figure 4.4a, 4.4b, 4.4c, 4.4e and 4.4f with dashed black lines.

In figure 4.4a, 4.4e, and 4.4f, the trend of the FP resonance-related enhancement can be referenced by two white solid lines in each map. Such lines are used to mark the FP resonance in the basic cell structure in figure 8. Clearly, adding an Ag nanograting to the structure causes a large red-shift of those FP resonances. In order to better interpret the FP resonance-related enhancement, Point 1 in figure 8 was selected as an example. This point represents a combination of wavelength at 670 *nm* and *a*-Si layer thickness of 100 *nm*, and corresponds to an exact FP resonance in the basic cell structure. After adding a 50 *nm* thick Ag nanograting with a period of 350 *nm*, the resonance red-shifted to Point 3 in figure 4.4a and figure 4.4, corresponding to a wavelength at 760 *nm*, and left a much reduced absorption at the original position of Point 2 (same position as Point 1 in figure 8). Such results can be further verified by the simulated EM field distributions (figure 4.6). Figure 4.6a and 4.6b show the E-field distributions across the basic cell for wavelengths at 670 *nm* (Point 1) and 760 *nm*, respectively. Obviously, the latter is slightly off the FP resonance. Figure 4.6c (4.6d) and 4.6e (4.6f) show TE (TM) electric

(magnetic) field distributions at Point 2 and 3, respectively. Comparing to figure 4.6c, figure 4.6e shows a much enhanced electric field intensity inside the *a*-Si layer at the wavelength of 760 *nm*, indicating a red-shift after adding the Ag nanograting. It is reasonable to assume that adding an Ag nanograting will actually change the effective cavity thickness, which causes the red-shift. According to figure 4.4a, 4.4e and 4.4f, the red-shift can also be affected by the Ag nanograting's thickness. Therefore, adjusting the Ag nanograting will be a practical means to tune the FP resonance (under both TE and TM polarizations) to better fit the solar spectrum, without the need to change the *a*-Si layer thickness.

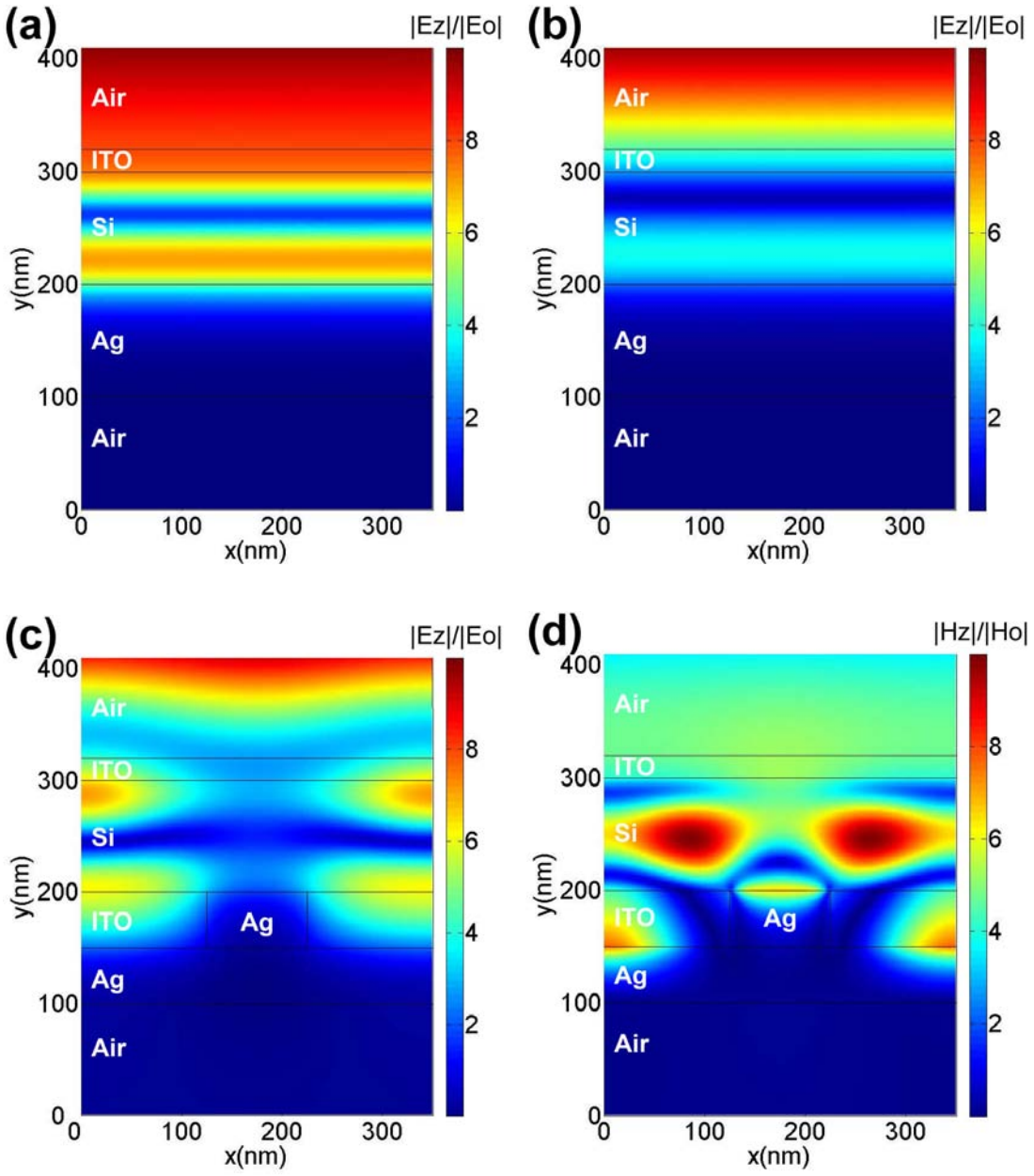
(a)
|Ez|/|Eo|
Air
ITO
Si
Ag
Air
y(nm)
x(nm)
(b)
|Ez|/|Eo|
Air
ITO
Si
Ag
Air
y(nm)
x(nm)
(c)
|Ez|/|Eo|
Air
ITO
Si
ITO
Ag
Ag
Air
y(nm)
x(nm)
(d)
|Hz|/|Ho|
Air
ITO
Si
ITO
Ag
Ag
Air
y(nm)
x(nm)

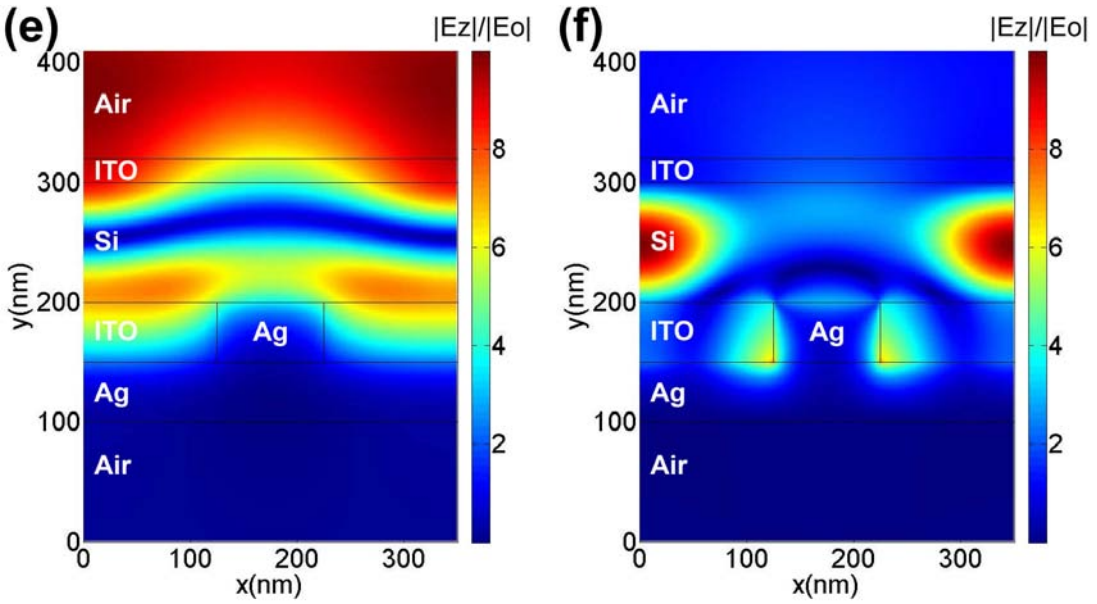

Figure 4.6: Normalized and time-averaged field plots across the cell structure. In all cases, the *a*-Si layer thickness is 100 *nm* and the incidence is at normal. (a) and (b) A bare *a*-Si layer was illuminated at wavelengths of 670 *nm* and 760 *nm*, respectively. (c) and (d) the nanograting-added structure illuminated by a wavelength of 670 *nm* at TE and TM polarizations, respectively. The Ag nanograting has P=350 *nm* and T_2 =50 *nm*, and was filled with ITO. (e) and (f) are similar to (c) and (d), but the incident wavelength was shifted to 760 *nm*.

Presence of an Ag nanograting increases the usefulness of TM polarization, according to the results shown in figure 4.4b and 4.4d in which as high as 5 times enhancement can be expected. To verify the judgment that such an enhancement is from TM polarization-excited SPPs, the relationship between the SPP wavelength and nanograting period was analyzed, and compared to the observed enhancement features shown in figure 4.4d. At the interface between two materials with dielectric constant ε_1 and ε_2, the SPP wavevector will be given by [22].

$$k_{sp} = k_0 \left(\frac{\varepsilon_1 \varepsilon_2}{\varepsilon_1 + \varepsilon_2} \right)^{1/2} \tag{4.2}$$

here k_{sp} is parallel to the interface and k_0 is wavevector at vacuum. Since ε_1 and ε_2 are opposite in sign (at least one material is conductive), k_{sp} is greater than the maximum photon wavevector available in the dielectric. The mismatch in wavevector between the in-plane momentums can be achieved by patterning the metal with a shallow grating of grooves having a period P. For a simple and one-dimensional (1-D) grating, phase matching will take place at [22]

$$k_{sp} = k_x \pm 2n\pi / P \tag{4.3}$$

At the normal incidence, k_x goes to zero. With n=1, substituting Eq. (4.3) into Eq. (4.2) results in Eq. (4.4), the requirement to excite SPPs with the metallic 1-D grating:

$$2\pi / P = k_0 \left(\frac{\varepsilon_1 \varepsilon_2}{\varepsilon_1 + \varepsilon_2} \right)^{1/2} \tag{4.4}$$

Here the interface is between ITO and Silver ($\varepsilon_1 = \varepsilon_{ITO}$ and $\varepsilon_2 = \varepsilon_{Ag}$). Since ε_{ITO}, ε_{Ag} and k_0 are functions of free space wavelengths, the SPP wavelength can be simplified as a function of the grating period. The estimated result is shown in figure 4.4d as a black solid line. The trend of this line matches well with the observed absorption enhancement features, and this supports the previous SPP-related absorption enhancement argument. A clear offset between the line and the observed absorption feature is due to the used approximation. In fact, ε_1 should be a complicated function of grating period, grating slit size, dielectric constants of ITO and Si, etc.

In order to look at the process more closely, Point 4 in figure 4.4d, corresponding to a wavelength of 860 *nm* and a grating period of 450 *nm*, was carefully analyzed. The

simulated EM field distribution across the cell with an Ag nanograting (figure 4.7b) shows a much stronger H_z field inside the *a*-Si layer, when compared to the case without the Ag nanograting (figure 4.7a). The argument that this enhancement is produced by SPPs can be supported by the strong H_z field observation around both Si/Ag and ITO/Ag interfaces (also found in figure 4.6d and 4.6f). This behavior indicates an existence of plasmonic current–a clear indication of TM polarization excited SPPs.

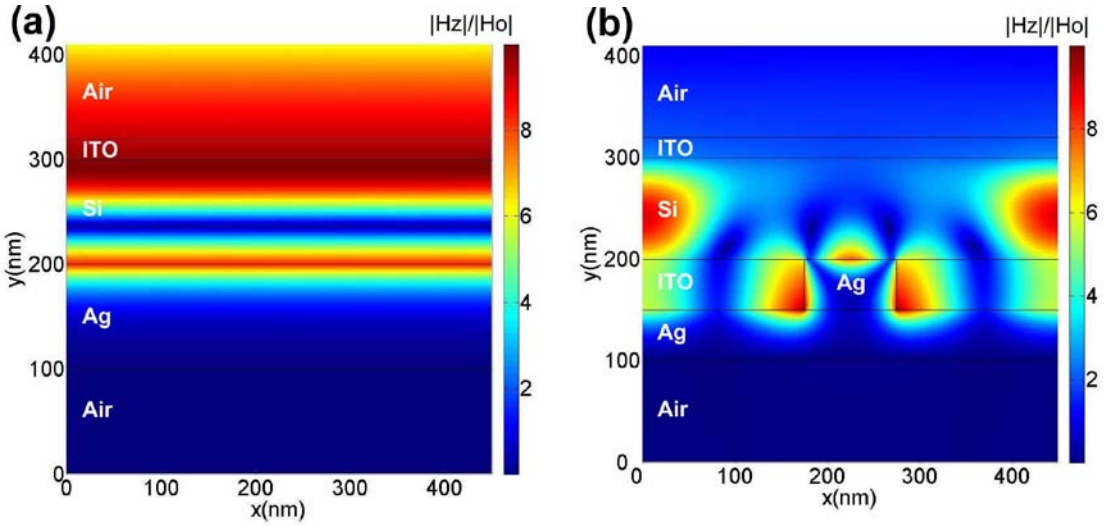

Figure 4.7: Normalized and time-averaged field plots across the cell structure. (a) A bare *a*-Si layer was illuminated at wavelength 860 *nm*. (b) An Ag nanograting with P=450 *nm*, T_2 =50 *nm* was added, and the grating was filled with ITO. The incoming light is a TM-polarized beam having a wavelength at 860 *nm* too.

A major contribution to the observed absorption enhancement is from lateral coupling of incident photons. In our designs, enhancement features from the lateral coupling can be found in figure 4.4a, 4.4b, 4.4c, 4.4e and 4.4f, all marked with dashed black lines. The simulated E-field distributions corresponding to Point 5 in figure 4.4a show a strong field pattern similar to that in ref. *6* (figure 4.8a). The guiding mode

weakens when removing the Ag nanograting (figure 4.8b). Formation of such strong field patterns is due to the excitation of guiding modes in the planar *a*-Si slab waveguide [23]. Very strong enhancement (up to 14 times) can occur in the near infrared regime for both TE and TM illuminations, after adding the Ag nanograting. This enhancement red-shifts with a thicker Si layer, a larger grating period and a thicker Ag nanograting.

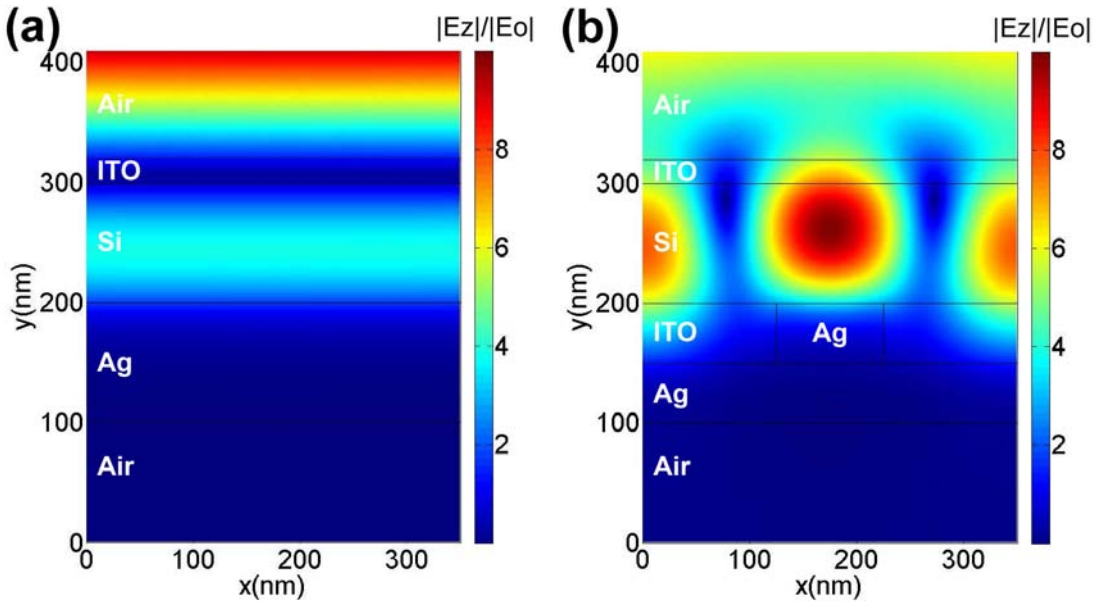

Figure 4.8: Normalized and time-averaged field plots across the cell structure. (a) A bare Si layer was illuminated at wavelength 930 *nm*. (b) A metallic grating structure was added with P=350 *nm*, T_2 =50 *nm* (fig. 4.1), and the grating slits were filled with ITO. The incoming light is TE polarized with the same wavelength as (a).

To perform a full evaluation on the design, total absorption enhancement over the full solar spectrum must be considered. Normally, a solar cell's short circuit current is proportional to the number of photons being absorbed. Therefore, total absorption enhancement must be evaluated based on the absorbed photon number. Assuming that distribution of the normalized photon number is a function of wavelength, $I(\lambda)$, for the

solar emission AM 1.5-G, and considering that the absorption enhancement due to the presence of the Ag nanograting is also a function of illumination (therefore, $\Lambda_{TM}(\lambda)$ and $\Lambda_{TE}(\lambda)$ were assumed to be functions representing different incident polarizations), the total absorption enhancement over the entire solar spectrum can be then calculated using:

$$\Lambda_{tot} = \frac{1}{2}\left(\int fI(\lambda) \times \Lambda_{TM}(\lambda) d\lambda + \int fI(\lambda) \times \Lambda_{TE}(\lambda) d\lambda\right) \tag{4.5}$$

where f is a normalized factor, i.e. $\int fI(\lambda) d\lambda = 1$.

Two slit filler materials, ITO and SOG, were considered, in order to see the effect of changing the nanograting's dielectric enviro*nm*ent. The dielectric constant of ITO can be found from ref. *18*. A complete representation for the dielectric constant of SOG will be difficult since that it strongly depends on its curing temperature (ref. *19*). Therefore it was assumed to have value of 2.7 + 0.01*i*. Fig. 4.9a and 4.9b show the enhancement as a function of *a*-Si thickness and Ag nanograting's period, respectively. The nanograting's thickness is 50 *nm*. The results clearly show that the dielectric enviro*nm*ent has little impact on the overall absorption enhancement.

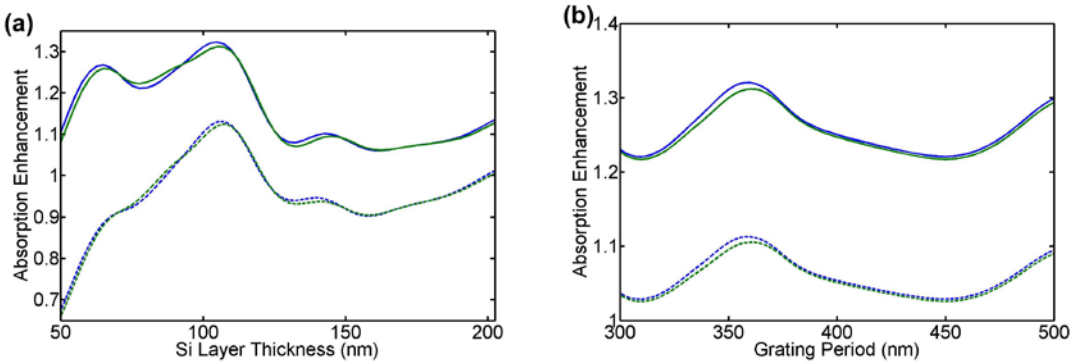

Figure 4.9: Total absorption enhancement over the full solar spectrum. (a) Absorption enhancement compared with bare thin layer *a*-Si (solid lines) and semi-infinite (bulk) Si layer (dashed lines) as a function of *a*-Si thickness with grating period at 350 *nm*. (b) Absorption enhancement as a function of grating periodicity with *a*-Si layer thickness at 100 *nm* (solid lines) and semi-infinite Si layer (dashed lines). The grating slits were filled with ITO (blue) and SOG (green).

The solid lines in Fig. 4.9a and 4.9b, which are the absorption enhancements when compared with a bare *a*-Si thin layer, show that adding the nanograting can enhance the absorption as much as 30 %. Furthermore, the enhancement is broadband when varying both *a*-Si layer thickness and the nanograting period. The dashed lines in Fig 4.9a and 4.9b represent the absorption enhancement when compared to bulk Si. It is very remarkable that, with the *a*-Si thickness changing from 85 to 120 *nm* and the grating period from 350 to 370 *nm*, performance of such an Ag nanograting-embedded thin film *a*-Si solar cell can be better than bulk Si-based solar cells. The average enhancement in this range can be above 10 %. To have a better evaluation of our cell design, the absorption efficiency is shown in figure 4.10.

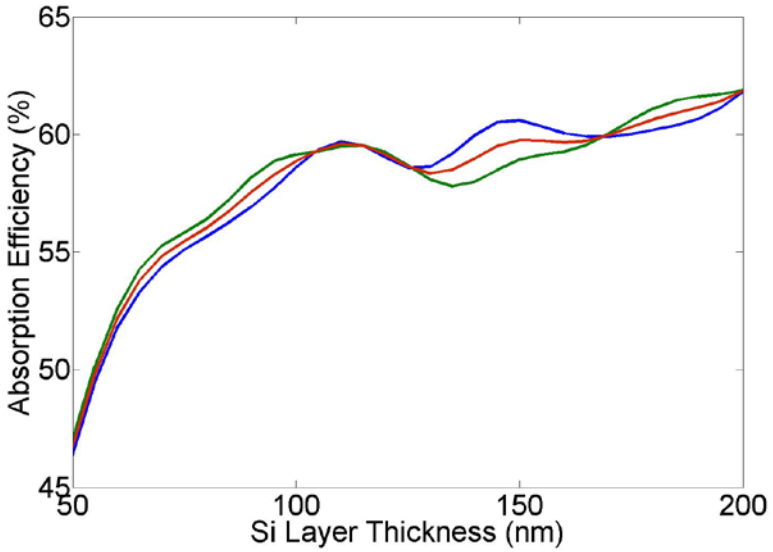

Figure 4.10: Absorption efficiency over the full solar spectrum as a function of the Si layer thickness. The efficiency was calculated under TM (blue), TE (green), and unpolarized (red) illumination, respectively. The grating period is fixed at 350 *nm*. The grating slits were filled with ITO.

Finally, we considered the absorption dependency on incident angle, as shown in Fig. 4.11. Total enhancement under an unpolarized illumination with an incident angle from 0~82^{o} is floating between 24 % and 31%, indicating that the response is relatively immune to the incident angle.

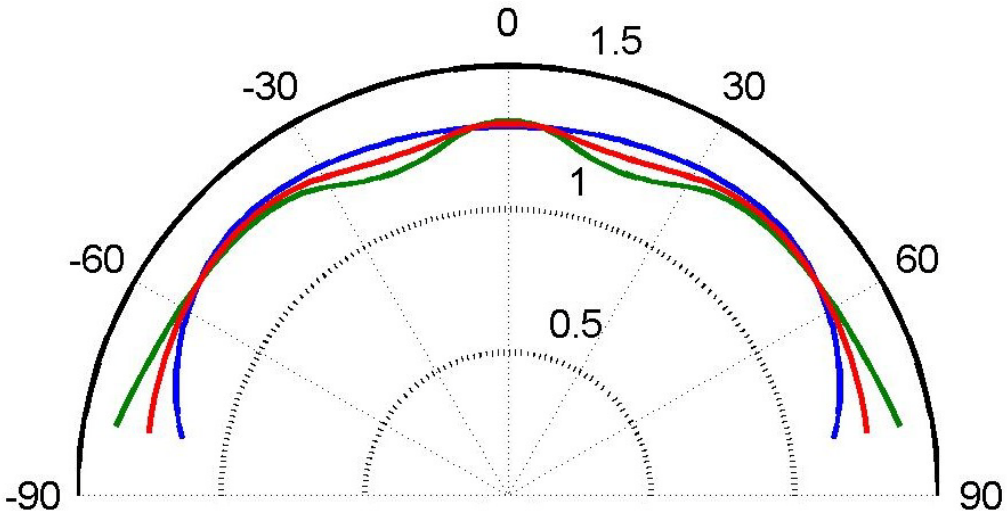

Figure 4.11: Absorption enhancement over the full solar spectrum as a function of the angle of incidence. The absorption was compared to the bare thin layer *a*-Si under TM (blue), TE (green), and unpolarized (red) illumination, respectively. Both Si thickness and grating period are fixed at 100 *nm* and 350 *nm*, respectively. The grating slits were filled with SOG.

4.4 CONCLUSION

In conclusion, a unique thin film Si solar cell design which includes an embedded metallic nanograting was proposed. While maintaining a similar absorption in the short wavelength range, large, broadband, and polarization-insensitive absorption enhancement can be realized in the long wavelength range (visible to infrared) when adding a thin metallic nanograting. Three mechanisms, the Fabry-Perot resonance, SPPs resonance and planar waveguide coupling, were identified in related to the observed high absorption enhancement. Since this unique solar cell design has no critical geometry requirements, concerns associated with fabrication and cost could be better balanced. Besides the

discussed *a*-Si, extending the similar design into other active solar materials such as CdTe and organics can also be expected.

REFERENCE

1. Shah, A.V., et al., *Thin-film silicon solar cell technology.* Progress in Photovoltaics, 2004. **12**(2-3): p. 113-142.

2. Green, M.A., *Lambertian light trapping in textured solar cells and light-emitting diodes: analytical solutions.* Progress in Photovoltaics: Research and Applications, 2002. **10**(4): p. 235-241.

3. Barnes, W.L., A. Dereux, and T.W. Ebbesen, *Surface plasmon subwavelength optics.* Nature, 2003. **424**(6950): p. 824-830.

4. Rockstuhl, C., S. Fahr, and F. Lederer, *Absorption enhancement in solar cells by localized plasmon polaritons.* Journal of Applied Physics, 2008. **104**(12).

5. Hallermann, F., et al., *On the use of localized plasmon polaritons in solar cells.* Physica Status Solidi *a*-Applications and Materials Science, 2008. **205**(12): p. 2844-2861.

6. Pala, R.A., et al., *Design of Plasmonic Thin-Film Solar Cells with Broadband Absorption Enhancements.* Advanced Materials, 2009. **21**(9999): p. 1-6.

7. Schaadt, D.M., B. Feng, and E.T. Yu, *Enhanced semiconductor optical absorption via surface plasmon excitation in metal nanoparticles.* Applied Physics Letters, 2005. **86**(6).

8. Panoiu, N.C. and R.M. Osgood, *Enhanced optical absorption for photovoltaics via excitation of waveguide and plasmon-polariton modes.* Optics Letters, 2007. **32**(19): p. 2825-2827.

9. Pillai, S., et al., *Surface plasmon enhanced silicon solar cells.* Journal of Applied Physics, 2007. **101**(9).

10. Stenzel, O., et al., *ENHANCEMENT OF THE PHOTOVOLTAIC CONVERSION EFFICIENCY OF COPPER PHTHALOCYANINE THIN-FILM DEVICES BY INCORPORATION OF METAL-CLUSTERS.* Solar Energy Materials and Solar Cells, 1995. **37**(3-4): p. 337-348.

11. Westphalen, M., et al., *Metal cluster enhanced organic solar cells.* Solar Energy Materials and Solar Cells, 2000. **61**(1): p. 97-105.

12. Derkacs, D., et al., *Improved performance of amorphous silicon solar cells via scattering from surface plasmon polaritons in nearby metallic nanoparticles.* Applied Physics Letters, 2006. **89**(9).

13. Ferry, V.E., et al., *Plasmonic Nanostructure Design for Efficient Light Coupling into Solar Cells.* Nano Letters, 2008. **8**(12): p. 4391-4397.

14. Fan, Z.Y., et al., *Toward the Development of Printable Nanowire Electronics and Sensors.* Advanced Materials, 2009. **21**(37): p. 3730-3743.

15. Chen, S.C., *Nanomanufacturing*. Nanotechnology Book Series. 2009, Stevenson Ranch, CA: American Scientific Publishers.

16. Tao, A.R., J.X. Huang, and P.D. Yang, *Langmuir-Blodgettry of Nanocrystals and Nanowires.* Accounts of Chemical Research, 2008. **41**(12): p. 1662-1673.

17. Palik, E.D., *Handbook of Optical Constants of Solids*. 1985: Academic.

18. Mergel, D. and Z. Qiao, *Dielectric modelling of optical spectra of thin In2O3 : Sn films.* Journal of Physics D-Applied Physics, 2002. **35**(8): p. 794-801.

19. Cook, R.F. and E.G. Liniger, *Stress-corrosion cracking of low-dielectric-constant spin-on-glass thin films.* Journal of the Electrochemical Society, 1999. **146**(12): p. 4439-4448.

20. *COMSOL 3.3 Reference Manual*. version 3.3 ed. 2005.

21. Lavrinenko, A., et al., *Comprehensive FDTD modelling of photonic crystal waveguide components.* Optics Express, 2004. **12**(2): p. 234-248.

22. Maier, S.A., *Plasmonics: Fundamentals and Applications*. 1st. ed. 2007: Springer.

23. Jackson, J.D., *Classical Electrodynamics*. 3rd ed. 1998: Wiley.

Chapter 5: Enhanced photon absorption and carrier generation in nanowire solar cells

Overall performance of a thin film solar cell is determined by the efficiency of converting photons to electrons through light absorption, carrier generation, and carrier collection. Recently, photon management via hybrid design has emerged as a powerful tool to further boost this conversion efficiency. Here we propose a novel nanograting solar cell design that achieves enhanced broadband light absorption and carrier generation in conjunction with the reduced use of active and non-earth-abundant materials. A test using this design for the short circuit current density in $CuIn_xGa_{(1-x)}Se_2$ (CIGS) thin film solar cells shows up to 250% enhancement when compared to corresponding bare thin film cells. In addition, placing metal strips on top of the nanograting to act as the top electrode reduces the use of non-earth-abundant materials such as indium that is normally used as the transparent conducting materials. This novel solar cell design has the potential to become a new solar cell platform technology.

5.1 Introduction

Thin film solar cell technology presents a powerful tool to tackle the world's increasing energy shortage. Cost and performance are major concerns when designing a thin film solar cell to provide cheap and abundant energy. A large portion [1] of a thin film solar cell's cost comes from the high cost of both active semiconductor and non-earth-abundant materials. In addition, these materials are often hazardous. Reducing environmental contamination and energy consumption in processing will require minimizing their use. Designing a thin film solar cell involves an inherent tradeoff in material use vs. light absorption and efficiency. For example, to realize a complete

absorption over the responsive solar spectrum in an amorphous silicon (a-Si) thin film solar cell, the absorbing layer's thickness should be at least a few micrometers. Unfortunately, this is unrealistic due to the increased material cost and the strong defect-related carrier recombination [2]. Therefore, a new thin film solar cell design that reduces the amount of both active and non-earth-abundant materials, enhances and balances the full-spectrum absorption, and improves the overall conversion efficiency, would be of significant importance to the solar cell industry.

Recently, notable progress in the field of surface plasmon polaritons (SPPs) [3] has provided a new way to trap light, drawing significant attention in the solar community[4-9] . Upon excitation, SPPs cause strong near-field amplitude of the incident electromagnetic (EM) field, as well as a resonantly enhanced scattering cross section (SCS). SPPs are expected to enhance light absorption because the dissipation energy is proportional to the square of the electric field (E-field). A larger E-field leads to a stronger absorption, and a stronger SCS redirects more incident photons to the absorbing layer, substantially increasing the absorbing length. Au or Ag nanoparticles [7, 9] and surface nanogratings [5] have been introduced to both crystalline [7, 9] and amorphous [5, 10] Si solar cells. Common disadvantages associated with those past efforts are that resonances can only occur at certain wavelengths, and their designs involve the use of surface metallic nanostructures directly on top of solar cells, which will block a fairly large amount of incident solar photons. [5-6, 8] Most recently, designs using embedded metallic structures were proposed [11-12]. Such designs not only free up those photons normally blocked by surface nanostructures in previous designs, but also achieve a large, broadband and polarization-insensitive absorption enhancement by taking advantage of effective coupling of light to planar waveguide modes, the Fabry-Perot (FP) resonance

and the SPP resonance. As high as 30% absorption enhancement was testified when using these embedded nanostructures [11].

More recently, research efforts has been focused on further reducing the use of both active and non-earth abundant materials in thin film solar cell architectures [13-16]. A nanowire optical antenna absorber was proposed [16], which demonstrates the potential to enhance short circuit current using less active material. However, the absorber does not include electrodes. To reduce the use of non-earth abundant materials, options vary according to what non-earth abundant element should be used. For example, thin film solar cells use non-earth-abundant elements in two major areas, such as indium in $CuIn_xGa_{(1-x)}Se_2$ (CIGS) as an absorbing material and in indium tin oxide (ITO) as a surface electrode. Tellurium in CdTe solar cells is another example. Replacing ITO by other conductive materials such as graphene is becoming a new trend [17], but unfortunately, very few alternatives could be found to replace the non-earth-abundant materials in the active layer. For a CIGS thin film solar cell, it has been demonstrated that its efficiency can be as high as 20% [18-19]. More important, CIGS solar cells showed excellent long-term stability in outdoor testing [20], high radiation resistance [21], high efficiency in large area modules [22], and the capability to be made lightweight with flexible substrates. As a result, CIGS-based solar cells have been considered as one of the most promising solar cell technologies for cost-effective and reliable power generation. Large scale implementation of the CIGS solar cells would benefit from new technologies that are able to reduce such non-earth-abundant material usage inside both the absorbing layer and the surface electrode layer without sacrificing the light absorption efficiency [23].

In this research, a new thin film solar cell design of patterning the entire thin film solar cell structure into a nanograting array is proposed (Fig. 1). A major merit of using

this structure is the potential for a significant reduction of both active and non-earth abundant material usage. For example, metallic strips on top of the active nanogratings can act as surface electrodes, and eliminate the need to use common surface electrodes such as ITO. The grating structure can also offer a large percentage reduction in the total active material usage, which can be easily determined by the grating's duty cycle. Furthermore, the structure can deliver a broadband and balanced absorption enhancement and an overall efficiency enhancement by taking advantage of waveguide resonance, metallic nanowire scattering, and the SPP resonance. A remarkable improvement in the short circuit current density as high as 250% is anticipated when applying this design to CIGS thin film solar cells as compared to the corresponding bare and non-grating thin film solar cells. Additionally, unlike using other electrode materials such as graphene, fabrication of such metal-semiconductor-metal nanogratings is technically feasible and compatible with standard complementary metal-oxide-semiconductor (CMOS) technology. [24-25]. Noting that, the geometric parameters of the nanograting, as well as the performance of the solar cells is controllable based on the fabrication methods. Finally, this design can be applied to many semiconductors such as a-Si, CdTe and GaAs (to be discussed in the supplementary information), and will lead to a new solar cell platform technology.

The design shown in Fig. 1 consists of a metal (thin)-semiconductor-metal (thick) structure. The through nanograting is made from the thin metallic layer side (acting as the top electrode), and their ditches stop at the thick metallic layer surface that acts as the bottom electrode. Solar light irradiates the cell from the top with transverse electric (TE) and transverse magnetic (TM) polarizations. In order to optimize the design, it is important to study the dependence of light absorption and short circuit current on the structure's geometric parameters and incident polarizations. To simplify our discussion,

we fixed the top thin metallic electrode's thickness, T_1, at 20 nm, and change other structural parameters including T_2, P, W, and the absorptive materials. Here silver was selected as both top and bottom electrode material and CIGS as the absorbing material. The gap between the nanogratings was assumed to be filled with air. Absorption enhancement in the absorbing layer and the short circuit current were also calculated over different absorptive materials such as a-Si, CdTe, and GaAs, with the goal of evaluating overall performance.

5.2 Computational Considerations

The design shown in Fig. 5.1 consists of a metal (thin)-semiconductor-metal (thick) structure. The through nanograting is made from the thin metallic layer side (acting as the top electrode), and their ditches stop at the thick metallic layer surface that acts as the bottom electrode. Solar light irradiates the cell from the top with transverse electric (TE) and transverse magnetic (TM) polarizations. In order to optimize the design, it is important to study the dependence of light absorption and short circuit current on the structure's geometric parameters and incident polarizations. To simplify our discussion, we fixed the top thin metallic electrode's thickness, T_1, at 20 nm, and change other structural parameters including T_2, P, W, and the absorptive materials. Here silver was selected as both top and bottom electrode material and CIGS as the absorbing material. The gap between the nanogratings was assumed to be filled with air. Absorption enhancement in the absorbing layer and the short circuit current were also calculated over different absorptive materials such as a-Si, CdTe, and GaAs, with the goal of evaluating overall performance.

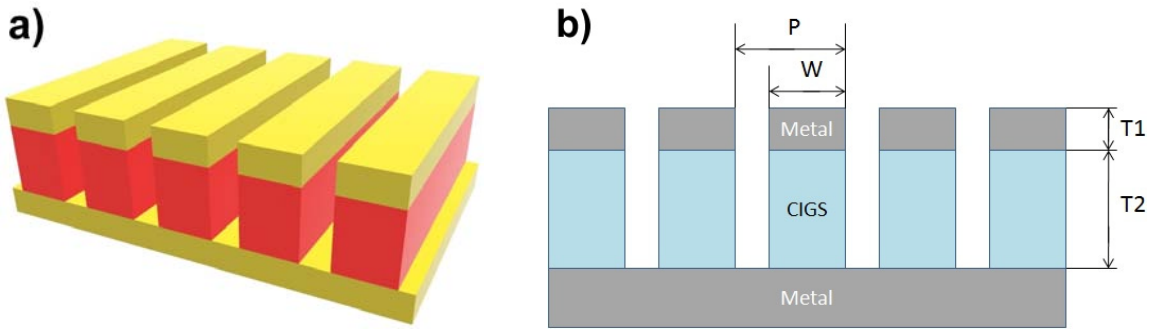

Figure 5.1: The proposed solar cell structure. (a) A 3D conceptual schematic. (b) A cross-sectional view outlining the device's structure to be used in the simulation. The top electrode thickness is T_1, the nanograting width is W, the period is P, and the active layer thickness is T_2.

We first analyzed the EM field distribution across the structure. EM fields were assumed to be time harmonic and the resulting governing equations for the steady-state distribution were solved using a commercial 2D finite element software (COMSOL 3.3) [25]. The computational domain considered is a single unit cell surrounded either by periodic boundary conditions or by perfectly matching layers [26]. The dispersive dielectric constants of silver and CIGS can be referred from references [27-28].

After we solved the EM distribution inside the cell, the absorption by the absorbing layer for an incident monochrome plane wave with certain wavelength λ was then calculated using eq. (5.1)

$$A(\lambda) = \oint_s \vec{S}(\vec{r}, \omega, \lambda) \cdot d\vec{a} \tag{5.1}$$

where $\vec{S}(\vec{r}, \omega, \lambda)$ is the Poynting vector and s is the surface of the analyzed absorptive layer. In order to make the comparison straightforward, an absorption enhancement function (Λ), defined as the ratio of the absorbed energy by the nanograting solar cell over the conventional thin film solar cell with the same thickness, was used throughout our simulations. Λ is a function of the cell's geometric parameters

(nanograting width, period, and absorbing layer thickness, etc.), illumination conditions (incidence's wavelength and polarization), and the selected absorbing material.

5.3 RESULTS

Simulation results, presented through mapping Λ with different structural parameters and incident conditions, are shown in figure 5.2. Inside those maps each point represents a full-field simulation result according to corresponding geometric and illumination parameters. Dark red areas indicate an absorption enhancement that can reach a high level of over 3 times, referring to the side intensity bar. The absorption maps show strong and broad band enhancement within the solar spectrum, especially within the relatively long wavelength range. This unique ability to balance the absorption over the spectrum and to achieve a large and broadband enhancement is crucial. Three possible enhancement mechanisms — coupling to the waveguide mode in the CIGS nanowire, scattering by the top silver electrode, and SPP resonance —will be discussed in details in the next section (section 5.4).

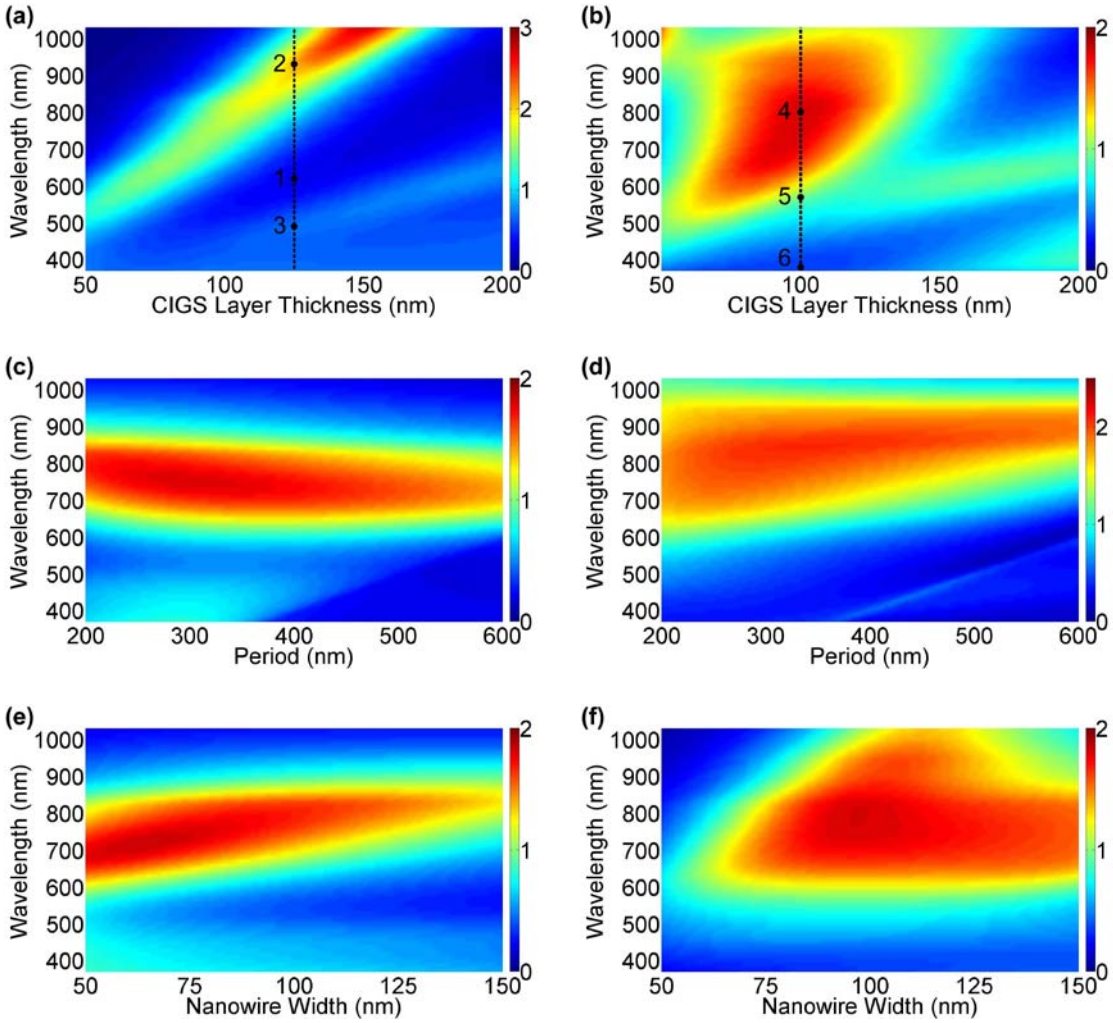
(a)
Wavelength (nm)
CIGS Layer Thickness (nm)
1
2
3
(b)
Wavelength (nm)
CIGS Layer Thickness (nm)
4
5
6
(c)
Wavelength (nm)
Period (nm)
(d)
Wavelength (nm)
Period (nm)
(e)
Wavelength (nm)
Nanowire Width (nm)
(f)
Wavelength (nm)
Nanowire Width (nm)

Figure 5.2: Mapping the absorption enhancement with varying geometric parameters and illumination conditions. Both TE and TM polarizations were considered in order to account for the randomly polarized nature of sunlight. (a, c, e) show the case under TE illumination while (b, d, f) show TM cases. (a) and (b) show the absorption enhancement versus both wavelength and the CIGS layer thickness. The array period and wire width are 200 nm and 100 nm, respectively. (c) and (d) show the enhancement versus both wavelength and the nanowire array's period. In these cases, the CIGS nanowire layer thickness and width (W) were both fixed at 100 nm. (e) and (f) show maps of the absorption enhancement versus both wavelength and nanowire width (W). The array period and wire thickness are fixed at 200 nm and 100 nm, respectively.

Changing CIGS layer thickness modifies the nanograting's cross section, which results in a shift in the waveguide resonance wavelength. In figure 5.2(a) (under TE illumination), as the CIGS layer thickness increases the absorption enhancement features a red shift and becomes broader and stronger simultaneously. Unlike the TE mode, TM illumination would excite SPPs, which results in very broad absorption enhancement band (more than 400 nm in figure 5.2b). As the CIGS layer thickness further increases beyond 110 nm, this SPP related enhancement weakens. Similar to the TE condition, this SPP-related enhancement red-shifts with thicker CIGS layer.

Changing the nanograting period will strongly affect the excited SPPs [29]. Under the TM illumination, the enhancement red-shifts as the period increase (figure 5.2d). At the same time, the enhancement does not change their spectral position very much under the TE illumination (figure 5.2c). Similar to the CIGS layer's thickness, the nanograting width also affects the nanograting's cross section. Figure 5.2e shows that, similar to the case of changing the active layer thickness, increasing the nanograting width leads to a red-shift of the enhancement. We have to point out that, this design is unique because that the grating duty cycle (the width-over-period ratio) plays an additional but very important

role in determining the absorption properties. A larger duty cycle means more used absorbing material but also more incident light to be blocked by the top metallic electrode. Figure 5.2b-d show that as the width and period increase, both of magnitude and bandwidth of the enhancement feature first undergo an increase and then diminish beyond certain points. As a result, a trade-off by balancing these two factors is needed in order to achieve the cell's maximum performance.

To better evaluate the nanograting solar cell design, short-circuit photocurrent density should be examined. It is a quantity describing the current generated per unit volume of active material in the nanograting solar cell compare with the conventional cell with the same absorbing layer thickness, reflecting the actual saving over the active material. First, we calculate the short-circuit photocurrent of a solar cell can be calculated as:

$$J_{SC} = q\int F_s(\lambda)\eta(\lambda,T_2)QE_{\text{int}}(\lambda)d\lambda \tag{5.2}$$

Here, q is the charge carried by one electron; $F_s(\lambda)$ is the spectral photon flux density delivered by the sun (AM 1.5-G); $\eta(\lambda,G)$ is the photon absorption efficiency of a solar cell, $G=\{g_1,g_2,g_3,...\}$ is the set of geometric parameters of the solar cell; $QE_{\text{int}}(\lambda)$ is the internal quantum efficiency of the absorbing material. The short-circuit photocurrent density is defined as photocurrent divided by the total volume of absorbing material used in the solar cell.

$$j_{SC} = J_{SC}\big/V = \frac{1}{V}q\int F_s(\lambda)\eta(\lambda,T_2)QE_{\text{int}}(\lambda)d\lambda \tag{5.3}$$

where V is the volume of absorbing materials.

Then, the short-circuit photocurrent density enhancement of the nanograting solar cell compared with conventional cell can be defined as:

$$K = \frac{j_{SC}^{NW}}{j_{SC}^{Con}}$$

$$= \frac{V^{Con} \cdot q\int F_s(\lambda)\eta^{NW}(\lambda, T_2, P, W)QE_{\text{int}}(\lambda)d\lambda}{V^{NW} \cdot q\int F_s(\lambda)\eta^{Con}(\lambda, T_2)QE_{\text{int}}(\lambda)d\lambda}$$

$$= \frac{V^{Con}}{V^{NW}} f(T_2)\int \frac{1}{2} F_s(\lambda)\eta^{Con}(\lambda, T_2)[\Lambda_{TM}(\lambda, T_2, P, W) + \Lambda_{TE}(\lambda, T_2, P, W)]QE_{\text{int}}(\lambda)d\lambda$$

…… (5.4)

Here, the variables with superscripts "NW" and "Con" denoted properties of nanograting and conventional cells, respectively; T_2, P and W are geometric parameters as defined above; in this equation $QE_{\text{int}}(\lambda)$, the internal quantum efficiency was assumed to be 100%, which has been demonstrate with NW junction devices [30]. $\Lambda_{TM}(\lambda, T_2, P, W)$ and $\Lambda_{TE}(\lambda, T_2, P, W)$ are absorption enhancement of nanograting cells under different incident polarizations; $f(T_2) = 1 \Big/ \int F_s(\lambda)\eta^{Con}(\lambda, T_2)QE_{\text{int}}(\lambda)d\lambda$ is a function of absorbing layer thickness T_2 only. Equation (5.4) shows the current density enhancement is a function of the geometric parameters of the nanograting array, which are absorbing layer thickness T_2, nanograting width W, and array period P.

Figure 5.3a-c show the simulation results of the current density enhancement versus different geometric parameters, and remarkably, the design in CIGS nanograting solar cell can enhance the overall current density over 250%. Unless the case that the nanograting width is very close to the period (in figure 5.3c), we can always expect a current density enhancement using whatever combination of geometric parameters.

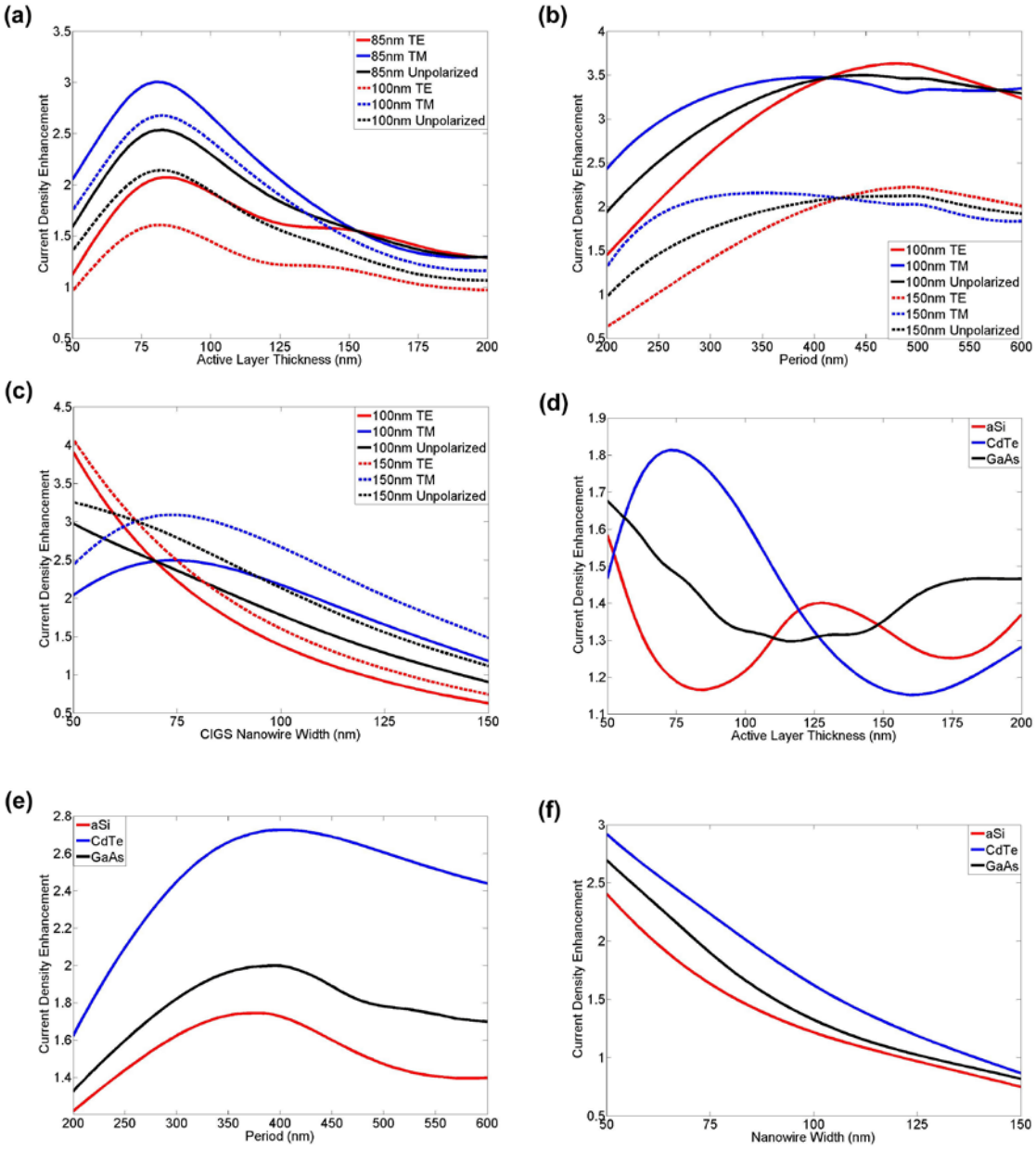
(a)
85nm TE
85nm TM
85nm Unpolarized
100nm TE
100nm TM
100nm Unpolarized
Current Density Enhancement
Active Layer Thickness (nm)
(b)
100nm TE
100nm TM
100nm Unpolarized
150nm TE
150nm TM
150nm Unpolarized
Current Density Enhancement
Period (nm)
(c)
100nm TE
100nm TM
100nm Unpolarized
150nm TE
150nm TM
150nm Unpolarized
Current Density Enhancement
CIGS Nanowire Width (nm)
(d)
aSi
CdTe
GaAs
Current Density Enhancement
Active Layer Thickness (nm)
(e)
aSi
CdTe
GaAs
Current Density Enhancement
Period (nm)
(f)
aSi
CdTe
GaAs
Current Density Enhancement
Nanowire Width (nm)

Figure 5.3: Short-circuit photocurrent density enhancement over the full solar spectrum. (a-c) shows the current density enhancement dependency on active layer thickness, array period, and nanograting width, respectively. (a) Current density enhancement compared with conventional cell as a function of active layer thickness with array period at 200 nm, wire width at 85 nm (solid lines) and 100 nm (dashed lines), respectively. (b) Current density enhancement compared with conventional cell as a function of array period with wire thickness at 200 nm, wire width at 100 nm (solid lines) and 150 nm (dashed lines), respectively. (c) Current density enhancement compared with conventional cell as a function of wire width with array period at 200 nm, wire thickness at 100 nm (solid lines) and 150 nm (dashed lines), respectively. In (a-c), red, blue and black curves show the enhancement under TE, TM and unpolarized illumination, respectively. (d-f) Current density enhancement compared with conventional cell as a function of active layer thickness, period, and nanograting width. In (d), array period is 200 nm, wire width is 100 nm. In (e), active layer thickness is 100 nm, wire width is 100 nm. In (f) active layer thickness is 100 nm, array period is 200 nm. Red, blue and black curves in these Figures show the enhancement using different materials (a-Si, CdTe, and GaAs, respectively).

An alternative way to evaluate the cell's performance is to compare the total short circuit current enhancement, which is defined as the comparison of the current generated in the CIGS nanograting solar cell to the conventional cell with the same absorbing layer thickness. It is very remarkable that, when the nanowire width is 85 nm and the array period is 200 nm, with the CIGS thickness range from 70 to 95 nm, the total short circuit current generated by the CIGS nanograting solar cell can reach up to a 8% enhancement compared with its conventional counterpart, while using only 42.5% of the total absorbing material and getting rid of the transparent top oxide electrode.

The nanograting solar cell design was also applied to other absorbing materials, with a goal to investigate the design's wide applicability potential. Figure 5.3d-f shows the current density enhancement of cells using *a*-Si, CdTe and GaAs. Similar to the results using CIGS, strong current density enhancements were achieved for most design geometry. Particularly, within the active layer thickness range that we considered (from

50nm to 200nm), the enhancement is greater than 10% for all materials and reached 59%, 82% and 68% for *a*-Si, CdTe and GaAs, respectively. Such results are impressive, but they are inferior to those from the use of CIGS. The better performance is due to the better absorption (larger $\eta^{Con}(\lambda)$) at long wavelength of the CIGS material. In the nanograting design, strong absorption enhancement was always observed at long wavelength (larger than 600nm). When calculating the current density enhancement by averaging the absorption enhancement over the whole solar spectrum (eq. (5.4)), larger $\eta^{Con}(\lambda)$ at long wavelength gave strong absorption enhancement, which then results in higher current density enhancement.

5.4 DISCUSSIONS

Figure 5.2a-b shows the absorption enhancements maps vs. CIGS layer thickness inside the nanograting cell and wavelength under both TE and TM illumination. By holding the thickness unchanged (denoted as dashed lines in figure 5.2), the absorption enhancement will reach several peaks and deeps as changing the incoming light wavelength. In our analyses, electromagnetic (EM) field across the cell structure at these peaks and deeps will be plotted to study the absorption enhancement mechanisms.

In the case of the TE illumination (figure 5.2a) and when we select the thickness at 125 nm, there is one absorption enhancement deep, point “1”, and two peaks, “2” and “3” in the wavelength range. The corresponding EM field distributions are plot in figure 5.4. For comparison, in figure 5.4a the electric field distribution at the same position of Point “1” in a conventional cell (no nanogratings and with a same active layer thickness) was shown. It shows a large and high electrical field in the conventional solar cell, which is due to the Fabry-Perot resonance inside the planar CIGS cavity. Fact of changing from

the planar absorbing layer to a nanograting array will break the Fabry-Perot resonance condition, which will result in an absorption decrease in the nanograting cell (31.7% compared with the conventional cell at this case). As the wavelength increasing, the absorption enhancement becomes stronger and it reaches a peak at 800nm (marked as the Point “2”). The corresponding electric field distribution in a nanograting cell was then shown in figure 5.4b. This figure actually shows two important properties. First, the reflection by the Ag top electrode is weak, which is due to the strong scattering by these metallic nanowires. Second, there is a large hot spot inside the CIGS nanowire, which indicates that most scattered energy are confined and absorbed in the CIGS nanowire by multiple internal reflections from the periphery. Apparently in this case, the strong absorption enhancement (207%) was because of strong metallic nanowire scattering and then efficient coupling to the nanograting waveguide modes. As the wavelength decreasing to 490nm (the Point “3” in figure 5.2), another absorption enhancement peak appears. The corresponding electric field distribution (figure 5.4c) shows that, in this case, the reflection rather than scattering by the metallic top nanowires is strong. Inside the CIGS nanowire, a higher order resonance inside the wire can be still seen. At this case the absorption is relatively lower than the conventional cell (67%). According to above analyses, scattering by the top electrode as well as the coupling to the nanowire waveguide resonance can be identified as the major contribution to the observed large absorption enhancement.

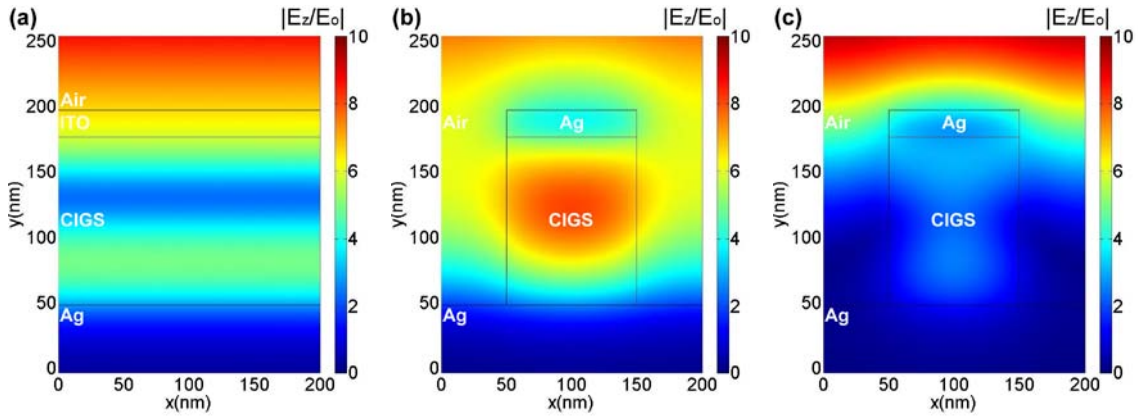

Figure 5.4: Normalized and time-averaged electric field plots across the cell structure under TE illumination. In all cases, the incidence is at normal and the CIGS layer thickness is fixed at 125nm. (a) A bare CIGS layer was illuminated at wavelength of 620 nm. (b) and (c) The nanograting CIGS cells were illuminated at wavelengths of 940nm and 490nm, respectively. The period and width of the nanogratings in the latter two cases are 200nm and 100nm, respectively.

Magnetic field distribution plots across the nanograting CIGS solar cells under the TM illumination corresponding to points "4"-"6" in figure 5.2b were shown in figure 5.5. At this case a CIGS layer thickness of 100nm was selected (denoted as dashed line in figure 5.2b). We first examined the magnetic field distribution at Point "4", which is an absorption enhancement peak at the 800nm wavelength, and the results were shown in figure 5.5a. In this case, most incoming light was transmitted through the Ag nanowire array due to the extraordinary optical transmission (EOT) phenomenon [31], which is caused by an efficient excitation of SPPs [32-34]. The transmitted light then confined in the CIGS wires which results in a strong absorption (181%) compared with the conventional cells. As the wavelength decreases, the absorption enhancement gradually attenuates, and then drops to nearly 1 as the wavelength equals 570nm (Point "5" in figure 5.2b). The magnetic field distribution at Point 5 was shown in figure 5.5b. At this

case the SPPs was also excited and a decent portion of the incoming light was still transmitted through the top electrode. However, most transmitted light travelled in the gaps between CIGS nanogratings and reflected back by the bottom electrode. Both magnetic field as well as the absorption inside the CIGS nanogratings was then relatively lower than the case of figure 5.5a. Apparently, this decrease of absorption enhancement is due to: (1) more reflection by the top electrodes; and (2) more transmitted lights travelled in the air gaps. As the wavelength continues to decrease, the absorption enhancement reached a deep at wavelength 380nm (Point "6" in figure 5.2b). The corresponding magnetic field (figure 5.5c) shows that the SPPs are very weak and most incoming light was reflected by the top electrode. The magnetic field is also very low inside the CIGS nanogratings. The absorption thus is very low if compared with the conventional cells (35%).

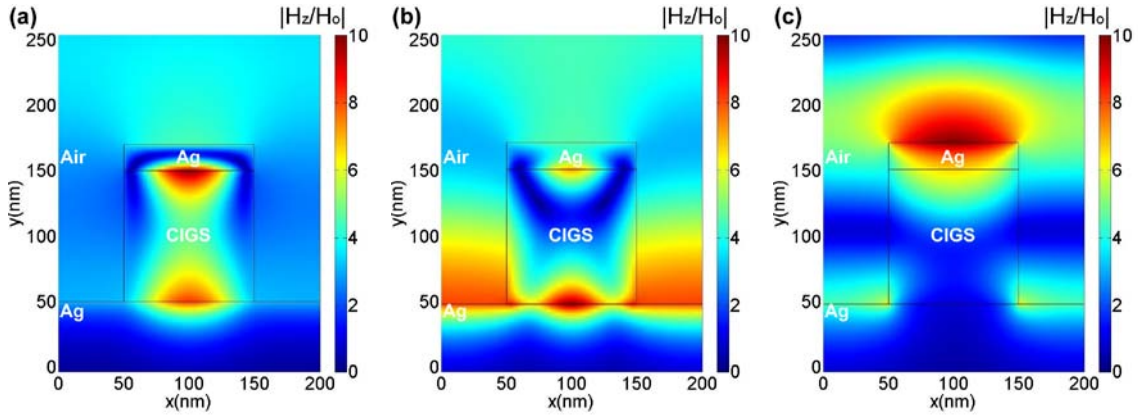

Figure 5.5: Normalized and time-averaged field plots across the nanograting CIGS cells under TM illumination. In all cases, the incidence is at normal and the CIGS layer thickness, period, and wire width is 100nm 200nm, and 100nm. The wavelengths of the incoming light are 800nm, 540nm and 380nm, respectively.

5.5 CONCLUSION

The absorption of the new nanograting solar cell design are dependent on geometric parameters (layer thickness, period, and nanograting width), illumination conditions (wavelength and polarization), and materials to be used (semiconductor and metals). The remarkable side of the design is the ability to incorporate different absorbing mechanisms together. Therefore the overall performance of the cell can deliver a strong enhancement over the conventional thin film solar cells. How wonderful would be a picture like that: adding a ~10% efficiency improvement over the current ~20% efficiency in CIGS thin film solar cells, using only 50% or less active CIGS materials, and using no ITO or other complicated surface electrode materials.

In conclusion, a unique thin film Si solar cell design which employed nanograting array as absorbing layer was proposed. The results showed large short circuit current density enhancement compared with conventional solar cells. Moreover, the design uses no expensive and scarce transparent conducting materials, providing a low cost and more sustainable way to solve the global warming problem. Since this unique solar cell design has no critical geometry requirements, concerns associated with the fabrication and then high cost could be better balanced. Beside the CIGS, the similar design was extended into other active solar materials such as *a*-Si, CdTe and GaAs (discussed in the supplementary information), and the results are impressive, indicating the design's wide applicability.

REFERENCE

1. Shah, A.V., et al., *Thin-film silicon solar cell technology.* Progress in Photovoltaics, 2004. **12**(2-3): p. 113-142.

2. Lalanne, P., J.P. Hugonin, and J.C. Rodier, *Theory of surface plasmon generation at nanoslit apertures.* Physical Review Letters, 2005. **95**(26).

3. Hallermann, F., et al., *On the use of localized plasmon polaritons in solar cells.* Physica Status Solidi a-Applications and Materials Science, 2008. **205**(12): p. 2844-2861.

4. Rockstuhl, C., S. Fahr, and F. Lederer, *Absorption enhancement in solar cells by localized plasmon polaritons.* Journal of Applied Physics, 2008. **104**(12).

5. Pala, R.A., et al., *Design of Plasmonic Thin-Film Solar Cells with Broadband Absorption Enhancements.* Advanced Materials, 2009. **21**(9999): p. 1-6.

6. Schaadt, D.M., B. Feng, and E.T. Yu, *Enhanced semiconductor optical absorption via surface plasmon excitation in metal nanoparticles.* Applied Physics Letters, 2005. **86**(6).

7. Panoiu, N.C. and R.M. Osgood, *Enhanced optical absorption for photovoltaics via excitation of waveguide and plasmon-polariton modes.* Optics Letters, 2007. **32**(19): p. 2825-2827.

8. Pillai, S., et al., *Surface plasmon enhanced silicon solar cells.* Journal of Applied Physics, 2007. **101**(9).

9. Derkacs, D., et al., *Improved performance of amorphous silicon solar cells via scattering from surface plasmon polaritons in nearby metallic nanoparticles.* Applied Physics Letters, 2006. **89**(9).

10. Ferry, V.E., et al., *Plasmonic Nanostructure Design for Efficient Light Coupling into Solar Cells.* Nano Letters, 2008. **8**(12): p. 4391-4397.

11. Wang, W., et al., *Broadband Light Absorption Enhancement in Thin-Film Silicon Solar Cells.* Nano Letters, 2010. **10**(6): p. 2012-2018.

12. Cao, L.Y., et al., *Engineering light absorption in semiconductor nanowire devices.* Nature Materials, 2009. **8**(8): p. 643-647.

13. Kelzenberg, M.D., et al., *Enhanced absorption and carrier collection in Si wire arrays for photovoltaic applications.* Nature Materials, 2010. **9**(3): p. 239-244.

14. Garnett, E. and P.D. Yang, *Light Trapping in Silicon Nanowire Solar Cells.* Nano Letters, 2010. **10**(3): p. 1082-1087.

15. Cao, L.Y., et al., *Semiconductor Nanowire Optical Antenna Solar Absorbers.* Nano Letters, 2010. **10**(2): p. 439-445.

16. Kim, K.S., et al., *Large-scale pattern growth of graphene films for stretchable transparent electrodes.* Nature, 2009. **457**(7230): p. 706-710.

17. Repins, I., et al., *19.9%-efficient ZnO/CdS/CuInGaSe2 solar cell with 81.2% fill factor.* Progress in Photovoltaics, 2008. **16**(3): p. 235-239.

18. Ramanathan, K., et al., *Properties of high-efficiency CuInGaSe2 thin film solar cells.* Thin Solid Films, 2005. **480**: p. 499-502.

19. Wieting, R.D., *CIS product introduction: Progress and challenges*, in *Ncpv Photovoltaics Program Review - Proceedings of the 15th Conference*, M. AlJassim and J.P. Thornton, Editors. 1999. p. 3-8.

20. Jasenek, A., et al., *Radiation resistance of Cu(In,Ga)Se2 solar cells under 1-MeV electron irradiation.* Thin Solid Films, 2001. **387**(1-2): p. 228-230.

21. Palm, J., et al., *CIGSSe thin film PV modules: from fundamental investigations to advanced performance and stability.* Thin Solid Films, 2004. **451**: p. 544-551.

22. Lewis, N.S., *Toward cost-effective solar energy use.* Science, 2007. **315**(5813): p. 798-801.

23. Fan, Z.Y., et al., *Toward the Development of Printable Nanowire Electronics and Sensors.* Advanced Materials, 2009. **21**(37): p. 3730-3743.

24. Chen, S., ed. *Nanomanufacturing*. Nanotechnology Book Series, ed. H.S. Nalwa. Vol. 284. 2009, American Scientific Publishers: Stevenson Ranch.

25. *COMSOL 3.3 Reference Manual*. version 3.3 ed. 2005.

26. Lavrinenko, A., et al., *Comprehensive FDTD modelling of photonic crystal waveguide components.* Optics Express, 2004. **12**(2): p. 234-248.

27. Palik, E.D., *Handbook of Optical Constants of Solids*. 1985: Academic.

28. Alonso, M.I., et al., *Optical functions of chalcopyrite CuGaxIn1-xSe2 alloys.* Applied Physics a-Materials Science & Processing, 2002. **74**(5): p. 659-664.

29. Maier, S.A., *Plasmonics: Fundamentals and Applications*. 1st. ed. 2007: Springer.

30. Tian, B.Z., et al., *Coaxial silicon nanowires as solar cells and nanoelectronic power sources.* Nature, 2007. **449**(7164): p. 885-U8.

31. Ebbesen, T.W., et al., *Extraordinary optical transmission through sub-wavelength hole arrays.* Nature, 1998. **391**(6668): p. 667-669.

32. Cao, Q. and P. Lalanne, *Negative role of surface plasmons in the transmission of metallic gratings with very narrow slits.* Phys Rev Lett, 2002. **88**(5): p. 057403.

33. Lalanne, P., J.P. Hugonin, and J.C. Rodier, *Theory of surface plasmon generation at nanoslit apertures.* Phys Rev Lett, 2005. **95**(26): p. 263902.

34. Lezec, H.J. and T. Thio, *Diffracted evanescent wave model for enhanced and suppressed optical transmission through subwavelength hole arrays.* Optics Express, 2004. **12**(16): p. 3629-3651.

Chapter 6: Outlook

6.1 Final summary

Plasmonic properties of subwavelength structures and their applications in optical devices have been explored in this dissertation. The following specific aims have been achieved. (i) Achieve polarization sensitive EOT in THz. (ii) Tune the EOT in THz by changing system temperature. (iii) Design plasmonic thin film solar cells that can achieve broadband absorption enhancement over the whole solar spectrum. (iv) Increase the short circuit current density, eliminate the expensive transparent top electrode, and further reduce the active materials used in the thin film solar cells.

In the first case, it was shown that by employing a metallic hole array of a rectangular converging-diverging channel (RCDC) shape, highly selective EOT in THz range was achieved. Moreover, for the rectangular holes with a high length-width ratio, a similar blue-shift in the transmission peaks as well as a narrower full width at half maximum (FWHM) are observed. Also, the converging angle of RCDC shape offers extra degrees of geometrical variables to 2D-MHA for tuning the location of the transmission peak and the FWHM.

In the second case, we have investigated the transmission spectra of metallic hole arrays with different converging-diverging channels combined with a layer of STO material. Besides extraordinarily-high subwavelength transmission, the simulation results also show strong tunable transmission characteristics. Both the location and magnitude of the transmission peak can be tuned by temperature, converging angle, and both of the metal and STO film thickness. Moreover, adding a STO layer offers a new approach to actively control the transmission without mechanically changing the optical device.

For the third aim, a plasmonic solar cell design with an embedded metallic nanograting was proposed. While maintaining a similar absorption in the short wavelength range, large, broadband, and polarization-insensitive absorption enhancement can be realized in the long wavelength range (visible to infrared) when adding a thin metallic nanograting. Three mechanisms, the Fabry-Perot resonance, SPPs resonance and planar waveguide coupling, were identified in related to the observed high absorption enhancement. Since this unique solar cell design has no critical geometry requirements, concerns associated with fabrication and cost could be better balanced. Besides the discussed *a*-Si, extending the similar design into other active solar materials such as CdTe and organics can also be expected.

Finally, for the last case, , a unique thin film Si solar cell design which employed nanograting array as absorbing layer was proposed. The results showed large short circuit current density enhancement compared with conventional solar cells. Moreover, the design uses no expensive and scarce transparent conducting materials, providing a low cost and more sustainable way for solar energy harvesting. Since this unique solar cell design has no critical geometry requirements, concerns associated with the fabrication and then high cost could be better balanced. Beside the CIGS, the similar design was extended into other active solar materials such as *a*-Si, CdTe and GaAs, and the results are impressive, indicating the design's wide applicability.

6.2 FUTURE WORK

In the field of plasmonics there are still lots of research opportunities to explore and develop. By employing metamaterials—man made materials whose permittivity and permeability can be engineered to be negative and positive, the new design proposed and

analyzed in this dissertation may open a chance to implement the SPs based circuits, where electronics could merge with photonics at the nanoscale [1] for developing ultra-low loss optically functional devices and couple them into non-conventional plasmonic chips. Hence it would be of significant interest to fabricate these new plasmonic optical devices and conduct experiments to confirm the tunable optical filters with fine properties.

The plasmonic solar cells are now suffering from the absorption of the metal materials, especially around the resonant frequencies, the relatively narrow enhancement bandwidth, and limited active material volume coupled with the plasmonic near-field enhancement (only at the metal/semiconductor interface). How to solve these problems remains a great challenge. Also, the plasmonics can benefit from further simplifying the solar cell structures, coupling more absorption enhancement mechanisms, and reducing the active and metal materials used in the cells.

REFERENCE

1. Ozbay, E., *Plasmonics: Merging photonics and electronics at nanoscale dimensions.* Science, 2006. **311**(5758): p. 189-193.

Bibliography

Alonso, M.I., et al., Optical functions of chalcopyrite CuGaxIn1-xSe2 alloys. Applied Physics a-Materials Science & Processing, 2002. 74(5): p. 659-664.

Atwater, H.A. and A. Polman, Plasmonics for improved photovoltaic devices. Nature Materials, 2010. 9(3): p. 205-213.

Azad, A.K. and W.L. Zhang, Resonant terahertz transmission in subwavelength metallic hole arrays of sub-skin-depth thickness. Optics Letters, 2005. 30(21): p. 2945-2947.

Azad, A.K., Y. Zhao, and W. Zhang, Transmission properties of terahertz pulses through an ultrathin subwavelength silicon hole array. Applied Physics Letters, 2005. 86(14).

Barnes, W.L., A. Dereux, and T.W. Ebbesen, Surface plasmon subwavelength optics. Nature, 2003. 424(6950): p. 824-830.

Battula, A., et al., Tunable transmission at 100 THz through a metallic hole array with a varying hole channel shape. Optics Express, 2007. 15(22): p. 14629-14635.

Battula, A., et al., Tuning the extraordinary optical transmission through subwavelength hole array by applying a magnetic field. Optics Letters, 2007. 32: p. 2692-2694.

Bethe, H.A., Theory of diffraction by small holes. Phys. Rev., 1944. 66: p. 163–182.

BOHREN, C.F. and D.R. HUFFMAN, Absorption and Scattering of Light by Small Particles. First ed. 1983, New York, NY: John Wiley & Sons. Inc.

Cao, H. and A. Nahata, Influence of aperture shape on the transmission properties of a periodic array of subwavelength apertures. Optics Express, 2004. 12(16): p. 3664-3672.

Cao, L.Y., et al., Engineering light absorption in semiconductor nanowire devices. Nature Materials, 2009. 8(8): p. 643-647.

Cao, L.Y., et al., Semiconductor Nanowire Optical Antenna Solar Absorbers. Nano Letters, 2010. 10(2): p. 439-445.

Cao, Q. and P. Lalanne, Negative role of surface plasmons in the transmission of metallic gratings with very narrow slits. Phys Rev Lett, 2002. 88(5): p. 057403.

Chen, S., ed. Nanomanufacturing. Nanotechnology Book Series, ed. H.S. Nalwa. Vol. 284. 2009, American Scientific Publishers: Stevenson Ranch.

COMSOL 3.3 Reference Manual. version 3.3 ed. 2005.

Cook, R.F. and E.G. Liniger, Stress-corrosion cracking of low-dielectric-constant spin-on-glass thin films. Journal of the Electrochemical Society, 1999. 146(12): p. 4439-4448.

Degiron, A., et al., Effects of hole depth on enhanced light transmission through subwavelength hole arrays. Applied Physics Letters, 2002. 81(23): p. 4327-4329.

Derkacs, D., et al., Improved performance of amorphous silicon solar cells via scattering from surface plasmon polaritons in nearby metallic nanoparticles. Applied Physics Letters, 2006. 89(9).

Ebbesen, T.W., et al., Extraordinary optical transmission through sub-wavelength hole arrays. Nature, 1998. 391(6668): p. 667-669.

Fan, Z.Y., et al., Toward the Development of Printable Nanowire Electronics and Sensors. Advanced Materials, 2009. 21(37): p. 3730-3743.

Ferry, V.E., et al., Plasmonic Nanostructure Design for Efficient Light Coupling into Solar Cells. Nano Letters, 2008. 8(12): p. 4391-4397.

Garnett, E. and P.D. Yang, Light Trapping in Silicon Nanowire Solar Cells. Nano Letters, 2010. 10(3): p. 1082-1087.

Green, M.A., Lambertian light trapping in textured solar cells and light-emitting diodes: analytical solutions. Progress in Photovoltaics: Research and Applications, 2002. 10(4): p. 235-241.

Hallermann, F., et al., On the use of localized plasmon polaritons in solar cells. Physica Status Solidi a-Applications and Materials Science, 2008. 205(12): p. 2844-2861.

Jackson, J.D., Classical Electrodynamics. 3rd ed. 1998: Wiley.

Janke, C., et al., Optimization of enhanced terahertz transmission through arrays of

subwavelength apertures. Physical Review B, 2004. 69(20).

Jasenek, A., et al., Radiation resistance of Cu(In,Ga)Se2 solar cells under 1-MeV electron irradiation. Thin Solid Films, 2001. 387(1-2): p. 228-230.

Kelzenberg, M.D., et al., Enhanced absorption and carrier collection in Si wire arrays for photovoltaic applications. Nature Materials, 2010. 9(3): p. 239-244.

Kim, K.S., et al., Large-scale pattern growth of graphene films for stretchable transparent electrodes. Nature, 2009. 457(7230): p. 706-710.

Koerkamp, K.J.K., et al., Strong influence of hole shape on extraordinary transmission through periodic arrays of subwavelength holes. Physical Review Letters, 2004. 92(18).

Kuzel, P. and F. Kadlec, Tunable structures and modulators for THz light. Comptes Rendus Physique, 2008. 9(2): p. 197-214.

Lalanne, P., J.P. Hugonin, and J.C. Rodier, Theory of surface plasmon generation at nanoslit apertures. Phys Rev Lett, 2005. 95(26): p. 263902.

Lavrinenko, A., et al., Comprehensive FDTD modelling of photonic crystal waveguide components. Optics Express, 2004. 12(2): p. 234-248.

Lewis, N.S., Toward cost-effective solar energy use. Science, 2007. 315(5813): p. 798-801.

Lezec, H.J. and T. Thio, Diffracted evanescent wave model for enhanced and suppressed optical transmission through subwavelength hole arrays. Optics Express, 2004. 12(16): p. 3629-3651.

Maier, S.A. and H.A. Atwater, Plasmonics: Localization and guiding of electromagnetic energy in metal/dielectric structures. Journal of Applied Physics, 2005. 98(1).

Maier, S.A., Plasmonics: Fundamentals and Applications. 1st. ed. 2007: Springer.

Mergel, D. and Z. Qiao, Dielectric modelling of optical spectra of thin In2O3 : Sn films. Journal of Physics D-Applied Physics, 2002. 35(8): p. 794-801.

Mie, G., Articles on the optical characteristics of turbid tubes, especially colloidal metal solutions. ANNALEN DER PHYSIK 1908(25).

Miyamaru, F. and M. Hangyo, Finite size effect of transmission property for metal hole arrays in subterahertz region. Applied Physics Letters, 2004. 84(15): p. 2742-2744.

Mulvaney, P., Not all that's gold does glitter. Mrs Bulletin, 2001. 26(12): p. 1009-1014.

Nagel, M., et al., Integrated THz technology for label-free genetic diagnostics. Applied Physics Letters, 2002. 80(1): p. 154-156.

O'Hara, J.F., R.D. Averitt, and A.J. Taylor, Terahertz surface plasmon polariton coupling on metallic gratings. Optics Express, 2004. 12(25): p. 6397-6402.

OTTO, A., EXCITATION OF NONRADIATIVE SURFACE PLASMA WAVES IN SILVER BY METHOD OF FRUSTRATED TOTAL REFLECTION. ZEITSCHRIFT FUR PHYSIK, 1968(216): p. 398.

Ozbay, E., Plasmonics: Merging photonics and electronics at nanoscale dimensions. Science, 2006. 311(5758): p. 189-193.

Pala, R.A., et al., Design of Plasmonic Thin-Film Solar Cells with Broadband Absorption Enhancements. Advanced Materials, 2009. 21(9999): p. 1-6.

Palik, E.D., Handbook of Optical Constants of Solids. 1985: Academic.

Palm, J., et al., CIGSSe thin film PV modules: from fundamental investigations to advanced performance and stability. Thin Solid Films, 2004. 451: p. 544-551.

Pan, C.L., et al., Control of enhanced THz transmission through metallic hole arrays using nematic liquid crystal. Optics Express, 2005. 13(11): p. 3921-3930.

Panoiu, N.C. and R.M. Osgood, Enhanced optical absorption for photovoltaics via excitation of waveguide and plasmon-polariton modes. Optics Letters, 2007. 32(19): p. 2825-2827.

Pendry, J.B., L. Martin-Moreno, and F.J. Garcia-Vidal, Mimicking surface plasmons with structured surfaces. Science, 2004. 305(5685): p. 847-848.

Piesiewicz, R., et al., Short-range ultra-broadband terahertz communications: Concepts and perspectives. Ieee Antennas and Propagation Magazine, 2007. 49(6): p. 24-39.

Pillai, S., et al., Surface plasmon enhanced silicon solar cells. Journal of Applied Physics, 2007. 101(9).

Porto, J.A., L. Martin-Moreno, and F.J. Garcia-Vidal, Optical bistability in subwavelength slit apertures containing nonlinear media. Physical Review B, 2004. 70(8).

Qu, D.X., D. Grischkowsky, and W.L. Zhang, Terahertz transmission properties of thin, subwavelength metallic hole arrays. Optics Letters, 2004. 29(8): p. 896-898.

Raether, H., Surface Plasmons on Smooth and Rough Surfaces and on Gratings. 1988: Springer-Verlag. 136 pages.

Ramanathan, K., et al., Properties of high-efficiency CuInGaSe2 thin film solar cells. Thin Solid Films, 2005. 480: p. 499-502.

Repins, I., et al., 19.9%-efficient ZnO/CdS/CuInGaSe2 solar cell with 81.2% fill factor. Progress in Photovoltaics, 2008. 16(3): p. 235-239.

Ritchie, R.H., Plasma losses by fast electrons in thin films. PHYSICAL REVIEW 1957(106).

Rivas, J.G., et al., Enhanced transmission of THz radiation through subwavelength holes. Physical Review B, 2003. 68(20).

Rockstuhl, C., S. Fahr, and F. Lederer, Absorption enhancement in solar cells by localized plasmon polaritons. Journal of Applied Physics, 2008. 104(12).

Sambles, J.R., G.W. Bradbery, and F.Z. Yang, Optical-Excitation of Surface-Plasmons - an Introduction. Contemporary Physics, 1991. 32(3): p. 173-183.

Schaadt, D.M., B. Feng, and E.T. Yu, Enhanced semiconductor optical absorption via surface plasmon excitation in metal nanoparticles. Applied Physics Letters, 2005. 86(6).

Shah, A.V., et al., Thin-film silicon solar cell technology. Progress in Photovoltaics, 2004. 12(2-3): p. 113-142.

Steele, J.M., et al., Resonant and non-resonant generation and focusing of surface plasmons with circular gratings. Optics Express, 2006. 14(12): p. 5664-5670.

Stenzel, O., et al., ENHANCEMENT OF THE PHOTOVOLTAIC CONVERSION EFFICIENCY OF COPPER PHTHALOCYANINE THIN-FILM DEVICES BY INCORPORATION OF METAL-CLUSTERS. Solar Energy Materials and Solar Cells, 1995. 37(3-4): p. 337-348.

Strachan, C.J., et al., Using terahertz pulsed spectroscopy to quantify pharmaceutical polymorphism and crystallinity. Journal of Pharmaceutical Sciences, 2005. 94(4): p. 837-846.

Tagantsev, A.K., et al., Ferroelectric materials for microwave tunable applications. Journal of Electroceramics, 2003. 11(1-2): p. 5-66.

Tanaka, M., et al., Effect of a thin dielectric layer on terahertz transmission characteristics for metal hole arrays. Optics Letters, 2005. 30(10): p. 1210-1212.

Tao, A.R., J.X. Huang, and P.D. Yang, Langmuir-Blodgettry of Nanocrystals and Nanowires. Accounts of Chemical Research, 2008. 41(12): p. 1662-1673.

Tian, B.Z., et al., Coaxial silicon nanowires as solar cells and nanoelectronic power sources. Nature, 2007. 449(7164): p. 885-U8.

Tonouchi, M., Cutting-edge terahertz technology. Nature Photonics, 2007. 1(2): p. 97-105.

Wang, W., et al., Broadband Light Absorption Enhancement in Thin-Film Silicon Solar Cells. Nano Letters, 2010. 10(6): p. 2012-2018.

Wang, W., et al., Tunable and polarization-selective THz range transmission properties of metallic rectangular array with a varying hole channel shape. Optics Express, 2009. 17(9): p. 7361-7367.

Wenger, J., et al., Single molecule fluorescence in rectangular nano-apertures. Optics Express, 2005. 13(18): p. 7035-7044.

Westphalen, M., et al., Metal cluster enhanced organic solar cells. Solar Energy Materials and Solar Cells, 2000. 61(1): p. 97-105.

Wieting, R.D., CIS product introduction: Progress and challenges, in Ncpv Photovoltaics Program Review - Proceedings of the 15th Conference, M. AlJassim and J.P. Thornton, Editors. 1999. p. 3-8.

Woodward, R.M., et al., Terahertz pulse imaging in reflection geometry of human skin cancer and skin tissue. Physics in Medicine and Biology, 2002. 47(21): p. 3853-3863.

Zakharian, A.R., M. Mansuripur, and J.V. Moloney, Transmission of light through small elliptical apertures. Optics Express, 2004. 12(12): p. 2631-2648.

Vita

Wei Wang was born in Shijiazhuang, Hebei Province, China on July 24th 1983. After finishing from Tsinghua High School from Beijing, he attended Tsinghua University, China to pursue his Bachelors in Automation. After that he further wanted to do graduate study and got into the University of Texas at Austin. Where, he did his research work in the general area of nanoscience and nanotechnology but with special emphasis in nano-optics.

Email address: andreww1983@gmail.com

This dissertation was typed by the author.